POLITECNICO DI MILANO
Department of Civil and Environmental Engineering

Master of science in Civil Engineering for Risk Mitigation

PROPAGATION AND IMPACT OF A DENSE FLOW SNOW AVALANCHE: FROM THE SMALL-SCALE EXPERIMENTS TO THE VAL DI ZOCCA EVENT

Supervisor: Prof. Francesco Calvetti

Co-examiner: Prof. Andrea Galli

Master thesis of:

Fabio Stabilini
Matr. 872982

Academic year 2018/2019

Acknowledgments

Sono grato a tutte quelle persone che hanno condiviso con me questo percorso. Per me il vostro supporto è stato essenziale. Sarebbe stato veramente difficile superare certi momenti di difficoltà senza di voi.
Ho avuto a cuore questo argomento perché alla Montagna devo molto, è il luogo dove sono cresciuto e dove ho coltivato tutti i migliori legami di amicizia. Questo piccolo mio contributo al mondo scientifico, per una migliore conoscenza dei fenomeni valanghivi spero possa essere una base per ulteriori studi e approfondimenti.
Ringrazio innanzitutto i miei genitori che hanno sempre creduto in me e mi hanno permesso questo percorso di crescita. Mia sorella Anna con cui spesso ho condiviso gioie e preoccupazioni mentre sedevamo allo stesso tavolo di studio.
Ringrazio poi gli amici di sempre, quelli con cui condivido fantastici weekend per sentieri, pareti e serate "scatenate".
Grazie a tutte le stupende persone che ho conosciuto questi ultimi anni a Lecco: i miei compagni di corso, i compagni di residenza e gli amici conosciuti durante le feste del Polo.
Grazie anche ai compagni del programma Unitech e del Trinity College con cui ho condiviso momenti bellissimi all'estero.
Grazie a Francesco che ha condiviso con me gioie e dolori del codice Anura.
Infine, voglio ringraziare il Prof. Calvetti per avermi guidato in questo percorso e la Dott.ssa Francesca Ceccato dell'Università di Padova per il preziosissimo aiuto con il codice MPM.

A tutti voi, **grazie di cuore**!

Summary

Snow avalanches are a major hazard to people and man-made structures in the Alps region. A better understanding of the propagation mechanism and the interaction of snow with the structures is crucial for the prediction of hazard zoning and the optimization of the mitigation measures. To this end, this thesis has the aim to use a numerical approach called MPM, extensively used in geomechanics, and adapt it to the snow avalanches.

The introduction of the work contains a state of the art about avalanche morphologies, snow rheologies and flow models.

In the second chapter, the MPM has been calibrated and validated with laboratory experiments on granular flows performed by Hutter (1995) and then extended to medium scale chute with dense snow (A. Upadhyay, 2010). The MPM 2D was employed to model the real scale propagation of a past event in Val di Zocca (Masino) and to compare the results with the commercial 3D code RAMMS. A scenario-based approach has been adopted to overcome the lack of data about the event and the many simplifying assumptions in modelling such a complex geomaterial.

The last part of the work is dedicated to the impact analysis of the flow against a wall. MPM simulations have been employed to capture the dynamic behaviour of the impact, find the actions on the structure and compare the findings with the current Italian and Swiss guidelines.

Contents

List of figures

List of tables

CHAPTER 1
INTRODUCTION

1.1 Description of snow

Snow is a porous medium consisting of air and water at the three different phases: ice, vapour and liquid. The ice phase consists in an assemblage of grains that are arranged in a random load bearing skeleton called ice matrix. This last one is surrounded by the ambient air which can be separated in dry air and water vapour component [1].

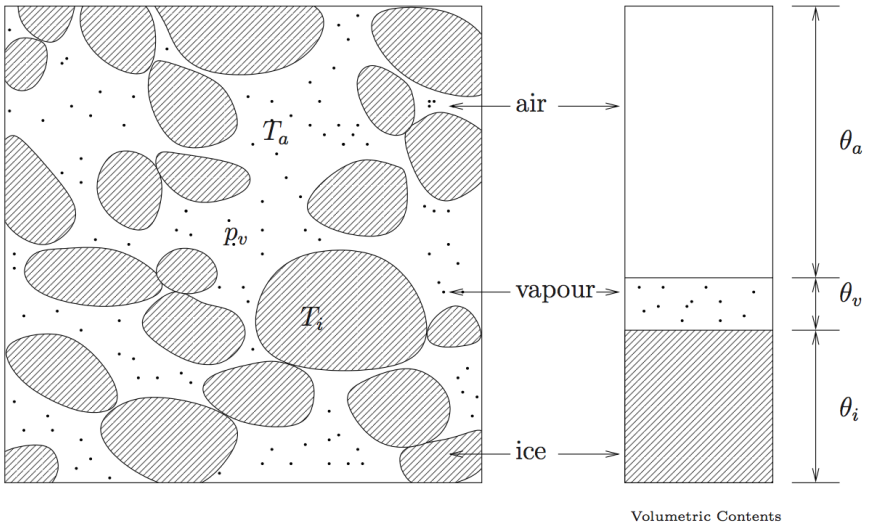

Figure 1.1 Schematic view of a sample of dry snow volume V [1].

Depending on the mixing ratio of the three components and the degree of impurity, snow has very mutable physical properties which influence avalanche events.

The snow history begins with the genesis in the troposphere and already at that level there can be high levels of variability in the grain shapes depending on air temperature, humidity, condensation nuclei and air mixing. (See [2] for a more complete description)

Changes in shape and size of grains occur during their whole life because snow temperature is close to its melting point (T_{melt}=273.15 K). The process is commonly known as metamorphism and it occurs when there is a thermo dynamical unstable condition:

- High surface energy due to large area over volume ratio
- Large temperature gradient (≈ 10°C/m) over the vertical profile of the snowpack

These two processes lead to very different ice crystal shapes. The former tends to round the grains since sphere is the shape with the lowest surface over volume ratio while the latter creates some pillar shape crystals called hoar.

A grain can grow and shrink many times over its life, up to the point it liquefies (Ambient temperature > 0°C) and starts flowing in the matrix of the residual crystals. In this case the snow contains liquid water and it is called wet snow.
In the following treatment only dry snow will be analysed.

1.2 Description of the snowpack

The snowpack consists of snow embedded layers with different characteristics that strongly depend on the snowfall event but also on the temperature history and wind exposure of the slope.
On a small scale there might be many differences due to the grain metamorphism explained in the previous subchapter.
On the contrary, on a large one if the weather conditions keep constant the structures are similar.
Layers are forming or destroying due to:

- the stratigraphic variation of subsequent snowfalls with different densities and then varying rates of fresh snow compaction
- the effect of wind of transport/deposition on the leeward side and erosion in the windward side, excavating and bringing to the surface the harder layers
- Surface melting during warm hours or short rainfalls wetting the surface followed by temperature drop during below freezing
- Surface hoar layers for water vapour condensation leading to very fragile structures
- Glide or creeping movements toward the direction of the slope

1.3 Mechanical properties

This subchapter wants to give the reader an overview about the mechanical behaviour of snow through the laboratory tests published in literature.
The review has already been tackled by the Ph. D. thesis performed by Cresseri S. [3] but, for the sake of completeness of the treating, the findings will be shown.

Significant experimental investigations date back in the period between the 50's and the 80's when the prediction and mitigation of the avalanche

hazard became a need. From the early beginnings many challenges arose regarding the sampling and testing techniques because of the fast-changing properties of snow that did not guarantee, during the tests, a reliable level of objectivity.

To briefly synthesize the peculiar aspects of this material, granular snow is conceived as an "***elastic-viscoplastic material that exhibits strong sensitivity to temperature, density and confining pressure***. *Furthermore, it is* ***time and strain-rate dependent***".[3]
The early works on the mechanical behaviour of snow were performed by Bader, Mellor and Fukue (1962, 1974,1979).
They highlighted the response of snow to different loading conditions, and through uniaxial tension, compression and base shear tests they investigated the dependency on several parameters.
A main finding is that "*snow exhibits a brittle-to-ductile transition with decreasing applied rate of deformation and this macroscopic behaviour is strictly related to the microcracks pattern".* [3]

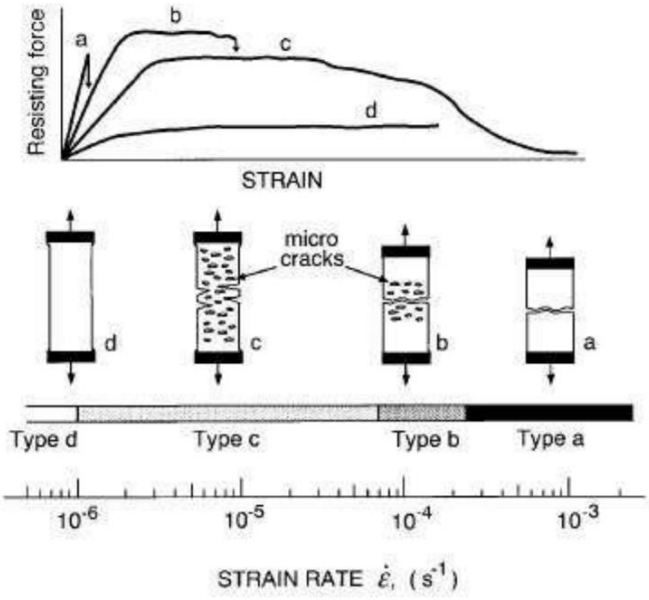

Figure 1.2 Schematic drawing of uniaxial tension test performed at T=-10°C and 290<ρ<310 Kg/m³ for different strain rates (Narita,1983)

From Figure 1.2 (a) can be noticed that under high strain rates (≈10^{-3}) the uniaxial traction increases linearly and the sample breaks in a brittle manner. As the strain rate is lowered, several irregular cracks appear in the specimen and the material shows a hardening process.
For very low applied strain rates, no microcracks appear and the resisting force increases asymptotically (d).
Tensile strength showed a tendency to increase with density, but the effect can be hindered by the change of snow matrix texture for different snow densities.

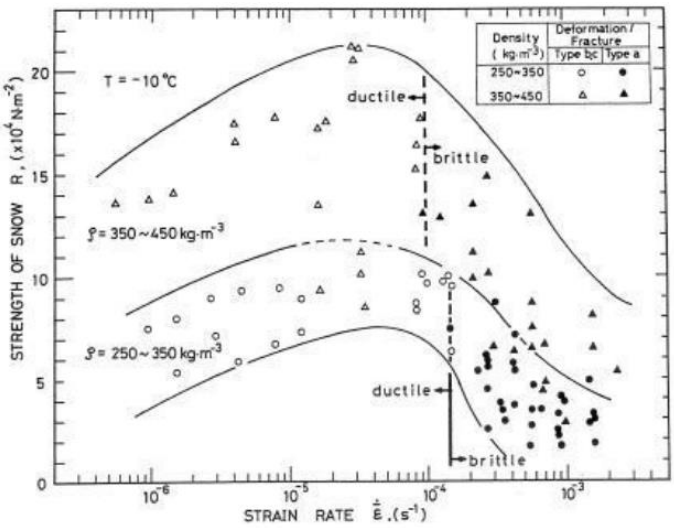

Figure 1.3 Density dependence at T=-10°C and for different strain rates (Narita,1983)

In the upper figure is evident that as density increases, the strength is higher and the boundary between brittle and ductile shifts backward its position.
Higher temperature, in line with the expectations, showed a reduction of strength and an increase of the transitional strain rate that widens the ductility domain (Figure 1.4)

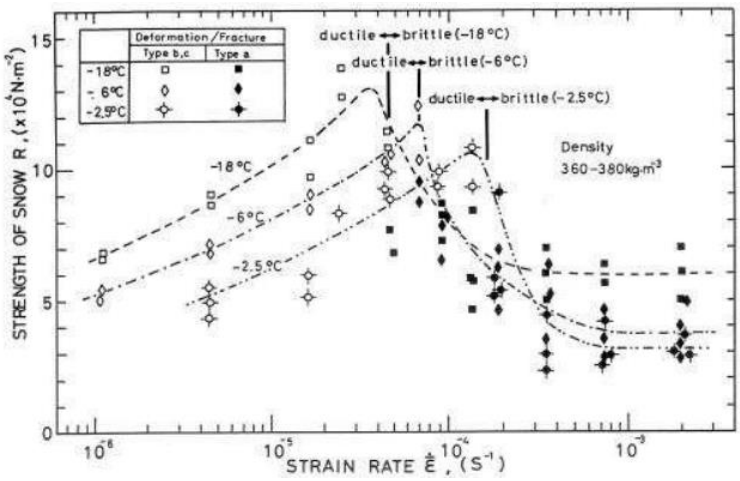

Figure 1.4 Temperature dependence of the tensile strength (Narita,1983)

Cresseri and Fukue (1979) [3] suggested that the high dependence on the applied strain rate depends on the micromechanical rearrangement of the grains and on the bonds disjointing.

Scapozza and Bartelt (2003) [3], in their doctoral thesis performed several tests that confirmed the previous results of Narita and showed (Figure 1.5), through an unconfined compression test, that the axial strain rate has a negligible effect on the hardening rate.

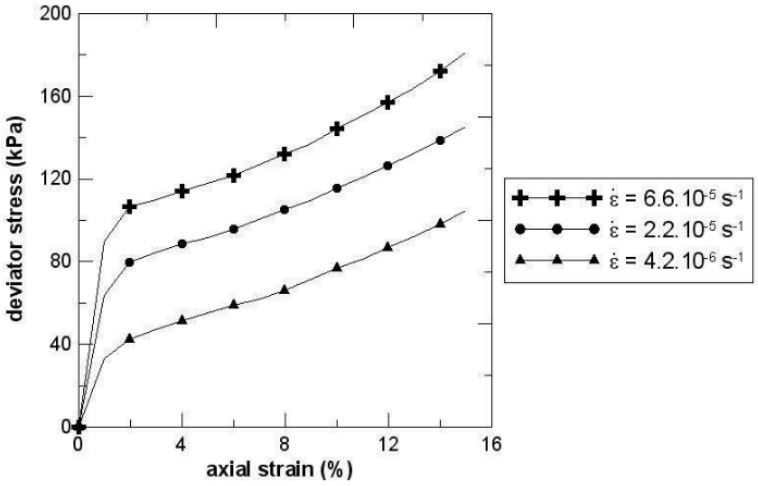

Figure 1.5 Strain rate effect in unconfined compression, T=-12°C and ρ=320 Kg/m³

Shear tests results from McClung and Schweizer (1977-1978) [3] performed on snow densities in the range 150-400 Kg/m^3 and temperatures between -10 and -6°C revealed that snow has a similar pattern to loose and dense sands.
This is reflected by the coupled effect of: strain softening, dilation of the sample (Figure 1.6 curve b) and the hardening response accompanied by contraction of the specimen (Figure 1.6 curve a).

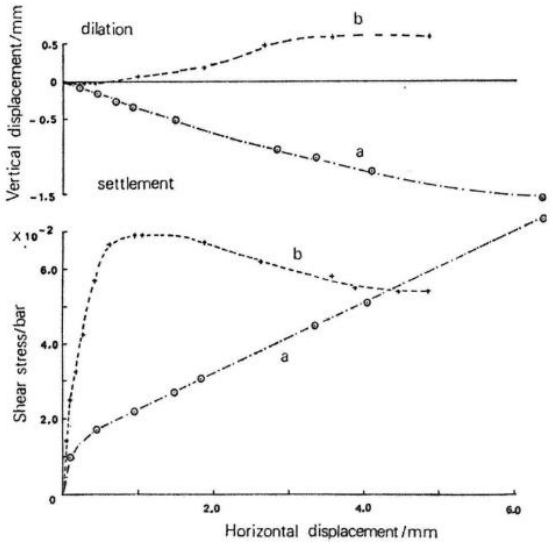

Figure 1.6 Shear stress and vertical displacements at low (curve a) and high (curve b) displacement rate McClung (1977)

Snow is also time-dependent and shows a viscous nature which depends on the stress path Shinojima (1967). *The higher the load the higher will be the creep rate resulting from time dependent structural changes*.[3]
With respect to soils the snow evidenced a viscous behaviour also during pure volumetric stresses.

Triaxial compression tests of Navarre et Al. (1987) demonstrated that snow belongs to the class of non-linear elasto-plastic materials with memory effects. During the reloading phase it exhibits a stiffer response until it reaches the maximum stress experienced (Figure 1.7).

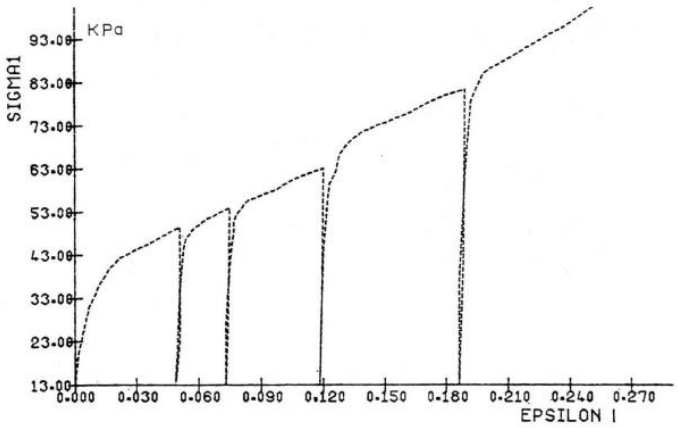

Figure 1.7 Axial stress-strain curve for σ_c=13kPa and ρ=320 Kg/m³ [4]

Non-drained triaxial tests performed some years later by Scapozza and Bartelt (2003), evidenced that for increasing densities the pre and post-yielding stiffness is higher (Figure(1.8))

The effect of confining pressure, in the range investigated (0-45kPa), is evident just in the hardening region and not in the pre yielding. (Figure 1.9)

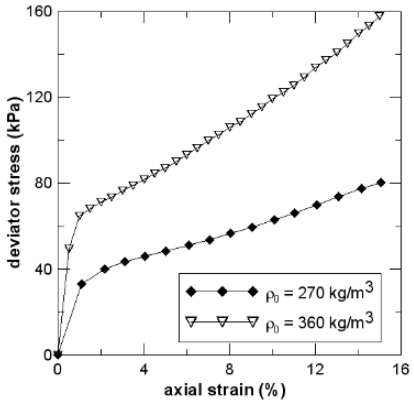

Figure 1.8 Effect of density, σ_c=10kPa (left)

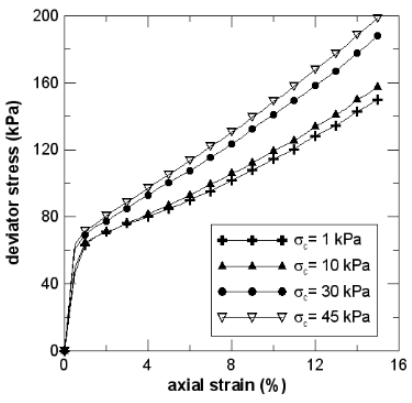

Figure 1.9 Effect of confining pressure, ρ=360 Kg/m³

1.4 Material law

Currently the constitutive models for describing snow behaviour are grouped into two big families: **phenomenological** and **micromechanical** models. The former group aims at reproducing the macroscopic behavior under certain loading conditions but neglect all the processes occurring at the microscopic level. The latter describes the role of the microstructure during the deformational process.
In engineering practice, even if the microstructural factors have been recognized critical, common constitutive approach is still at the macroscopic level.

The first one-dimensional rheological models were proposed as linear (Mellor,1974) or non-linear (Bader,1962; Salm,1971) constitutive laws obtained by a combination of elastic springs and dampers. Amongst them, the linear Burgers model was widely used for a qualitative description.
Few years later, the linear relation for the dashpot was adjusted with a hyperbolic sine law [3].
More recently, Scapozza and Bartelt proposed a hyperbolic potential equation to model the irreversible viscous deformations. Compared to elastic and plastic contributions, in their study they found the viscous part to be the leading factor determining total strains[1]. Viscous deformations assumed this shape:

$$\dot{\varepsilon}_v = A_0 e^{\frac{Q}{RT_i}} \sinh(\alpha\sigma)^n \tag{1.1}$$

Being R the molar gas constant, Q the activation energy, A_0 and n two material parameters density and temperature-dependent

One-dimension rheological models have the upside of being simple but they cannot be easily extended to multidimensional loading conditions [3].

In the literature, snow avalanches have also been treated as **non-Newtonian fluids** [5] because of the similarities with fluid flows. Compared to the typical Newtonian ones, it is evident that snow comes to rest also when the stresses are non-zero. This reason drove Dent et Lang (1983) to considered snow as a biviscous Bingham material.

Bingham is a viscoplastic material that behaves as an elastic body at low shear stresses but flows as a viscous fluid at high ones.

$$\begin{cases} \tau = G\gamma & for\ \tau < \tau_0 \\ \tau = \eta\dot{\gamma} + \tau_0 & for\ \tau \geq \tau_0 \end{cases} \quad (1.2)$$

Since the first formulation in 1916, many adjustments have been proposed [6]. The biviscous model developed by Dent et Lang is one example [5]. It shows that the non-constant plastic behavior, typical of Bingham fluids, well captures the locking property of snow at low stresses. This effect translates in a flow in which some portions of material behave as fluids and others as solids.

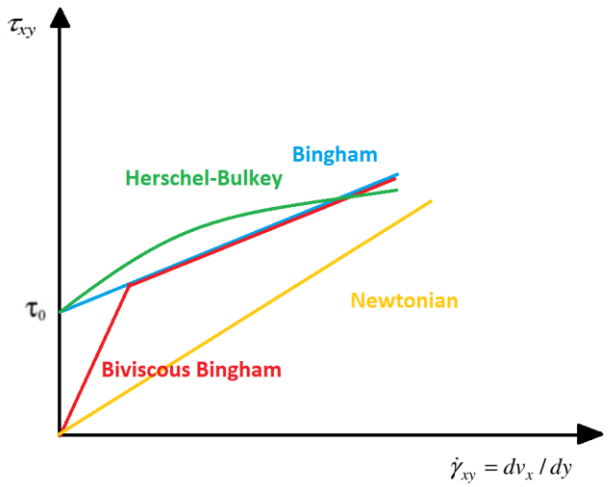

Figure 1.10 Shear stress vs shear rate for different viscoplastic models

Another version of the Bingham model is the Herschel-Bulkey, developed to take in account higher shear rate intervals [7]. It models the plastic behaviour with a non-linear law of the following type:

$$\begin{cases} \tau = G\gamma & for\ \tau < \tau_0 \\ \tau = K\dot{\gamma}^n + \tau_0 & for\ \tau \geq \tau_0 \end{cases} \quad (1.3)$$

Snow avalanches have also been modelled with a Bingham pressure dependent law called frictional fluid [8].In the specific case the yield threshold is defined as follows:

$$\tau_0 = c + p \sin \Phi \quad (1.4)$$

Where the internal friction angle Φ and the cohesion c derived from the Mohr-Coulomb failure criterion.

Besides the fluid constitutive laws, in the late 90's Lang and Harrison (1995) and Meschke et al. (1996) proposed another approach that consists in treating the snow in the same way used for soils. Cam-clay model was adopted and the results showed good agreement during isotropic compression and direct shear tests [3]
Meschke (1996), after the experience gained in laboratory, suggested to consider snow with a *"multisurface viscoplastic constitutive model for large strains and 3D states of stress"*[3] This model has 2 independent hardening mechanisms and 2 yield functions

The studies on the micromechanics of snow began with Brown (1980) and Hansen (1987) and were firstly based on the investigation of the interparticle phenomena that accounted in the deformation process. The research community agreed that the development and breakage of necks connecting the grains largely affected the mechanics.[3]
Brown and Hansen identified crucial characteristics of the ice matrix and proposed a constitutive theory based on *non-equilibrium thermodynamics with internal state variables*. [9]

That theory has been extended by Nicot (2003) correlating the spatial distribution of the bonds with the changes in the microstructure through a linear viscoelastic law. The model lacked a complete description of the micromechanics which also accounted for the sintering process and the neck deformations.

Cresseri in 2005, filled this gap and proposed a model that coupled the microstructure with the macro behaviour imposing a dependence of the hardening parameters with the sintering process. More precisely, following the modified Cam Clay model of Meschke (1996), she proposed a yield function of this type:

$$f = \left(\frac{q}{p_a}\right)^2 - \left(\frac{M}{p_a}\right)^2 [p(p_0 + p_m - p_t) + p_t(p_0 + p_m) - p^2] \tag{1.5}$$

Where $p_m$and $p_t$are the two hardening parameters related with the bonding degree, $p_a$the atmospheric pressure and p_0 the pre-consolidation pressure.

The time dependency and strain-rate sensitivity typical of snow was guaranteed by the overstress approach (Perzyna) which allows irrecoverable strains to take place also when $f < 0$. This is explained by the fact that in the pre-yielding the solid matrix undergoes at the same time sintering and neck deformations.

$$\dot{\epsilon}^{irr} = \frac{\gamma\sqrt{q^2 + p^2}}{p_0}\Phi(f)\frac{\partial g}{\partial \sigma}\frac{1}{|\nabla g|} \tag{1.6}$$

The viscous nucleus $\Phi(f)$ defined as follows:

$$\Phi(f) = e^{\alpha f} \; with \; \alpha > 0 \tag{1.7}$$

The plastic potential g resembles the shape of the yielding function

$$g = q^2 - M^2[p(p_{gc} - p_{gt}) + p_{gt}p_{gc} - p^2 \tag{1.8}$$

And for simplicity $p_{gc}$and $p_{gt}$are assumed to be linearly dependent

The evolution of p_t , p_0 and p_m depend on a scalar measure of bonding, the sintering, the temperature and the irreversible strains. The reader can find the empirical formulations on those parameters in the PhD study of Cresseri [3].

All the previous models assumed the material properties of snow to be constant within the layer; that assumption is now being overcome by the on-going research.

In 2008, J.Gaume et Al. proposed an elastoplastic model with a strain-softening plastic flow rule which is able to capture the interaction between slab and weak layer [10]. Such a unified model is of paramount importance and opens new paths for the snow constitutive modelling. So far, for instance, the release of slab avalanches was poorly captured by the normal models which failed in reproducing the collapse of porous cohesive material under compression. This softening rule, coupled with a cohesive Cam Clay model, has been demonstrated able to well describe the bond breaking in the weak layer and the grain rearrangement of the slab.

Figure 1.11 better explains the scheme used and it can be summarised as follows:

1. The stresses in the weak layer increases elastically until they reach the cohesive yield surface (Figure 1.11 b, points 1-2)
2. Even under compression, the yield surface shrinks and reaches the origin of the p-q space (Figure 1.11 b, point 2*)
3. The yielding surface, now cohesionless, expands again following the traditional hardening rule typical of frictional and compaction behaviour (Figure 1.11 b, point 3*)

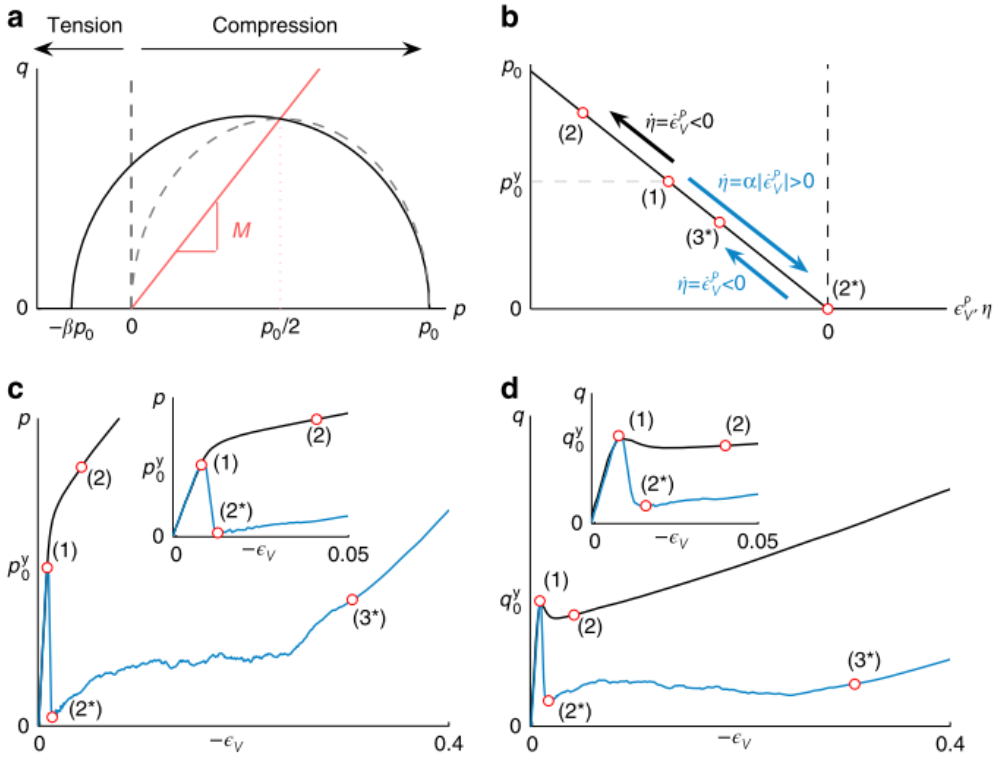

Figure 1.11 Overview of the elasto-plastic model [10]
a) yielding surface with cohesion (black line) and without (dashed grey line) b) Traditional hardening law (black arrow) and the softening formulation for the weak layer (blue arrow) c) $p - \varepsilon_v$ and $q - \varepsilon_v$ (d) curves for the classical hardening law (black) and the new one (blue)

1.5 Classification and snow avalanche typologies

"*A snow avalanche is a rapid flow of snow along a slope with a volume more than 100m³ and a path length of more than 50m*" [2].

Dry snow avalanches can be described dividing the flow into three regimes: a dense snow core, a fluidized layer and a turbulent suspension of snow. The dense snow core flows at the bottom of the avalanche and has a density in the order of 300 Kg/m³ with typical depths of 1-2m. On top of this layer there is a fluidized stratum in which the particles are not in persistent contact and move with higher velocities than the core. Typical densities are in the range of 10-100 Kg/m³ and depths are 2-5m [11]. Powder clouds are present when the density of the snow before the release is similar to that of fresh snow (100-120 Kg/m³) or when the flow reaches relevant speeds (>30m/s). This plume of turbulent snow and air mixture can reach height from few tens of meters to 100m and the density is on the order of 3 Kg/m³ [11]. The distinction of the three regimes is not sharp but is easily evidenced from the impact measurement on structures.

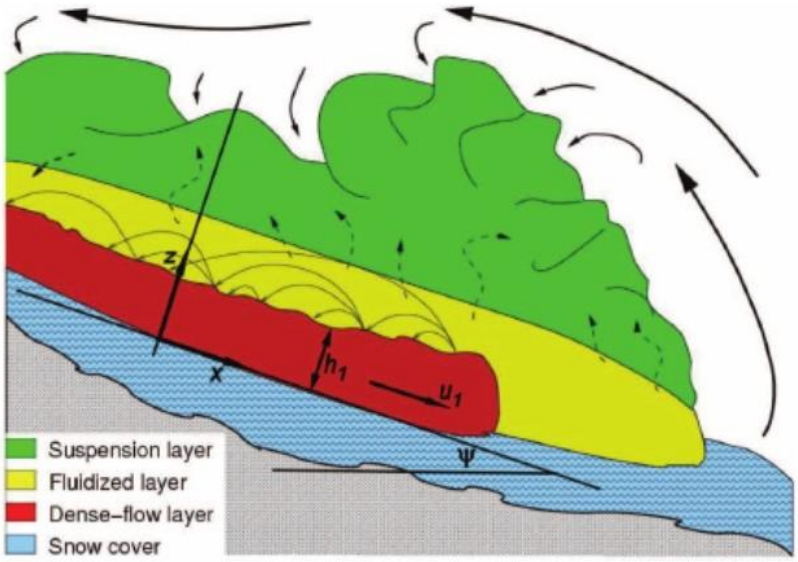

Figure 1.12 Schematic representation of the 3 flow regimes in dry snow avalanches [11]

In avalanche science, considering the high variability of events, having a classification based on characteristics of the phenomenon is of fundamental importance. UNESCO since 1981 has provided an International Avalanche classification in which avalanches are grouped according to common features in these characteristic zones: release zone, flowing zone and deposition.

- **Release zone** is the place where the phenomenon starts. Usually it is located in the nearby of ridges above the vegetation level, or in those places where snow accumulates due to precipitation and wind transport.

  In order to have a release the slope must be at least inclined 30°. At slopes higher than 50° the snow accumulation is not likely [2]. Other influencing factors are the terrain morphology, the vegetation, the overload, the meteorological history and the exposition of the slope.

  Depending on the initiation, an avalanche is defined as either a *loose snow avalanche* or a *slab avalanche*. Loose avalanches are triggered in a specific point and they are confined to surface snow layers while the slab avalanches are released simultaneously over a large area and they involve one or more layers of cohesive snow. The latter can be identified easily by the presence of a defined fracture line that confines the release zone.

  The role of vegetation and forest need to be mentioned since they play an important function in the release prevention [2].More specifically the retention of snow with the tree trunks increases the friction between the snowpack and the substratum.It furthermore affects the deposition of snow.during the snowfall creating irregular patterns.

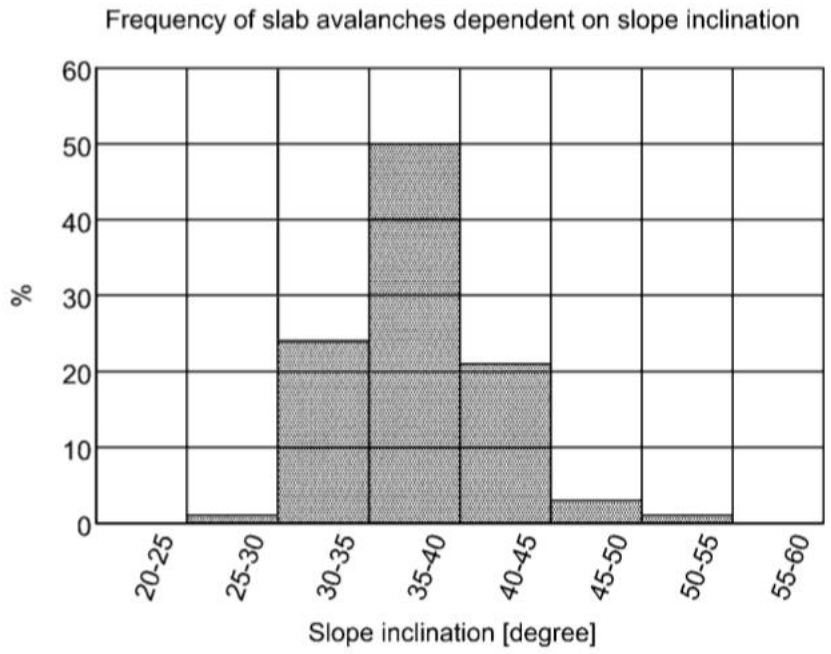

Figure 1.13 Frequency of slab avalanches as function of slope inclination [2]

- The **flowing zone** is the area between the release and the stop condition. This is the zone where the highest speed of the avalanche is registered.

  In this phase, depending on the characteristics of the flow there is a distinction between *flowing avalanches*, the material is concentrated in a "core" at the bottom, *powder avalanches* characterised by a low-density snow cloud and a version in-between the two called *mixed motion*.

  The avalanche can move towards the valley in a well-defined channel (*channelled avalanche*) or on an open slope (*open-slope avalanche*). During the flow it can also entertain trees or stones depending on the magnitude of the event and the type of snow. *Wet-snow avalanches*, for instance, are distinguished from *dry snow avalanches* because of the much higher friction at the sliding surface that often causes the formation of grooves and the entertainment of rock and dirt.[12] Entertainment works to slow avalanche motion by two effects. First,

the new snow which is picked up is at rest and therefore the effect is to decrease the overall momentum. Second, it modifies the bottom of the flow increasing the basal surface friction [12]

The propagation of every type of flows is mainly governed by the resistive forces that arise from the interaction of the dense core with the sliding surface at the bottom and the snow dust with the ambient air at the top. Resistive forces at the bottom account nearly for all the total friction except those cases of very high speed where the friction on the upper portions may contribute.

Sliding friction takes the form of collision and frictional rubbing between snow particles that in some cases have been demonstrated causing heat and production of small amount of waters on the surfaces of particles. [13]

Air between snow particles at the base of flowing avalanches has been proved not having influence in the friction process because of the relative low density of air compared to the particles (<1%) and the absence of turbulence phenomena for flows with a similar porosity (n=0.2-0.5).[12]

Usually wet-snow motion follows terrain features much more readily to dry snow because of the higher friction and adhesion to the slope.

The avalanche release volume ranges from a few to thousand cubic meters. SLF considers a small avalanche when the volume is smaller than 25000m^3, medium 25000< V(m^3) <60000 and large >60000. Regarding densities, the prevalent range is between 100 and 350 Kg/m^3 (Mc Lung & Schaerer [12]).

- Deposition or **runout zone** is the area where the snow mass progressively slow down and stops. Typical slope angles where avalanches decelerate are 15° or less. Observations of avalanche paths indicates that terrain variations such as gullies or boulders, also create favourable conditions for snow deposition [1]

The characteristics of debris in avalanche deposit depend on the hardness and moisture content of the snow that originally released. A hard slab usually has large chunks of debris whereas soft slab breaks into smaller pieces and balls. In general, the farther the avalanche travels, the smaller are the particles in the runout zone. Another common feature of dry debris is that the average size of the particles decreases with depth into the deposit and the shape is more rounded. This is due to the basal shearing and leads to an increase of density which can be up to five times the value of the starting zone.[2] Debris from wet avalanches are generally larger, with boulders up to 0.5m, and harder if the water on the surface freezes.

Figure 1.14 Example of a dry snow slab avalanche [14]

Figure 1.15 Deposition front of a wet snow avalanche [15]

As previously evidenced, there are lots of variables playing in the avalanche phenomenon, so hereafter is proposed a table with the criteria summarized. (Praolini et Al.)

Type of release	**Position of the sliding surface**	**Humidity of the snow**	**Shape of the path**	**Type of movement**	**Triggering cause**
loose snow avalanche	Surface layer	Dry-snow	Open slope	Powder avalanche	Spontaneous
slab avalanche	Full depth	Wet-snow	Gully	Flow avalanche	Triggered
				Mixed avalanche	

Table 1.1 Classification of snow avalanches proposed by Praolini et Al. [2]

CHAPTER 2
STATE OF THE ART: ANALYTICAL AND NUMERICAL MODELS

2.1 General remarks

As expressed in the first chapter, snow shows a large variability and when it comes to mathematically describe the avalanche movement many difficulties arise. So far, a complete and accurate model reproducing the behaviour at micro and macroscale from the triggering to the deposition has not yet been developed.

Here below a description of the typical parameters present in the avalanche models and how they change with respect to the position of the flow.

The movement is characterized by:

1. **The velocity v** usually has the highest values in the front of the avalanche and then it reduces in the body and the tail. It varies with mass, depth and distance travelled down the slope.

   Most of the vertical speed profiles show a pronounced shear layer at the bottom and a region of little or no shear above.[16], [5] and [17]. In a first approximation velocities of the avalanche depend (1) on the release volume and entrained or deposited snow, (2) the external friction at the top and bottom of the avalanche and (3) the morphology of the terrain (length, vertical drop).[12]

It is also expected that avalanche speeds are higher when the flow is confined to gullies than for open-slope flows. This is because the same amount of material is forced through a confined space and therefore the speed must increase. Also, velocities are higher at the center of the gully than at the sides due to lateral friction.

From Issler (2003) study was found that peak speeds of dense snow avalanche vary from 20 to 60 m/s [18].

2. **Flow height *h*** is very sensitive to the spatial distribution of the mass. There are only a few measurements on avalanche flow heights and they were collected by putting switches on a mast that are triggered by the flow (Vallè de la Sionne [19])

   From the experiments performed in the Pizzac Site [20] it was shown that among two avalanches of equal mass, that one with more mass concentrated at the front had higher velocity and reached longer runout distance. The maximum flow heights are generally located some tens of meters behind the front. However, when the avalanche runs on a steep track (35– 40°), the maximum heights move forward, closer to the avalanche front.

   Maximum height position usually match with maximum impact pressures. Exceptions are due to the presence of a powder cloud moving at the front of the avalanche.

3. **Mass density** ρ is a leading factor in the evaluation of the momentum equations. The density of a dry flowing avalanche is supposed to be in the range between 100 to 300-400 kg/m^3 (Hopfinger, 1983; Hutter, 1996; Ancey, 2001).

   The density of the deposited snow can be from 2 to 5 times higher than the density of the snow in the release area. It is still not clearly known in which phase this compaction takes place [12].

4. **Runout distance**

The run-out zone is defined as *"the point of farthest reach of the debris"* [12]. Voellmy defined the run-out zone as the part of the avalanche track where the inclination is below 15◦. The value of 15◦ has been chosen because the repose angle of flowing snow is supposed to be slightly higher than 15◦[2]

That is just an assumption and "*usually any observable clues at the site are given priority over the models due to the complexity of the problem and the uncertainties"* [12].

Important clues normally include sign of damaged vegetation or aerial and satellite photos.

5. **Pressure**

Impact pressures range from relatively harmless blast of powder clouds to the destructive forces of a full-scale flowing avalanche. Generally, dry flowing avalanches have a combination of high density and speed which results in very high impact effects.

From data of site tests [19], [21] peak pressures are found to be from two to six times higher than the average pressure during the impact. Maximum forces come near the front of the avalanche.

The impact, on a first approximation can be expressed through equation (2.1)

$$I \approx \rho v^2 \tag{2.1}$$

Density ρ of the mixture depends on the concentration of solid material

$$\rho = \rho_s n + \rho_A (1 - n) \tag{2.2}$$

Where $\rho_A \approx 1\, Kg/m^3$ and ρ_s ranges from 200 to 917 Kg/m^3.

Porosity n of flowing snow is estimated $\approx 0.3 - 0.5$ and therefore the density of the mixture results $200 \leq \rho \leq 550\ \ Kg/m^3$[12]

2.2 Literature review about snow propagation models

In literature several attempts of giving an overview of all the current propagation models were carried (Mellor, Perla, Hopfinger, Harbitz). SAME project [2] showed that avalanche models can be divided into two big families:
empirical and **deterministic models**.
There are then separate models depending on the type of avalanche (powder, flow or wet)

2.2.1 Empirical methods

These models are based on statistical elaboration of past event data, without taking into account the physics of the problem. The advantages of such empirical models are the simplicity in estimating the run-out distance and the fact they try to quantify the uncertainties. On the contrary they cannot determine velocity, flow depth and pressure.
Several statistical methods have been proposed [22] and they all rely on the correlation between topographic parameters and run-out distance through a regressive analysis (topographic-statistical models) or through the nearest neighbors method (comparative models).
An example of the topographical-statistical models is the αβ-model[23] which relates the inclination of the total avalanche path α to the slope β that is the inclination between the starting point and the point with 10° slope along the terrain profile.

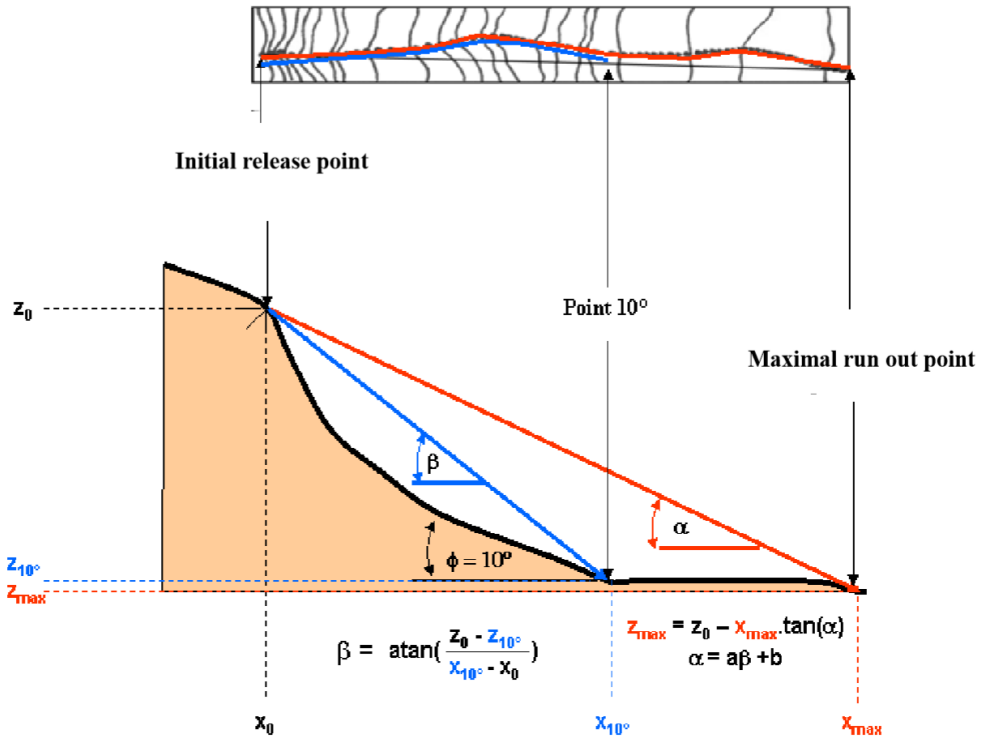

Figure 2.1 Topographic parameters describing the αβ-model

The relation is linear and follow this law:

$$\alpha = m\beta + c \tag{2.3}$$

Typical values of the parameters m and c can be found in the Italian snow guidelines [22]

Particular care must be paid while using these models because as mentioned in [24] "*Although statistical methods have been extensively used throughout the world over the last twenty years and have given fairly reliable and objective results, many cases exist in which their estimates are wrong*.

There are also models based on the adaptation of distribution probability laws like Extreme Value or Gumbel to runout distances.[25]

The comparative methods use a multi-variate statistic and find the dependent variables knowing the independents in a multi-dimensional space.

2.2.2 Deterministic (dynamical) models

The deterministic models quantify the base mechanism which affects the avalanche motion. Each avalanche can be approached at different scales, the largest consider the entire flow and leads to the simplest sliding block models while the smallest is close to the size of the grains and leads to complex rheological and numerical problems. [24]
There are also intermediate models called quasi three-dimensional models that are obtained integrating the motion equations across the flow depth.
Disregarding the models related to the airborne avalanches, the earliest model dates back to the Olympic Games at Chamonix in 1924 when the Swiss professor Lagotala computed the velocity of an avalanche in the Pelerine area [26].
The model was then extended by Voellmy (1955) and became the most used method all over the world [27]. This model follows the sliding block approach where the flow is subjected to a friction force f_R:

$$f_R = \rho g \frac{u^2}{\xi} + \mu \rho g h cos\theta_s \qquad (2.4)$$

With m denoting the mass, ρ the density, u the velocity, h the flow depth, θ_S the average slope of sliding area and μ and ξ two friction parameters.
More precisely μ accounts for the snow fluidity and range from 0.15 to 0.4 depending on the avalanche size [28].
ξ reflects the influence of the path (400 for open slopes and 1000 or more for gullies)

The main hypothesis of the Voellmy model is to make an analogy of the sliding zone of the avalanche with the hydraulic open channel flows. Avalanche is therefore considered as an incompressible fluid, infinitely extended that after a short acceleration reaches a condition of uniform flow. Maximum velocity reached in the sliding zone can be calculated equaling (2.4) with (2.5)

$$f_D = \rho g h sin\theta_s = f_R \tag{2.5}$$

And follows

$$u = \sqrt{\xi h(sin\theta_s - \mu cos\theta_s)} \tag{2.6}$$

Runout analysis is performed considering a block on a constant slope $tg\theta_a < \mu$ having already identified the part of the slope where most likely the flow will stop.

The evaluation of the run-out distance proposed by Voellmy considers an energy balance of the work dissipated by the frictional forces and the loss of mechanical energy. The expression proposed in [22] is the following:

$$X_R = \frac{u^2}{2g(\mu cos\theta_a - sin\theta_a) + \frac{gu^2}{\xi h}} \tag{2.7}$$

This model in 2002 has been extended to a continuum model called AVAL 1D [2] and from 2005 to the more complex RAMMS [2]

In this last model the snow is an unsteady and non-uniform flow, described through the depth-averaged mass (2.8) and momentum balance equations(2.9) (2.10) as follows:

$$\partial_t H + \partial_x(HU_x) + \partial_y\big(HU_y\big) = \dot{Q}(x, y, t) \tag{2.8}$$

Where $\dot{Q}(x, y, t)$expresses the mass entertainment or deposition rate

The two components of the depth-averaged momentum equations are:

$$\partial_t(HU_x) + \partial_x\left(c_x HU_x^2 + g_z K_{a|p}\frac{H^2}{2}\right) + \partial_y\big(HU_x U_y\big) = S_{gx} - S_{fx} \tag{2.9}$$

$$\partial_t\big(HU_y\big) + \partial_y\left(c_y HU_y^2 + g_z K_{a|p}\frac{H^2}{2}\right) + \partial_x\big(HU_x U_y\big) = S_{gy} - S_{fy} \tag{2.10}$$

The right-hand side is the difference of the gravitational and the typical Voellmy frictional force

$$S_{gx} = g_x H \;\; and \;\; S_{gy} = g_y H \tag{2.11}$$

$$S_{fx} = n_{U_x}\left(g\frac{\|U\|^2}{\xi} + \mu g_z H\right) and \;\; S_{fy} = n_{U_y}\left(g\frac{\|U\|^2}{\xi} + \mu g_z H\right) \tag{2.12}$$

Being n_{U_x} and $\|U\|^2$:

$$n_U = \frac{1}{\|U\|}\left(U_x, U_y\right)^T \tag{2.13}$$

$$\|U\|^2 = U_x^2 + U_y^2 \tag{2.14}$$

c_x and c_y of the equations (2.9 and (2.10) denote two correction factor to account for shear gradients and non-rectangular velocity profiles but their influence is rather insignificant [29].

$K_{a|p}$ is a proportionality factor between the vertical and horizontal normal stresses. Usually is set to 1 [29] because, as the previous case, it has little influence on the final runout distances and velocities. It is defined as follows:

$$K_{a|p} = tan\left[45° \mp \frac{\phi}{2}\right] \tag{2.15}$$

Where ϕ is the internal friction angle assuming a Mohr Coulomb model on the vertical stress distribution.

RAMMS model has also been extended to a treatment called RKE which adds a term of random energy to account for the influence of the velocity fluctuations on the depth-averaged flow.

Numerical solution of RAMMS Voellmy model or a better treatment of RKE are out of the scope of this thesis and can be found in the studies of Bartelt and Buser (2009)[18,19]

Among the continuum models, the main variations accounts for the constitutive modelling of snow. There are many experimental studies [31][5][7] on the rheological examination of snow and it is common opinion that snow is a non-Newtonian viscoplastic material. Some of the constitutive equations proposed are for instance: Newtonian fluid, Bingham fluid, frictional Coulombic fluid.

Hutter and Savage [32],[33] showed that assuming snow a dry granular flow and describing it through a Coulomb law it well captures steep smooth inclined channels.
Sometimes the significant variations in the material caused by a small change of air temperature or the diversity of snow consistency with the size scale, allows the simple models to be preferred to more refined and complex rheological laws.
The reader must consider that validation of complex models is extremely difficult because of the lack of local experimental data and the scarce representativity of the tests performed at laboratory scale. On the contrary simple models can be validated through a back analysis considering global parameters (geometry features of the avalanche and velocity along the slope) that generally are easier to collect from site experiments [19], [34][21].

2.3 Review of numerical models for granular flow

The previous treating showed the reader a framework about the models specifically developed for snow applications. This chapter wants to explore more generic numerical approaches used for similar problems so that the Material point method, employed in the empirical part, can be contextualized. In the following page a series of deterministic models will be presented with their pros and cons.

The models used to describe granular flows can be grouped into two big families: the discrete and the continuum models.

Discrete models have been developed since the late 50s and they aim in describing the medium at the microscopic scale. The most common method is the Discrete element method (DEM); the material is discretized in particles that move according the Newton's laws of motion and interact between each other. The behavior depends on the type of particle contact

and on the interaction with the surrounding fluid. DEM is a very promising method to study granular materials but, due to the high computational effort for real scale application, it is rarely applied to the engineering practice. [35]

On the other hand, the **continuous models** treat the medium as a continuum and the governing equations can be expressed according to the Lagrangian or Eulerian formulations.
Different approaches are used to subdivide the domain and solve the equations leading to the fundamental division of **mesh-based methods** (FDM, FEM) and **particle-based methods** (SPH, MPM, PFEM).

Both finite difference methods (FDM) and finite element methods (FEM) consist in discretizing a continuous domain into sub domains which are called elements. The former, generally, is applied to computational fluid dynamic problems while the latter for structural mechanics applications.
From the 60's and 70's FEM has been developed and released in many forms but the main versions are two and depend on the coupling or uncoupling of the mesh with the material (Eulerian and Lagrangian FEM). In the Eulerian FEM the computational mesh is fixed while the material deforms in time. The method does not suffer any mesh distortion but it cannot handle history-dependent material. On the contrary Lagrangian FEM deforms its mesh as the material moves and has the advantage of giving the possibility to deal with history dependent materials. However, in some circumstances, large deformations leads to a cumbersome mesh distortion and misleading results.[35]

Particle based methods discretize the continuum with a collection of material points that carry the physical properties. This strategy allows to overcome the mesh distortion problems typical of mesh-based methods
Many versions have been developed; here just those methods that were the basis for the derivation of the Material point method will be reported.

The Particle Finite Element Method (PFEM) has been developed in 2004 and consists in using the FEM for the discretization and integration of the equations. Contrarily to classical version, nodes of the mesh behave as particles and transport the physical properties. Then at every end of the time step, the mesh is regenerated through a Delaunay Tessellation [35].

The Smoothed Particle Hydrodynamics (SPH) discretize the domain in a cloud of particles but does not need any type of mesh because the physical properties of the points are weighted through a kernel function depending on the distance and density of the neighbor particles.

2.4 Material point method

The material point method (MPM) is a method in between the particle-based methods and the Finite Element Method. [8]
It was developed in the 90's by Sulsky and Schreyer as an extension of the fluid implicit particle method (FLIP) [9].

This method allowed to solve at the beginning solid mechanic problems and extreme loading conditions. It has been used, as example, for large deformations problems as penetration [10], collision [11], crack propagation [12] and granular flow [13].
Compared to the standard Lagrangian FEM, MPM allows to model successfully large deformations problems because it does not suffer any severe mesh distortion that lead to inaccurate results.
In 2013 there has been a big resonance within the research community because it was used for the animation of the Disney movie "Frozen" and its potential was publicly recognized [14].
Few years later the Swiss institute for snow and avalanche research (SLF) started a project to adapt this model with accurate physically-based constitutive law in order to simulate snow slab avalanches [15].

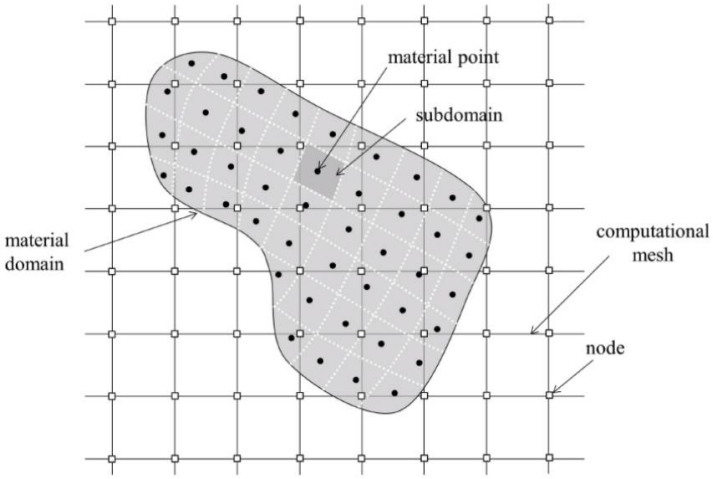

Figure 2.2 MPM Space discretization [5]

MPM, as shown in Figure 2.2 MPM Space discretization [5], consists in discretizing a continuum body Ω with a finite set of n_p material points. Each particle represents a portion of the total mass and carry variables such as position, velocities, strains and stresses. Material points form therefore a Lagrangian frame of reference while the domain in which they are moving is Eulerian. Finite element mesh is fixed and it is basically used just to solve the equations of motion. [38]

The variables needed are transferred first from the material points to the nodes of the grids through shape functions [5]. Then, after having set the boundary conditions at the particle or at the mesh nodes, the governing equations are solved at the grid level (Figure 2.3 Calculation steps of MPMb).
The incremental change in nodal velocity is then updated and transferred to the MP location (Figure 2.3 Calculation steps of MPM through the same shape functions.
Stresses and state variables are consequently computed accordingly to the constitutive material chosen. Final step of the iteration consists in updating the particle velocity and position (Figure 2.3 d)
The information at the mesh level can be discarded and the procedure starts its iteration avoiding any kind of mesh distortion [5].

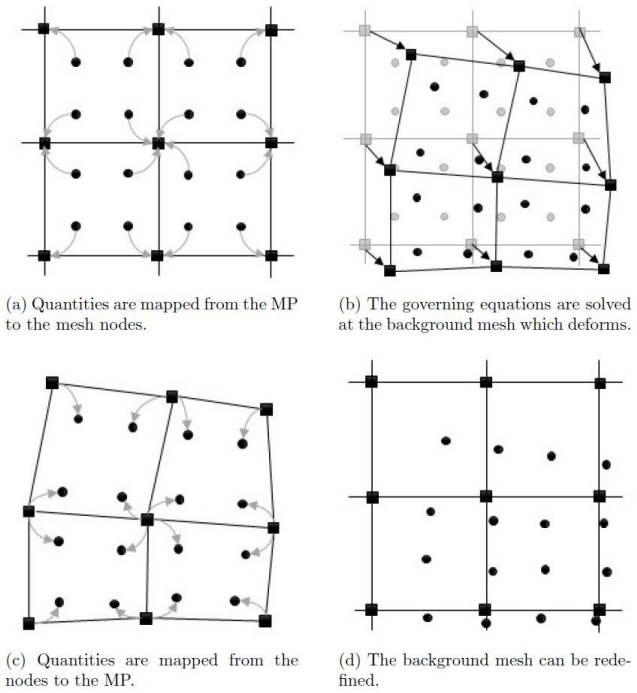

(a) Quantities are mapped from the MP to the mesh nodes.

(b) The governing equations are solved at the background mesh which deforms.

(c) Quantities are mapped from the nodes to the MP.

(d) The background mesh can be redefined.

Figure 2.3 Calculation steps of MPM

2.4.1 Formulation of the single-phase MPM

In this chapter the formulation of the one phase MPM will be presented together with the computation scheme adopted by the code Anura3D.
Material point method has a lot in common with FEM, actually one can be seen as an extension of the other.
The two methods share the weak form of the governing equations that derives from the conservation of momentum

$$\int_{\Omega} \delta v_s \rho \frac{dv_s}{dt} d\Omega = \int_{\delta\Omega_\sigma} \delta v_s \tau_s dS + \int_{\Omega} \delta v_s \rho g d\Omega - \int_{\Omega} \delta v_s \frac{\partial \delta v_s}{\partial x_i} \sigma_{ij} d\Omega \qquad (2.16)$$

With δv_s indicating the test function or virtual velocity, ρ the density and $d\Omega$ the boundary of the domain. Ω_σ and τ_s are respectively the boundary and the stress if a traction condition is applied and σ_{ij} the stress tensor.

Equation (2.16) states therefore that the inertia at the left hand is equal to the sum of external forces, body forces and internal forces.
Strains and stress tensors are represented in vector form, taking advantage of the tensor's symmetry

$$\varepsilon(x,t) = [\varepsilon_{11}\ \varepsilon_{22}\ \varepsilon_{33}\ 2\varepsilon_{11}\ 2\varepsilon_{23}\ 2\varepsilon_{31}]^T \tag{2.17}$$

$$\sigma(x,t) = [\sigma_{11}\ \sigma_{22}\ \sigma_{33}\ \sigma\varepsilon_{11}\ \sigma\varepsilon_{23}\ \sigma\varepsilon_{31}]^T \tag{2.18}$$

As in FEM, nodal displacement, velocity and acceleration are approximated through shape functions

$$u(x,t) \approx \overline{N}(x)\hat{u}(t) \tag{2.19}$$

$$v(x,t) \approx \overline{N}(x)\hat{v}(t) \tag{2.20}$$

$$a(x,t) \approx \overline{N}(x)\hat{a}(t) \tag{2.21}$$

The kinematic relation can be written as:

$$\dot{\varepsilon}(x,t) = Lv(x,t) = LN(x)\hat{v}(t) = B(x)\hat{v}(t) \tag{2.22}$$

With L being a linear differential operator and B having the following form:

$$B_i(x) = \begin{bmatrix} \frac{\partial \overline{N_i}(x)}{\partial x_1} & 0 & 0 \\ 0 & \frac{\partial \overline{N_i}(x)}{\partial x_2} & 0 \\ 0 & 0 & \frac{\partial \overline{N_i}(x)}{\partial x_3} \\ \frac{\partial \overline{N_i}(x)}{\partial x_2} & \frac{\partial \overline{N_i}(x)}{\partial x_3} & 0 \\ 0 & \frac{\partial \overline{N_i}(x)}{\partial x_3} & \frac{\partial \overline{N_i}(x)}{\partial x_2} \\ \frac{\partial \overline{N_i}(x)}{\partial x_3} & 0 & \frac{\partial \overline{N_i}(x)}{\partial x_1} \end{bmatrix} \tag{2.23}$$

The weak formulation (2.16) in matrix form yields to:

$$Ma = F^{\text{ext}} + F^{grav} - F^{int} \tag{2.24}$$

$$\int_{\Omega} N^T \rho N a d\Omega = \int_{\partial\Omega_r} N^T \tau dS + \int_{\Omega} N^T \rho g d\Omega + \int_{\Omega} B^T \sigma d\Omega \tag{2.25}$$

At this stage the main difference between FEM and MPM arises:
in FEM the integration is carried out using the Gaussian quadrature while in MPM the quadrature points coincide with the material points n_p and the weight is associated to their volume Ω_p.

$$\int_{\Omega} B^T \sigma d\Omega = \sum_{p=1}^{n_p} \Omega_p B^T(x_p)\sigma_p \tag{2.26}$$

Mass matrix M depends on the position of the material points and on their mass. At the initialization stage every material point has the same portion of the element volume.

$$\Omega_p = \frac{1}{n_{ep}} \int_{\Omega_e} d\Omega \tag{2.27}$$

Where Ω_p represents the particle volume and n_{ep} the number of particles within the element

Equation (2.27) confirms that, at the initialisation, each MP has the same mass within the element, i.e.

$$m_p = \Omega_p \rho_p \tag{2.28}$$

In which ρ_p denotes the mass density of the material belonging to the particle p

Mass matrix to solve equation (2.24) has to be inverted and, for computational purposes, considered in a diagonalized form called lumped mass matrix. It is defined as follows:

$$M = \int_{\Omega} N^T \rho N d\Omega = \sum_{p=1}^{n_p} m_p N^T(x_p) N\,(x_p) \tag{2.29}$$

External and gravity forces are calculated as:

$$F^{trac} = \sum_{p=1}^{n_p} N^T(\xi_p)\, \mathrm{f}_{\mathrm{p}}^{trac} \tag{2.30}$$

$$F^{grav} = \sum_{p=1}^{n_p} N^T(\xi_p)\, \mathrm{f}_{\mathrm{p}}^{grav} \tag{2.31}$$

The traction force $\mathrm{f}_{\mathrm{p}}^{trac}$ indicates the external force vector which is acting on the material points close to the element border.

$$f_p^{trac} = \tau_e(x_p)\frac{S_e}{n_{ebp}} = \frac{S_e}{n_{ebp}} \sum_{p=1}^{n_{tri}} N_i(\xi_p)\tau_e(x_i) \tag{2.32}$$

With n_{ebp} denoting the number of MP situated next to the loaded surface S_e

The other part of the external forces is the gravity force $\mathrm{f}_{\mathrm{p}}^{grav}$ that is computed in the following way

$$\mathrm{f}_{\mathrm{p}}^{grav} = m_p g \tag{2.33}$$

The equation (2.24) is discretized in time by replacing the differentials in the ODE by finite difference quotients, i.e.:

$$a^t = M^{t^{-1}}(F^{ext,t} + F^{grav,t} - F^{int,t}) \tag{2.34}$$

$$v^{t+\Delta t} = v^t + a^t \Delta t \tag{2.35}$$

The explicit scheme is conditionally stable, and the threshold is set by the critical time step which depends on minimum length of the element mesh l_e and on the velocity of the compression wave in the material c_p

$$\Delta t_{crit} = \frac{l_e}{c_p} \tag{2.36}$$

$$c_p = \sqrt{\frac{E_c}{\rho}} \tag{2.37}$$

The term E_c in equation (2.37) is the constrained compression modulus that for elastic material is expressed as:

$$E_c = \frac{(1-\nu)}{(1+\nu)(1-2\nu)} E \tag{2.38}$$

In the code Anura the parameter responsible to change the time step is the Courant number C. It has crucial role when processes are highly dynamic and energy conservation is important while in quasi static conditions it can be set close to the value 1 (C=0.98).

$$C = \frac{\Delta t}{\Delta t_{crit}} \tag{2.39}$$

2.4.2 Single step solution algorithm

This paragraph will show the computational cycle to solve the governing equations. It consists in a series of steps to update the situation of a continuum form time t to time $t + \Delta t$. [7,10]

1. The nodal mass is calculated through the shape functions and the lumped mass M^t is assembled. Through equations 2.11, 2.15 and 2.16 the internal and external forces are evaluated.

2. The momentum equation (2.24) is solved for the nodal acceleration

$$a^t = M^{t^{-1}}(F^{ext,t} + F^{grav,t} - F^{int,t}) \tag{2.40}$$

3. The material point velocities are updated through nodal accelerations and shape functions

$$v_p^{t+\Delta t} = v_p^t + \sum_{i=1}^{n_{nodes}} N_i(\xi_p^t)\, a_i^t\, \Delta t \tag{2.41}$$

4. The nodal momentum is updated, and the nodal velocities are computed

$$M^t v^{t+\Delta t} \approx \sum_{p=1}^{n_{ep}} m_p N^T(\xi_p^t)\, v_p^t \tag{2.42}$$

5. The incremental nodal displacement is calculated

$$\Delta \mathrm{u}^{\mathrm{t}+\Delta t} = \Delta t v^{t+\Delta t} \tag{2.43}$$

6. The strain increment at the material point location follows as

$$\Delta \varepsilon_{\mathrm{p}}^{\mathrm{t}+\Delta t} = B(\xi_p^t)\Delta u^{t+\Delta t} \tag{2.44}$$

   Strains are then multiplied for the chosen constitutive matrix to obtain MP stresses

7. The volumes associated with the material points are updated through the volumetric strain increment and the density is recomputed

$$\Omega_{\mathrm{p}}^{\mathrm{t}+\Delta t} = (1 + \Delta {\varepsilon_{vol,p}}^{t+\Delta t}) \quad \text{and} \quad \rho_{\mathrm{p}}^{\mathrm{t}+\Delta t} = \frac{\rho_p^t}{(1+\Delta {\varepsilon_{vol,p}}^{t+\Delta t})} \tag{2.45, 2.46}$$

8. Material point positions are updated considering

$$u_p^{t+\Delta t} = u_p^t + \sum_{i=1}^{n_{nodes}} N(\xi_p^t)\, u_i^{t+\Delta t} \tag{2.47}$$

9. The grid is reinitialized discarding the nodal values and detecting the new number of particles within each element. A new local position of each particle is computed through the shape functions.

2.4.3 Contact algorithm

The contact algorithm is fundamental in the propagation processes because it rules the energy dissipation of the flow and avoids interpenetration of material. In Anura it has been implemented as a predictor-corrector scheme at the nodal velocity level.

The algorithm first detects which are the contact nodes comparing the predicted velocity of the two single bodies to that of the combined system. Velocities are obtained from the momentum balance equations evaluated at the node k:

$$M_{A,k}^t \dot{v}_{A,k}^t = F_{A,k}^t \tag{2.48}$$

$$v_{A,k}^{t+\Delta t} = v_{A,k}^t + \Delta t \dot{v}_{A,k}^t \tag{2.49}$$

The same for the body B

$$M_{B,k}^t \dot{v}_{B,k}^t = F_{B,k}^t \tag{2.50}$$

$$v_{B,k}^{t+\Delta t} = v_{B,k}^t + \Delta t \dot{v}_{B,k}^t \tag{2.51}$$

And for the combined system

$$(M_{A,k}^t + M_{B,k}^t)\dot{v}_{sys,k}^t = F_{A,k}^t + F_{B,k}^t \tag{2.52}$$

$$v_{sys,k}^{t+\Delta t} = v_{sys,k}^t + \Delta t \dot{v}_{sys,k}^t \tag{2.53}$$

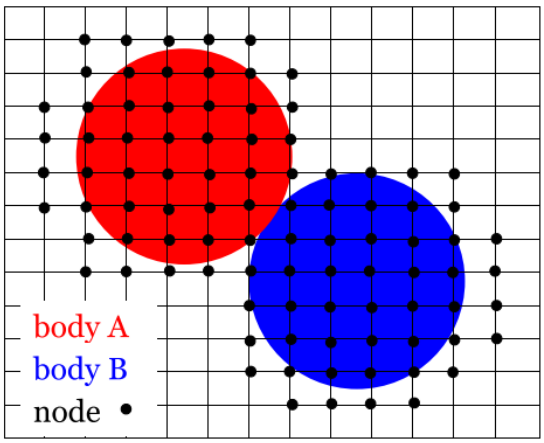

Figure 2.4 Contact algorithm scheme [39]

At this point if the velocities $v_{A,k}^{t+\Delta t} \neq v_{sys,k}^{t+\Delta t}$ means that the node is a contact node.

Once it is detected, as expressed in Figure 2.5, the algorithm checks if the bodies are approaching or separating. This task is performed comparing the normal component of the single body velocity with the normal component of the velocity of the system.

If Eq (2.54) is fulfilled means that the two bodies are approaching and a correction is required.

$$\left(v_{A,k}^{t+\Delta t} - v_{sys,k}^{t+\Delta t}\right) \cdot n_k^t > 0 \tag{2.54}$$

Being $n^t$the unit outward normal to the body A

The predicted relative normal and tangential velocities are:

$$v_{norm,k}^{t+\Delta t} = [(v_{A,k}^{t+\Delta t} - v_{sys,k}^{t+\Delta t}) \cdot n_k^t] \cdot n_k^t \tag{2.55}$$

$$v_{tan,k}^{t+\Delta t} = n_k^t \times [(v_{A,k}^{t+\Delta t} - v_{sys,k}^{t+\Delta t}) \times n_k^t] \tag{2.56}$$

Two bodies which are sliding have a magnitude of tangential force which must be greater than a so defined force:

$$f_{tan,k}^{max,t+\Delta t} = f_{adh,k}^{t+\Delta t} + \mu |f_{norm,k}^{t+\Delta t}| \tag{2.57}$$

Where $f_{adh,k}^{t+\Delta t}$ is the adhesive force at the contact and $f_{tan,k}^{t+\Delta t}$ can be evaluated from the first Newton equation considering Eq.(2.56). The predicted single body velocity $v_{A,k}^{t+\Delta t}$ is corrected to a new velocity $\tilde{v}_{A,k}^{t+\Delta t}$ such in a way that the normal component coincides with the normal component of the combined bodies and the tangential force has the value of Eq.(2.57)

$$\overrightarrow{\tilde{v}_{A,k}^{t+\Delta t}} = \overrightarrow{v_{A,k}^{t+\Delta t}} + \frac{\overrightarrow{f_{tan,k}^{max,t+\Delta t}} + \overrightarrow{f_{norm,k}^{t+\Delta t}}}{m_{A,k}^{T}} \Delta t \tag{2.58}$$

Having calculated the velocity of the contact node $\tilde{v}_{A,k}^{t+\Delta t}$, the corrected acceleration (Eq (2.59)) is used to compute the velocities of MPs and update their position, strains and stresses. The contact algorithm is therefore applied between the Lagrangian phase and the convective phase.

$$\overrightarrow{\tilde{a}_{A,k}^{t}} = \frac{\overrightarrow{\tilde{v}_{A,k}^{t+\Delta t}} - \overrightarrow{v_{A,k}^{t}}}{\Delta t} \tag{2.59}$$

The basal friction and the contact algorithm are fundamental for propagation problems because, as it will be shown in chapter 3, they significantly modify the shape of the flow, the position of the front in time and the runout.

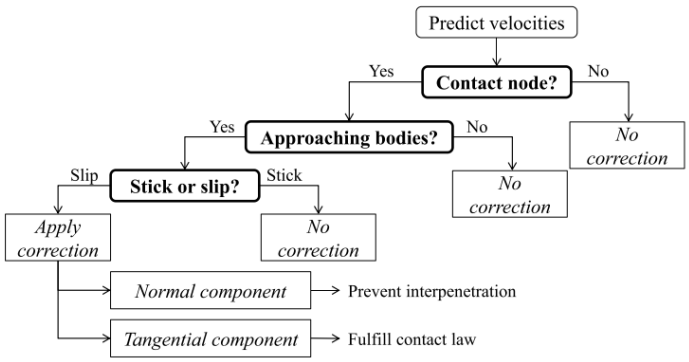

Figure 2.5 Flow chart illustrating the contact algorithm [57]

CHAPTER 3
NUMERICAL MODELLING AND RESULTS

3.1 Small scale

3.1.1 Introduction of the experiment

The purpose of the first stage of the thesis is to model with MPM a small-scale setup of the avalanche phenomenon and compare it to the experiments performed by Hutter in 1995 [32]. Through the experience gained with Anura MPM code, it was chosen to approach the problem starting from a two-dimensional condition able to capture the characteristics of motion from the release to the final run-out. The aim in this phase is to keep the treatment as simple as possible neglecting large-scale effects, and to explore the sensitiveness of the MPM model by changing the main numerical and mechanical parameters.

An elastic-plastic model with Mohr Coulomb failure criterion and Bingham constitutive law are used to model the snow behaviour. Both the models and the set of optimized parameters will be presented and commented.

Hutter' experiments were performed in a 100 mm wide chute made of two straight portions 1700 mm long and an arc radius connecting them (R=246 mm). As shown in figure 8 in the upper part of the channel the material is confined by a rotating gate that can be suddenly released and triggers the motion of the particles down the chute.

In his work he performed a series of tests changing the material of the particles (glass beads and PVC), inclination (40°,50° and 60°), bed lining

(drawing and sand paper) and total mass released (ranging from 500 to 1500g).

The side walls in every experiment were made of a smooth plastic material to keep the flow as much two dimensional as possible. [32]

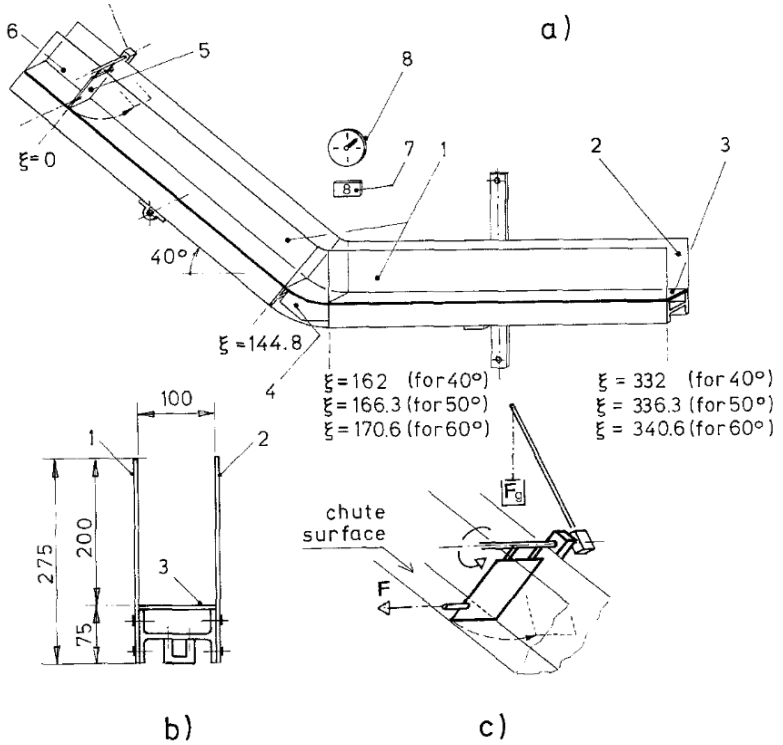

Figure 3.1 Side view (a) and cross section (b) of Hutter's set-up with different inclinations. In the right corner (c) the detail of the release system [32]

Hutter recorded through a camera the mass motion and, for each experiment, collected trail and leading-edge position and velocity. Unfortunately, as mentioned also in a previous study [40], the only result fully available is the experiment #87 and this last one will be used as a reference experiment to calibrate the MPM simulations.

Table 3.1 Experiment 87 setup

Experiment number	Material	Bed lining	Inclination of the chute (°)	Internal friction angle (°)	Bed friction angle (°)
87	Vestolen 1500g 950 Kg/m^3	Drawing paper	50	29	20-23

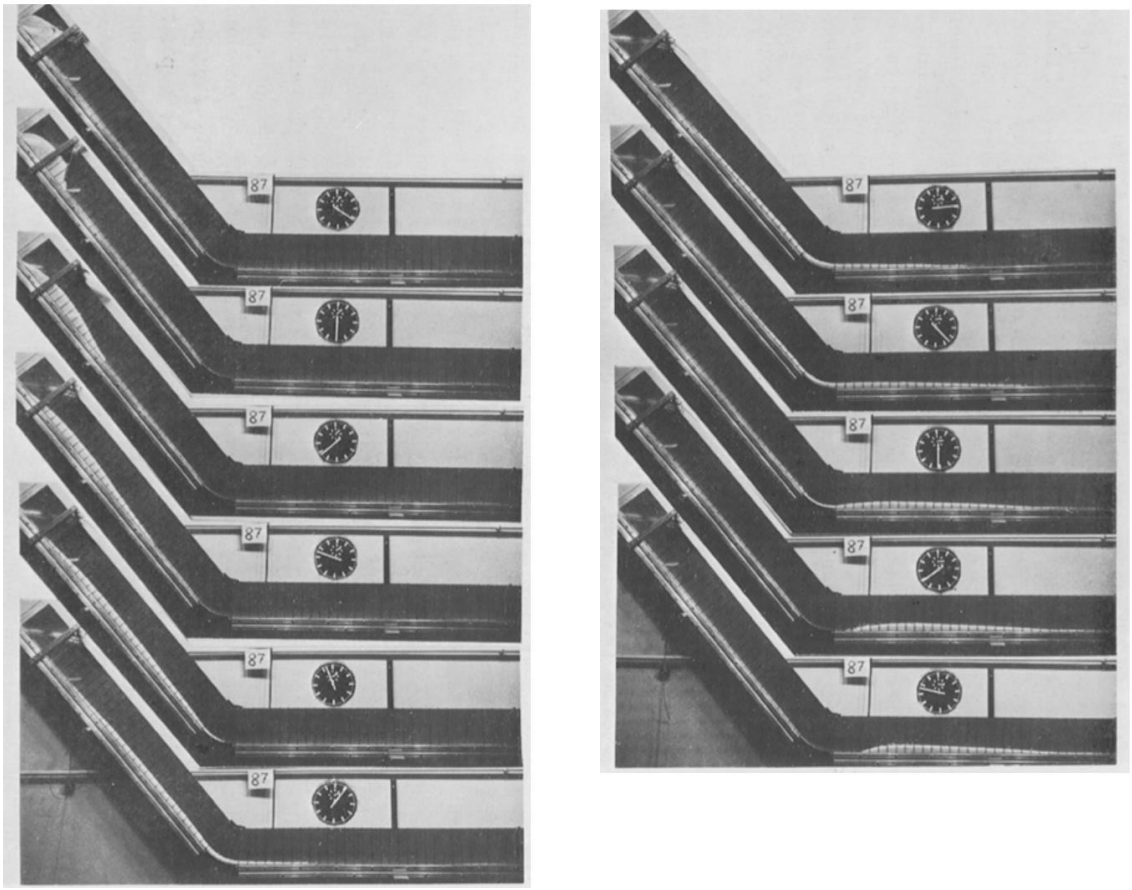

Figure 3.2 Series of pictures taken at different times during the experiment #87

3.1.2 MPM model

The numerical model of the chute has been built considering the problem 2D (plane strains) because the code is still too demanding in term of computational time when simulations have large scale. The aim is therefore to evaluate both at the small and real scale the accuracy of the 2D model.

As a first approximation the non-linear behaviour of snow has been described with an isotropic elastic-perfectly plastic model with Mohr-Coulomb failure criterion. The constitutive law of the base, on the contrary, does not affect the dynamic of the avalanche because it works just as a medium to apply the contact algorithm.

Here below in Table 3.2 are shown the material constitutive parameters adopted in the simulations with Mohr Coulomb failure criterion.

Table 3.2 Material properties (In brackets are reported the values kept fixed during the sensitivity analysis)

Parameter	Symbol	Value
Density (Kg/m^3)	ρ	950
Porosity (-)	n'	0.4
Effective Poisson ratio (-)	v'	0.3
Effective Young modulus (kPa)	E'	20-200000 (2000)
Effective Cohesion (kPa)	c'	0
Friction angle (°)	Φ'	10-40 (25)
Dilatancy angle (°)	Ψ'	0

Porosity was set equal to 0.4 since the bulk density corresponding to the densest particle packing was 540 Kg/m^3 [32]

Release volume has been found that highly influence the results; so, as an assumption, the 2D model has a volume which equals the exact volume and it is 1.5 Kg.

During every simulation the material has some time to adjust on the base and to reach a condition of equilibrium in term of stresses. This procedure is called quasi static convergence and it is recommended by the authors of the tutorial [21] in the example of the column collapse.

The sensitivity analysis performed showed that Courant number (0.6-0.8-0.9-0.98) and Young modulus (200-2000-20000-200000) do not affect the overall behaviour of the avalanche. The numerical parameters are therefore set as follows:

Parameter	Symbol	Value
Mesh size		Unstructured triangular 3 cm
Number of particles per element		3-25 (3)
Courant number (-)	C	0.6-0.98 (0.9)

Numerical damping	δ	0.05
Bed friction angle (°)	θ	0-35 (21)
Bed contact cohesion (KPa)	c	0

Table 3.3 Numerical parameters

The size of the mesh and the number of material points affected the results; For this reason a further study on the influence of the number of material points has been carried out.
On the basis of similar works [15,16], the mesh chosen was triangular-unstructured with a size of 3cm.

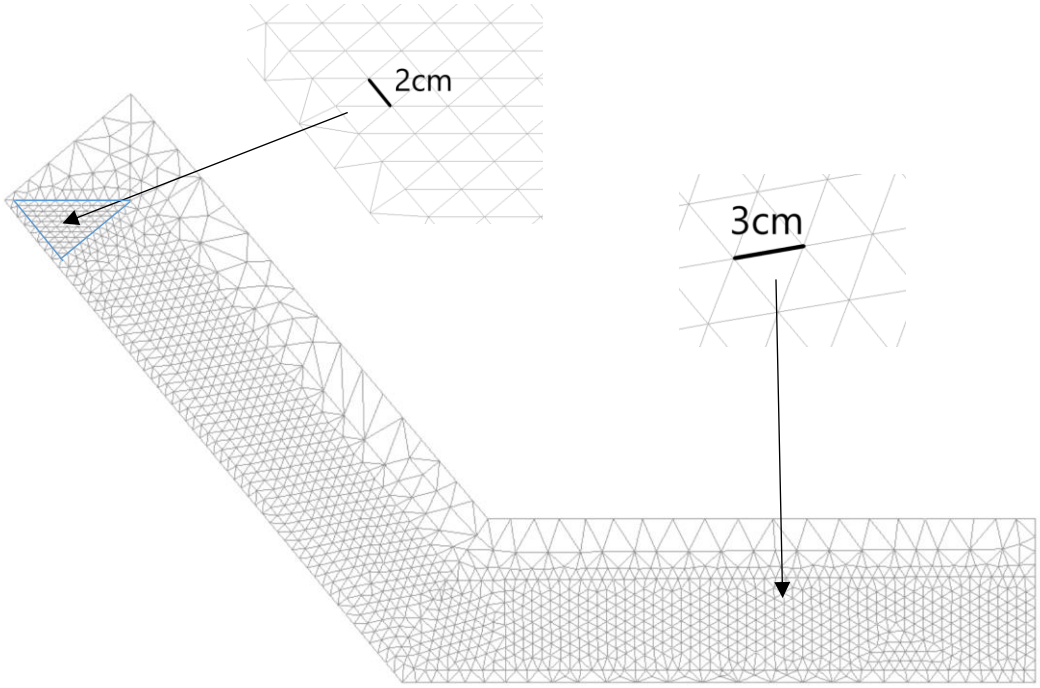

Figure 3.3 Detail of the mesh model

3.1.3 Results

The evolution of the flow is in good agreement with the experiments, especially the position of the front. The length of the deposit on the contrary is greater than the experiments because the trailing edge as soon it reaches the flat part it stops.
This trend is typical of every simulation in the sensitivity analysis.

Results are fairly insensitive to internal friction angle Φ but react critically to the values of bed friction angle θ confirming Hutter' s numerical findings [32].

For every simulation performed, the avalanche position and velocity of the front (XF, VF) and rear (XR, VR) have been recorded.

During the initial phase the data were taken qualitatively because of the difficulties in defining the shape of the avalanche. Same problem was encountered by Hutter in 1995 [32] and has been solved adopting the same approach used by Ceccato [42]. To keep the treatment as objective as possible, the problem of faster MPs was overcome by considering the average value of the first and last 20 points.

Comparing the 2 graphs of Figure 3.4 and Figure 3.5 can be highlighted the strong influence of bed friction compared to the interparticle angle. Increase in friction translates in higher energy dissipation and consequently shorter runouts.

Regarding the shape of the flow, as already found by Ceccato F.[44], decreasing the basal friction coefficient, the avalanche has a more compacted shape with higher thickness of the flow

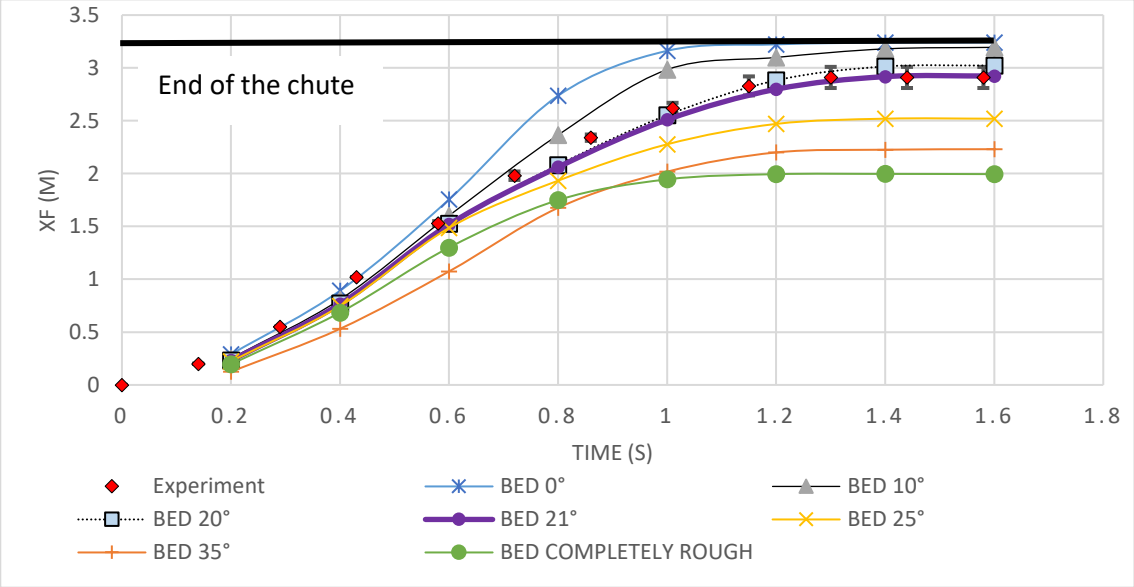

Figure 3.4 Position of the front as function of the bed friction keeping fixed the interparticle angle at 29°

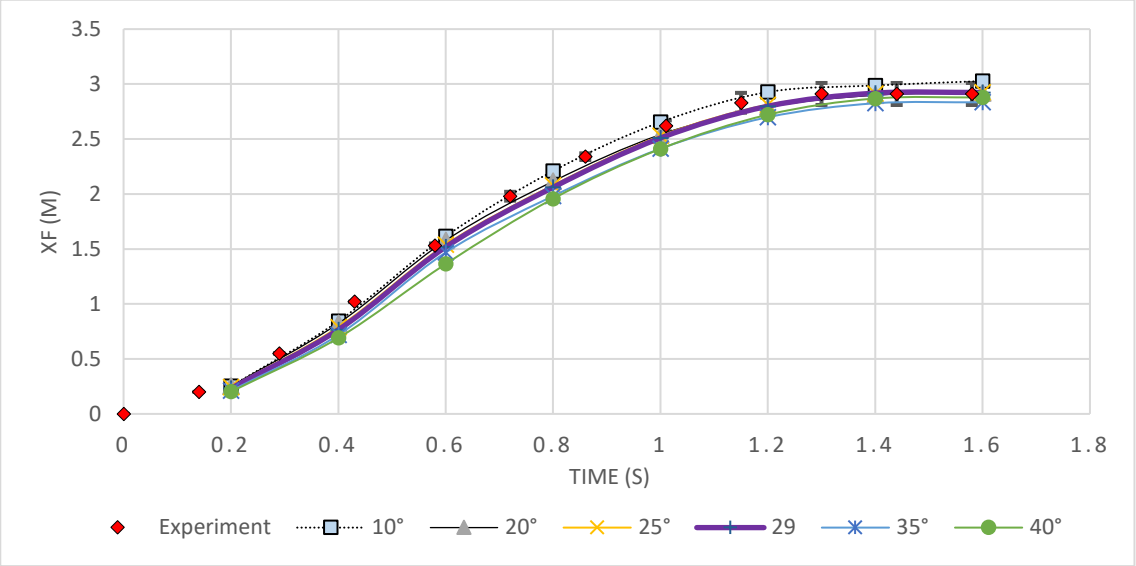

Figure 3.5 Effect of the interparticle angle keeping fixed the bed contact at 21°

The rear, as mentioned before, is influenced by the deposition of the particles ahead and rest in a range of 40 to 60 cm before the experiment evidences. Even with the extreme condition of absence of bed contact (blue line) it still shows the same trend.

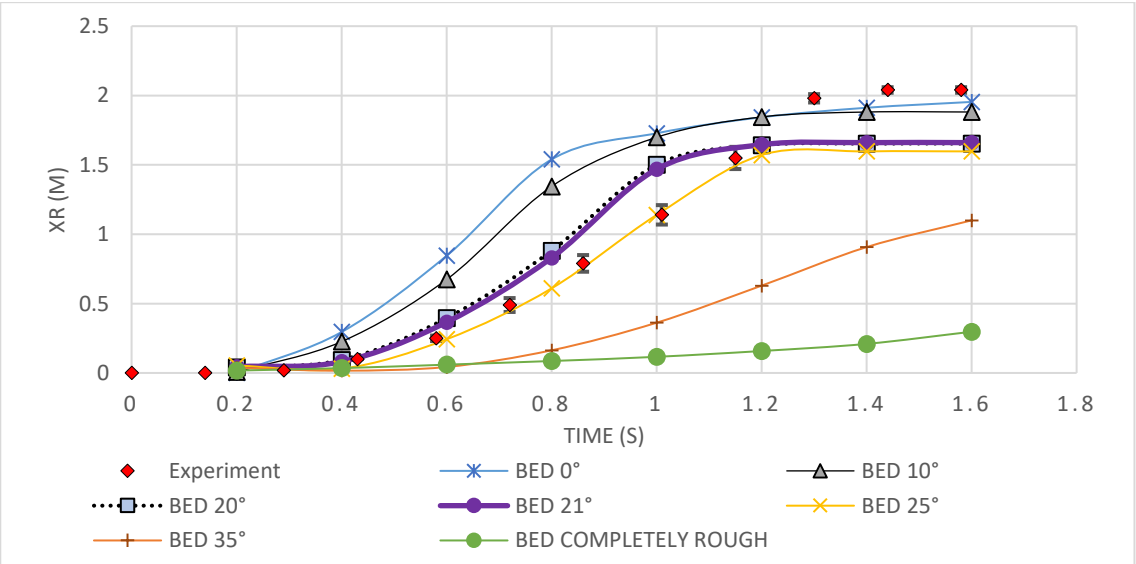

Figure 3.6 Effect of the bed friction angle on the rear position of the flow

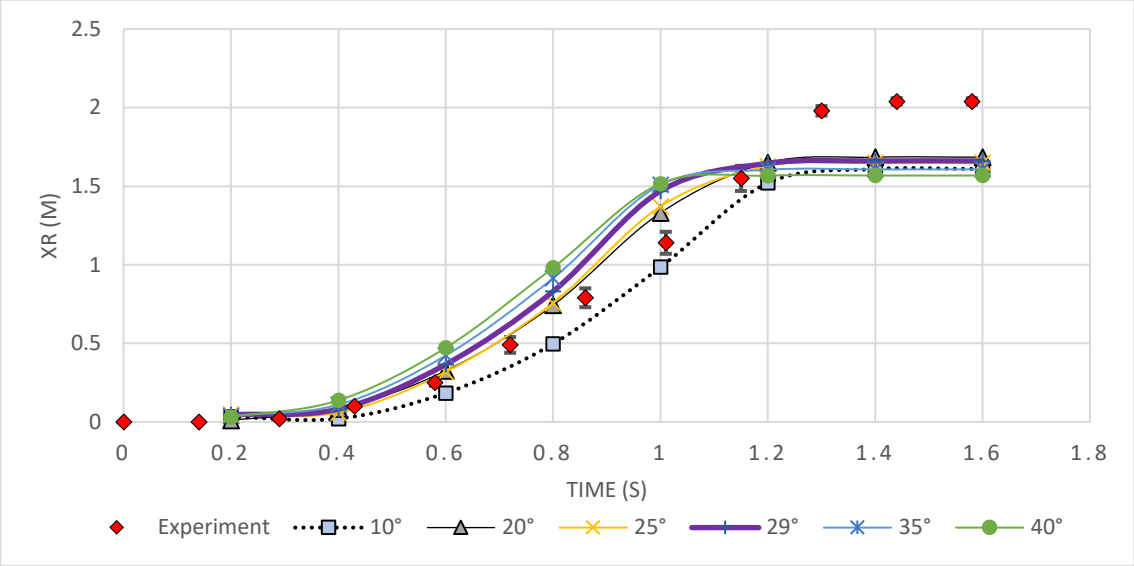

Figure 3.7 Effect of the interparticle angle on the rear position of the flow

In the graph of Figure 3.7 and the screenshot Figure 3.8 it is evident that friction angle is affecting the propagation confirming the theory. This states that the higher the friction angle is, the greater the frictional force contrasting the motion of the block will be. The shape of the avalanche highlights it: high interparticle angle corresponds to thicker and shorter granular configurations while low angles, longer and thinner flows.

In the upper graph it is worth noting the inversion of the position of the curves from the acceleration phase of the flow (t=0.4s) to the sudden braking (t=1s) and rest.

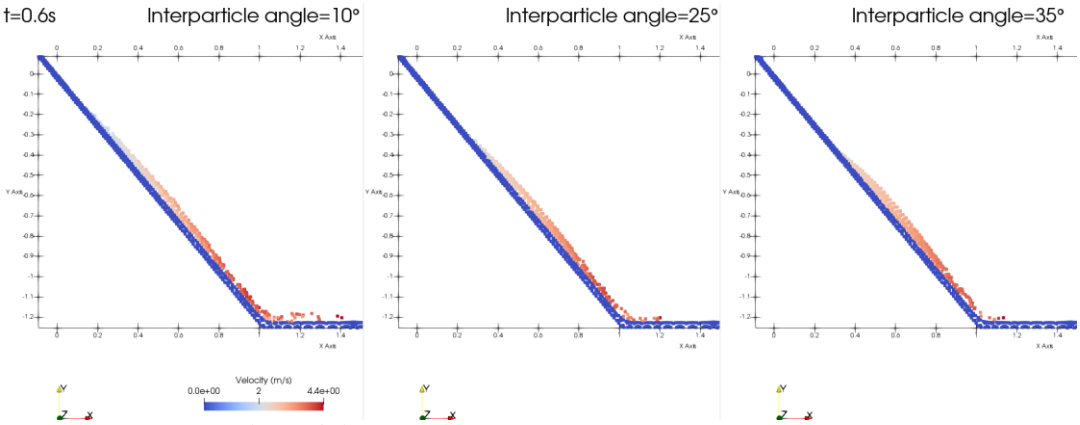

Figure 3.8 Screenshot of the simulations at instant 0.6s

Front velocity recorded at specific instant of time show that the model, in the acceleration and braking phase, slightly underestimates front velocities. Further investigations should be done in understanding the sensitivity of the velocities by changing the number of material point which are representative of the leading edge.

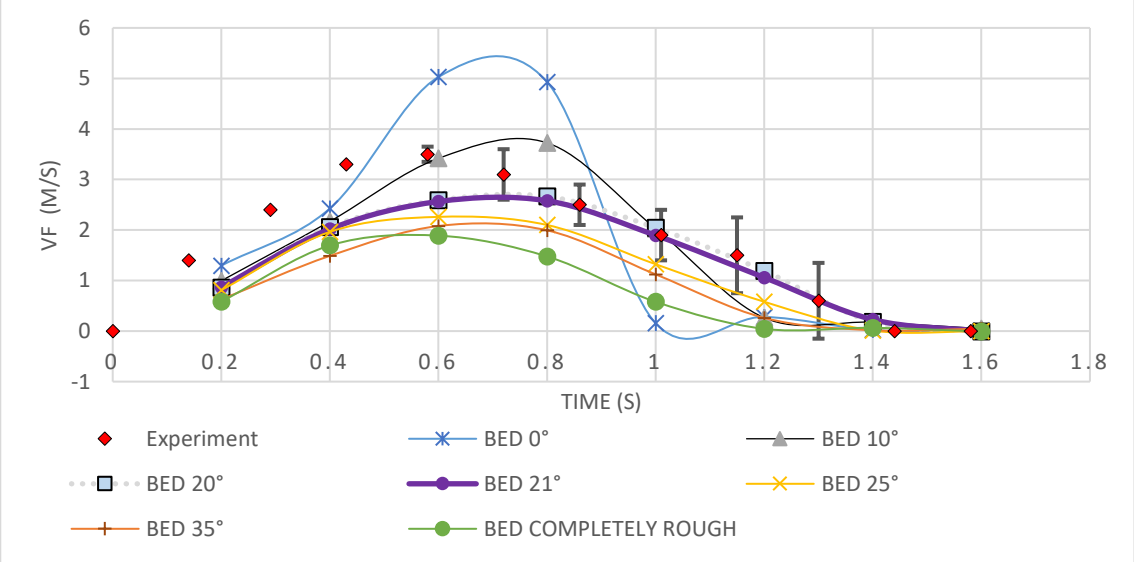

Figure 3.9 Effect of the bed friction angle on the front velocity

Trailing edge velocity does not fit again the experimental results during the deposition phase.

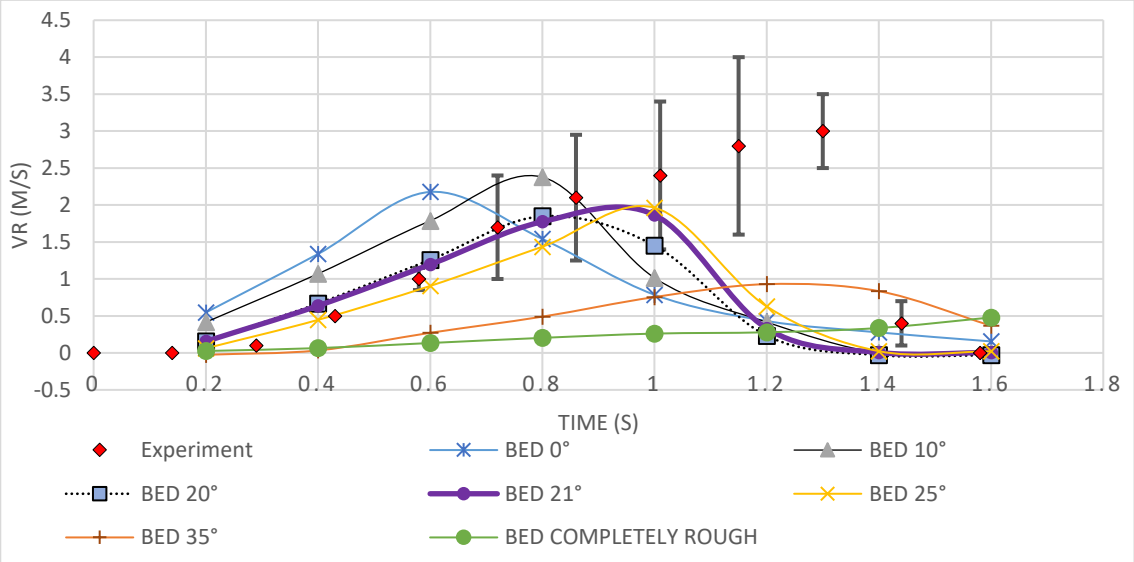

Figure 3.10 Effect of the bed friction angle on the rear velocity

For propagation problems the number of material points representing the medium has been found significant in shaping the runout of the avalanche. The results obtained modelling the material with 12 and 25 points led to a deposit that reached the end of the straight plane (Figure 3.12).
The higher the number of points the faster and stretched the flow resulted (Figure 3.12).

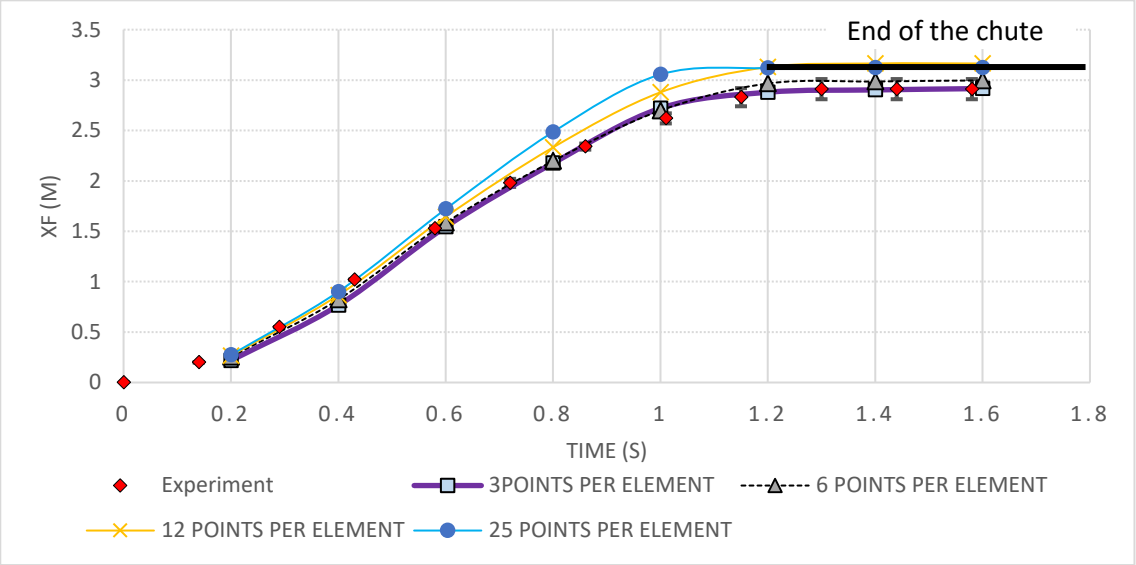

Figure 3.11 Position of the front along the trajectory considering different number of MP per element

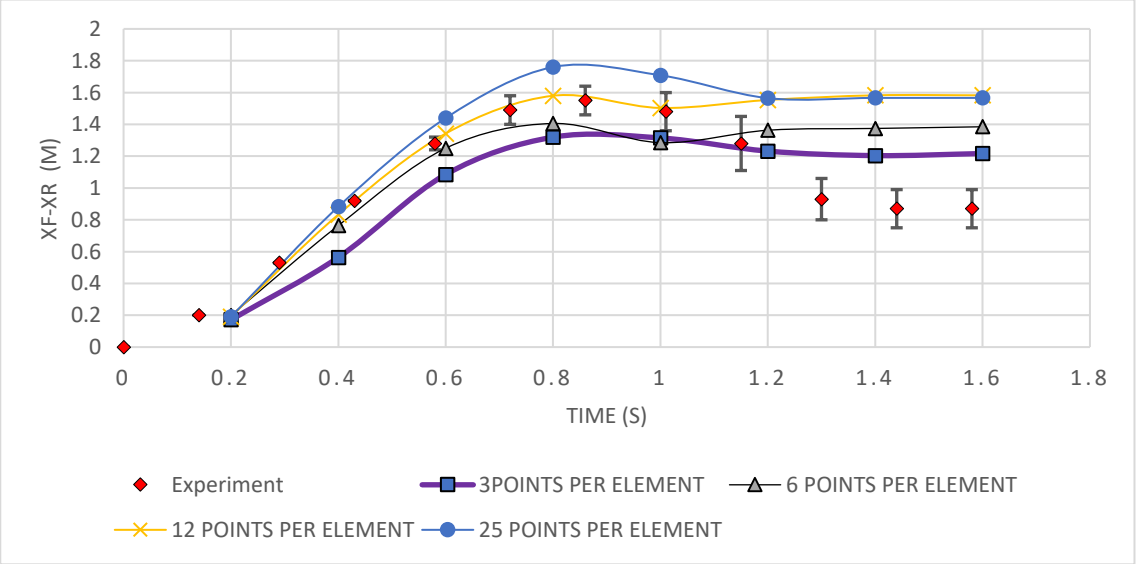

Figure 3.12 Length of the avalanche (XF-XR) by changing the number of MP's

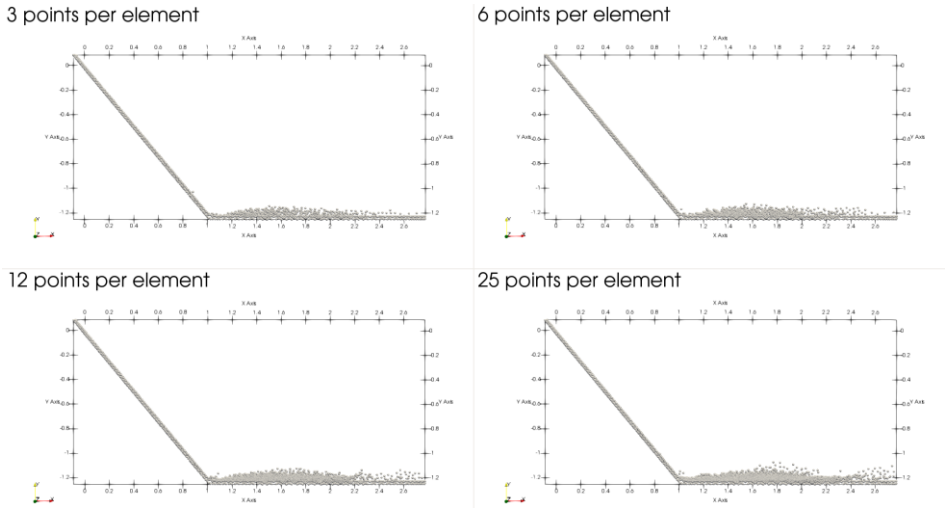

Figure 3.13 Final shape of the deposit at time 1.6s

The same simulations have been computed considering snow as a Bingham fluid. The aim of this phase is to make a comparison with Mohr Coulomb and to find the set of parameters for both models that best fit the experiments.

As previously done for the other simulations the first approach was understanding the influence of the main parameters; in the case of Bingham they are dynamic viscosity, yield threshold and bed friction.

Looking at Figure 3.14 can be noticed that, considering snow a Newtonian fluid, the order of magnitude of the viscosity which best fit the empirical results is in a range of $1.0E^{-2} \div 2.5E^{-2}$. Both values are considerably higher than the viscosity of water ($\sim 1.0E^{-6} KPa \cdot s$)

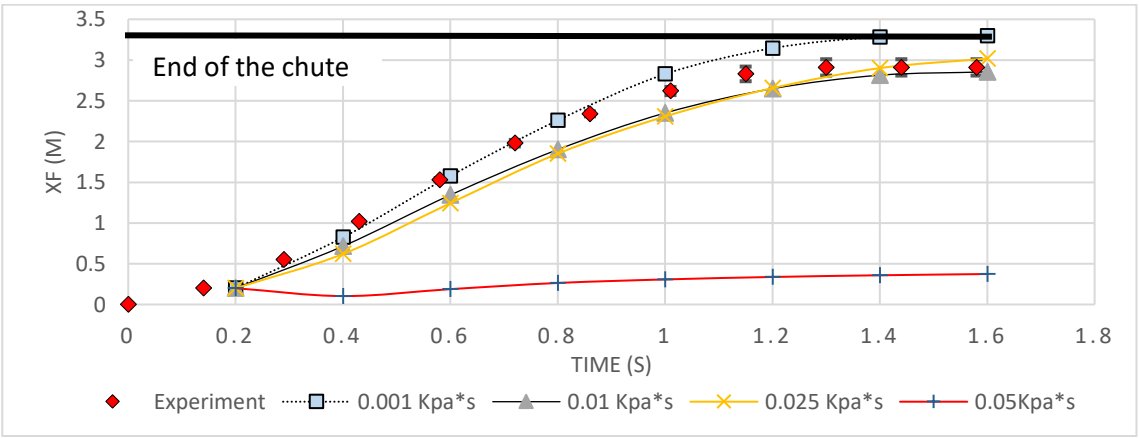

Figure 3.14 Position of the front considering a Newtonian fluid (Bingham with threshold at 0 KPa) changing the dynamic viscosity

The rear side of the avalanche, also in this case of a fluid material, has a much lower runout compared to the experiments.

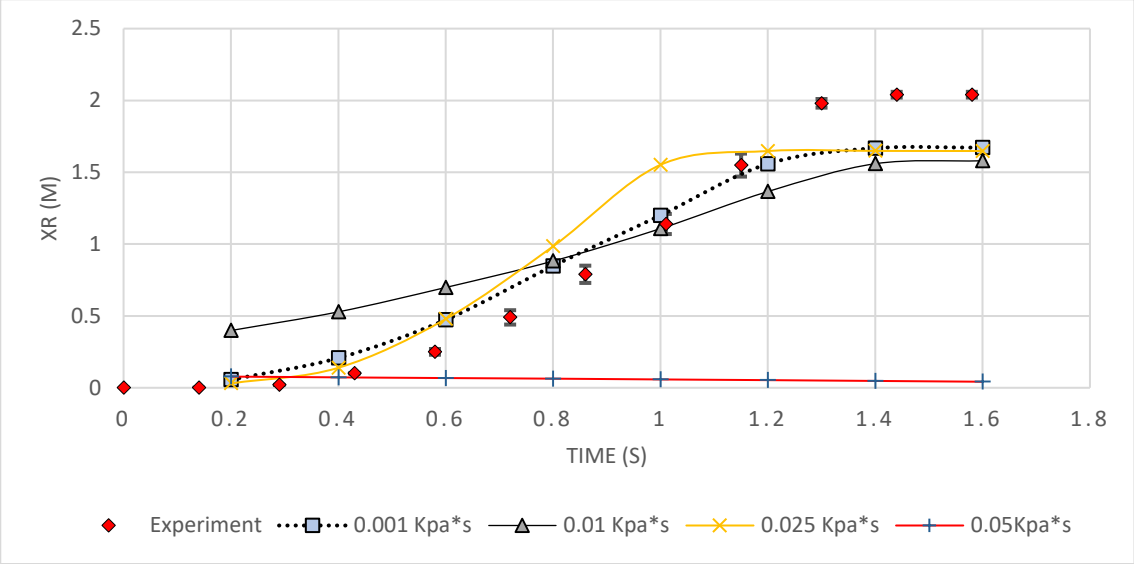

Figure 3.15 Position of the rear considering snow as a Newtonian fluid

Before the calibration of the others Bingham parameters, the bulk modulus and Young modulus have been observed having negligible effect on results.

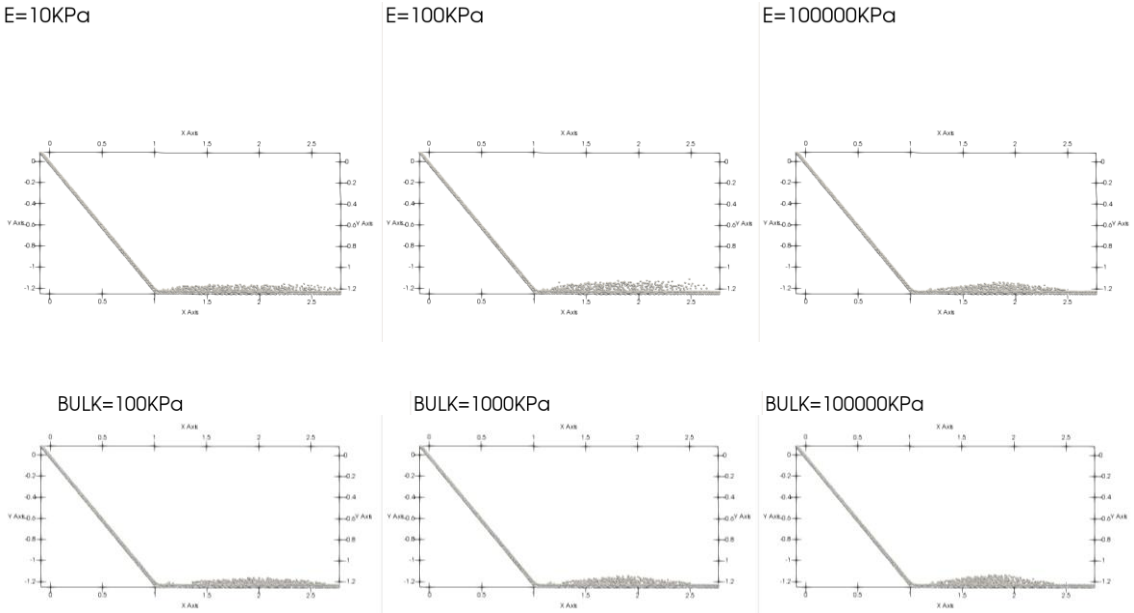

Figure 3.16 Effect of the Young and bulk modulus on the shape of the deposit

In the other sensitivity analysis snow was considered as a fluid with the same viscosity of water. The yield threshold which divides the elastic to the plastic behaviour, varied in a reasonable range ($1 \div 1E^{-2}$)

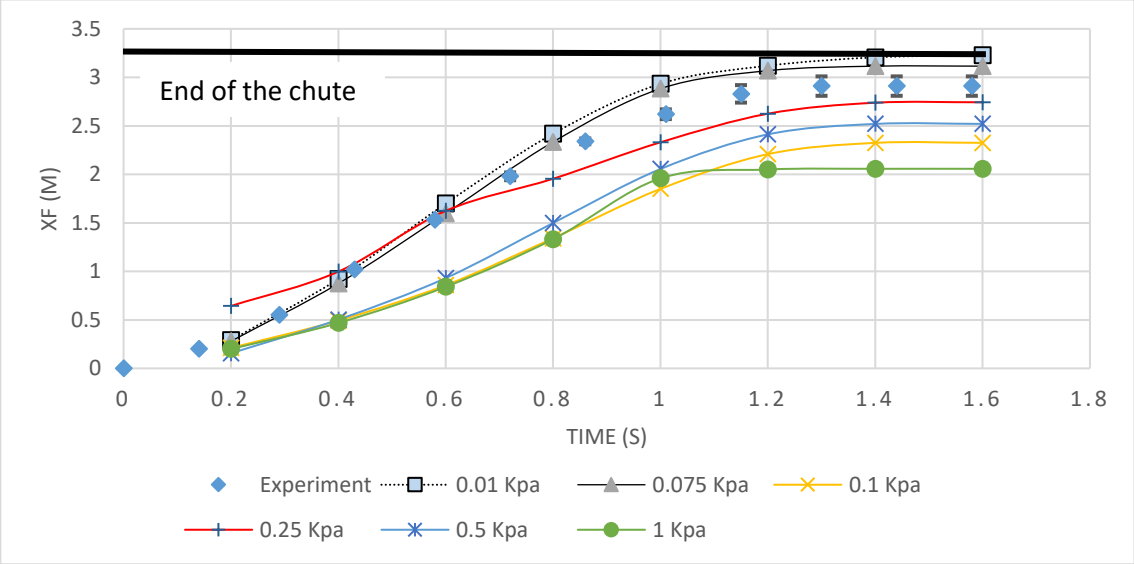

Figure 3.17 Position of the front of the avalanche varying the Bingham yield threshold

The increase in yield threshold led to a shape of the deposit which underlines the plastic deformations undergone by the material (Figure 3.18)

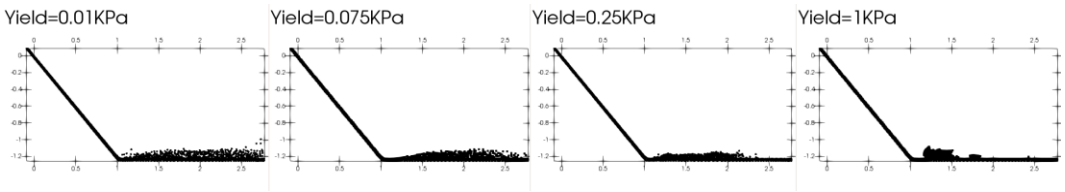

Figure 3.18 Screenshots of the material deposit at time t=16s

From the previous computations, the yield threshold was assumed to be fixed at 0.075 KPa while viscosity and bed friction have been calibrated. The combination of parameters which best fit the experiments is reported in brackets in the following table and represented in Figure 3.19.

Table 3.4 Bingham material parameters

Parameter	Symbol	Value
Density (Kg/m^3)	ρ	950
Bulk modulus (kPa)	k	100-100000 (1000)
Poisson ratio (-)	ν'	0.3
Dynamic viscosity (kPa*s)	ν	0.001-0.05 (0.001)
Bingham yield stress	τ	0.01-1 (0.075)
Elastic Young modulus (kPa)	E	10-100000 (2000)
Effective Cohesion (kPa)	c'	0
Friction angle (°)	Φ'	15
Dilatancy angle (°)	Ψ'	0

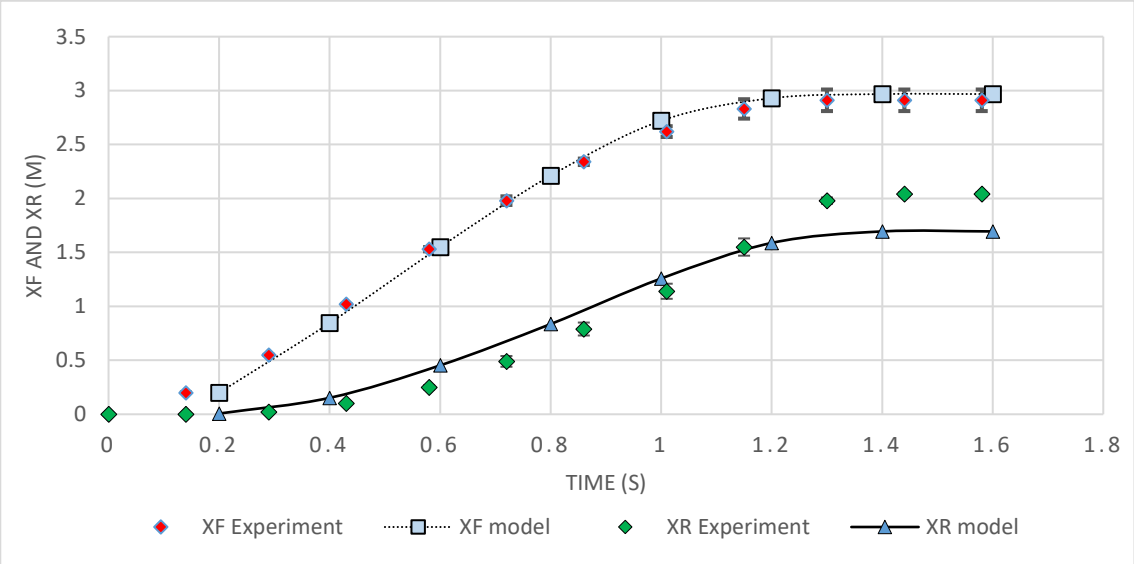

Figure 3.19 Position of the front and rear of the avalanche for the Bingham model with $\tau = 0.0075 KPa$ *and* $\nu = 0.001\ KPa \cdot s$

As already found in the Mohr Coulomb computations, the rear of the flow does not match the experiment (black line of Figure 3.19) and the increase of material points shifts forward the material (Green and yellow line of Figure 3.20)

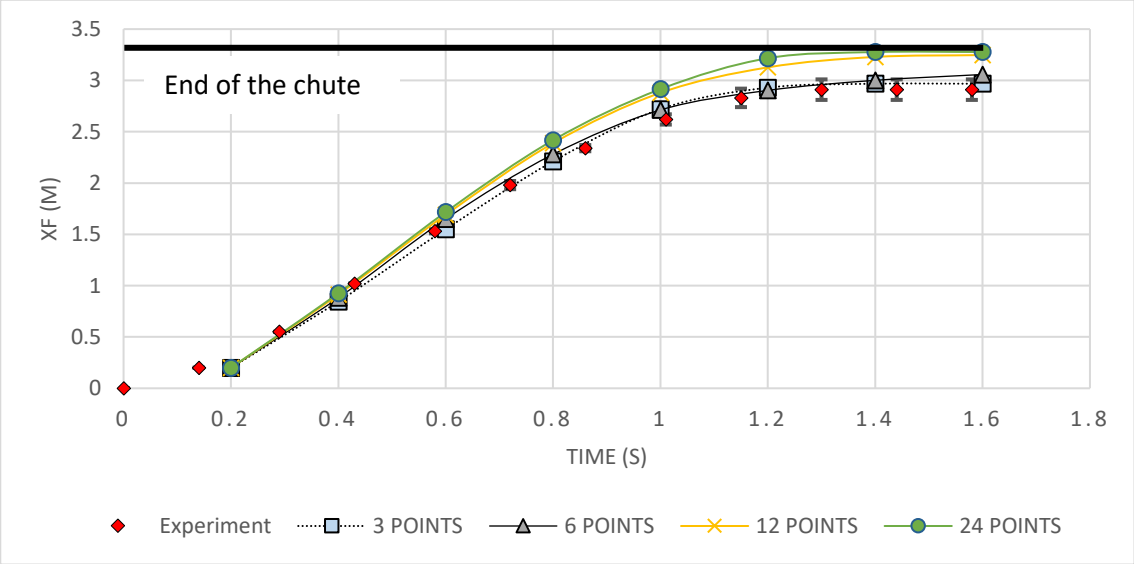

Figure 3.20 Position of the front of the avalanche for the Bingham model considering an increasing number of material points per element

3.2 Medium scale

3.2.1 Introduction of the experiment

At this step of the thesis the findings at the small scale of dry granular flow will be extended to dense snow at the medium scale. This is a fundamental link to investigate the limits of the available MPM constitutive laws in modelling the propagation. Among the type of avalanches, in the last decade, there have been studies that identified clear differences between dry and wet snow flows [18,19]. From an engineering perspective, to guarantee higher level of safety, the most critical condition for the defensive structure has been chosen and the flow was therefore considered dense.

The experiments used to calibrate the model were carried out on a snow chute in Dhundi, India [46]. The test site is located at 2800m a.s.l. and is a channel 61m long and 2m wide. The geometry of the chute follows the scheme in

Figure 3.21.

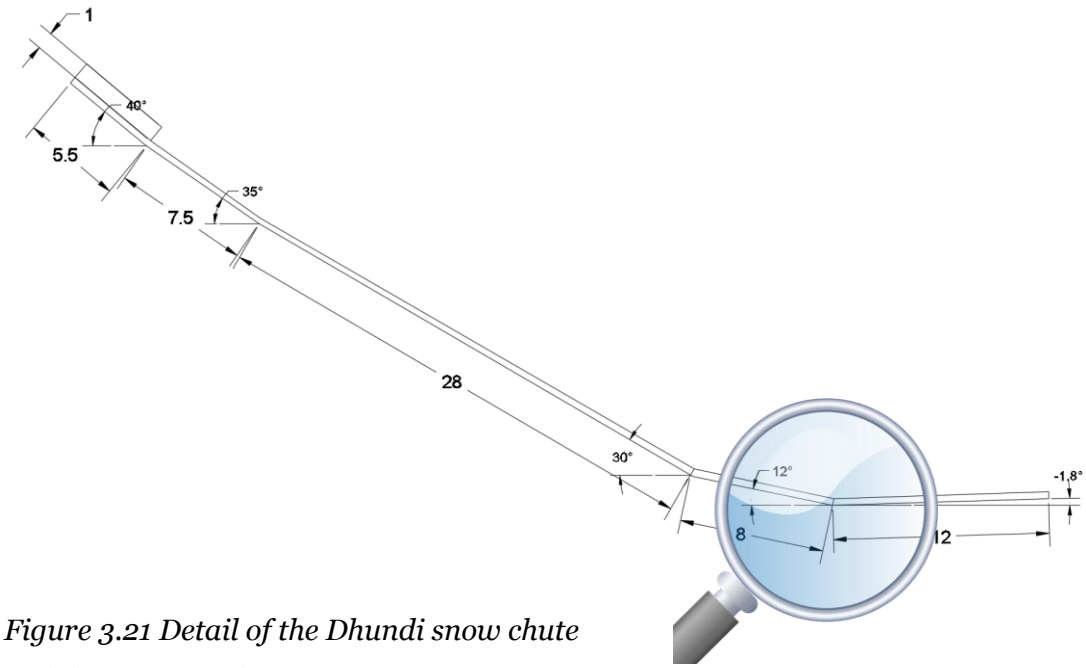

Figure 3.21 Detail of the Dhundi snow chute and focus on the deposition area.

Chute experiments are important because they have the advantage that the initial fracture conditions, geometry of the flow and properties of the flow materials are defined.

From the results of the experiment [46] the information about the velocity at a specific section could not have been matched with the run-out information [47] because the tests had different snow volumes and densities.

The decision taken was to consider the final position and shape of the deposit rather than the information of velocity at a specific point.

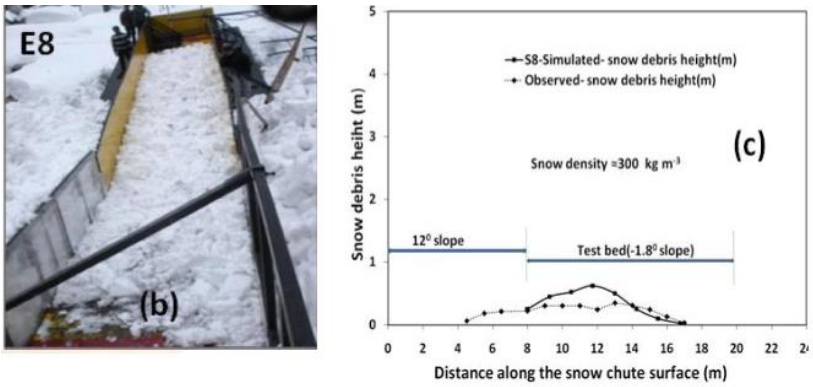

Figure 3.22 Final shape of the deposit measured experimentally and simulated with a CFD code [47]

3.2.2 MPM sensitivity analysis

The problem was modelled 2D and snow has been considered with a failure criterion of the type Mohr Coulomb.

The interparticle angle of snow in nature varies from 80° (fresh snow crystals) to 10° (highly wet) [47] but in this treating, as the flow is assumed dense, will be set at maximum 25°.

Parameter	Symbol	Value
Density (Kg/m^3)	ρ	300
Porosity (-)	n'	0
Effective Poisson ratio (-)	ν'	0.3
Effective Young modulus (kPa)	E'	200
Effective Cohesion (kPa)	c'	0
Friction angle (°)	Φ'	16-25
Dilatancy angle (°)	Ψ'	0
Number of particles per element		3
Numerical damping	δ	0.05
Bed friction angle (°)	θ	15-25 (18)
Bed contact cohesion (KPa)	c	0
Mesh size		Unstructured triangular 15 cm

Table 3.5 Mechanical and numerical parameters for the MPM model of Dhundi snow chute

At the beginning the material was modelled also as a Bingham fluid but the numerical instabilities due to the sharp discontinuity of the stress-strain relationship led to the decision to leave this approach.

Already in the simulations of the experiment of Hutter there were some small instabilities but did not affect the overall behaviour of the flow; now at a medium scale the flow has larger velocities and they become critical.

From the simulations performed with Mohr Coulomb model the deposit had a much higher thickness than the experiments. Figure 3.23 shows that the run out modelled is three times thicker than the real one.

Repose angle in a range 16°-25° does not affect a lot the results; the deposits have the same height and similar shapes.

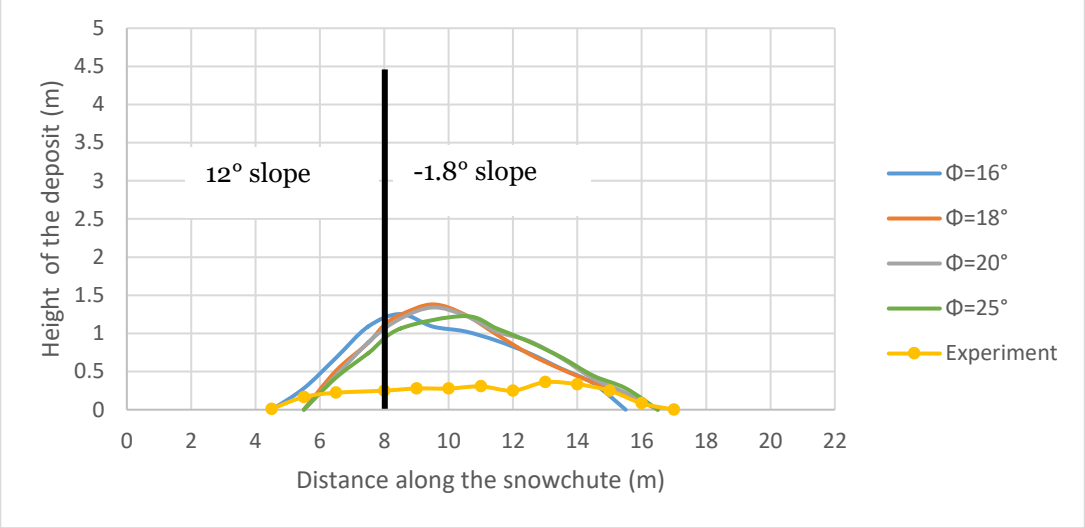

Figure 3.23 Sensitivity of the final run-out changing the angle of repose Φ and keeping fixed the contact friction θ=18°

The sensitivity analysis for the bed contact friction parameter highlights that the center of mass, as expected, is shifted forward and is more flattened for decreasing θ.

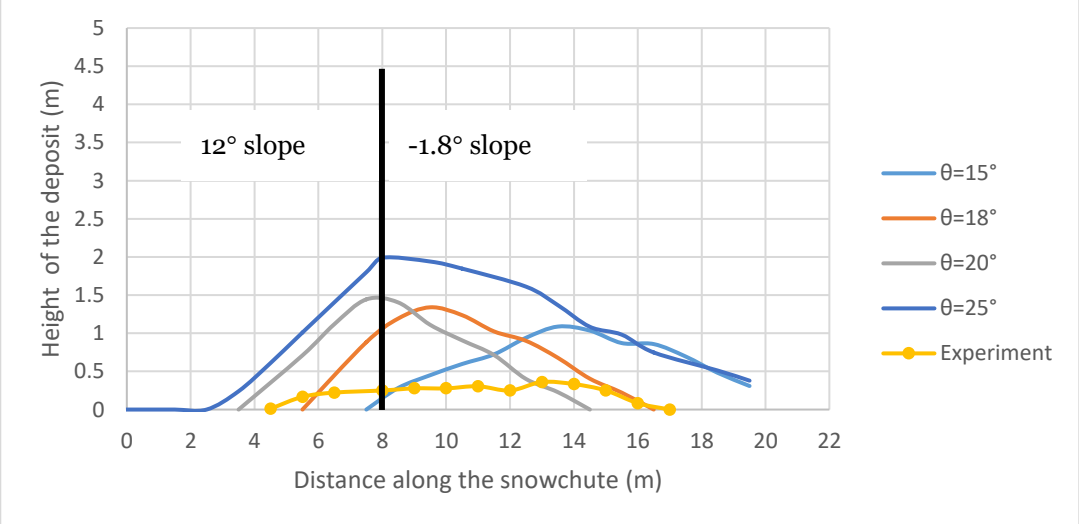

Figure 3.24 Effect of the bed contact friction keeping fixed the interparticle angle at 20°

The importance of the mesh size and number of material points is further investigated and seems that up to a size of 30cm the behaviour follows the same trend, then it begins to deviate.

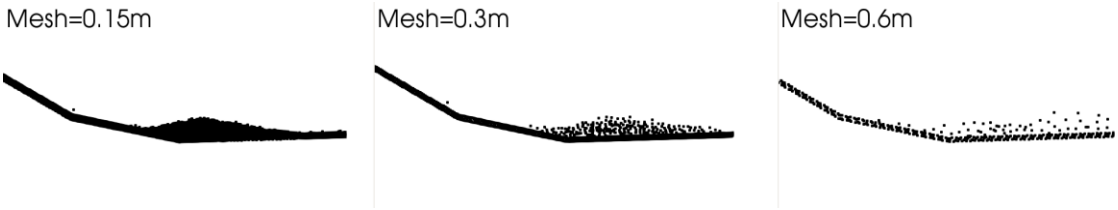

Figure 3.25 Screenshot of the final shape of the deposit for different mesh sizes

A low number of material points is not the reason of the deviation of the 60cm mesh setting. Even with 8 times the number of MP per element, another simulation showed that the deposit was completely different from the others performed. The cause must be ascribed mainly by the low numbers of elements (1-2) along the depth of the flow which leads to inaccuracies in solving the governing equations.
Nevertheless, material points influence the shape and position of the front (Figure 3.26) and confirm the findings of the previous chapter.
It must be pointed out that the comparison of the numerical output with the experiments, considered just the deposition, which is a small part with respect to the entire propagation (Figure 3.21).

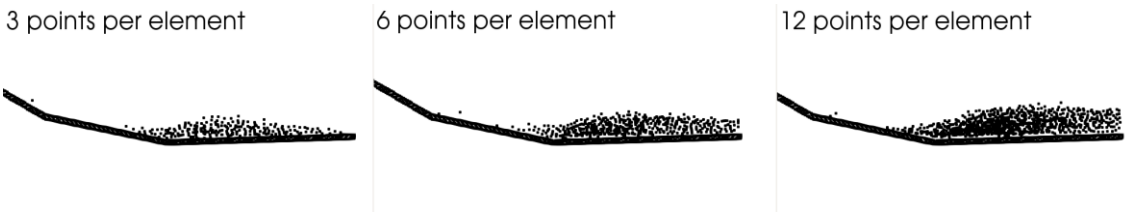

Figure 3.26 Screenshot of the final shape of the deposit by changing the number of MPs and keeping fixed the mesh at 0.3m

3.2.3 RAMMS sensitivity analysis

Dhundi experiment has been used as a reference test to investigate the accuracy of the propagation model RAMMS and to get experience about the sensitivity of its parameters.

Compared to MPM, RAMMS is a completely different model which is based on the Voellmy depth-averaged flow equations coupled with the three-dimensional digital elevation of the terrain (See chapter 2.2).

Since 2015 has been widely used in Europe for modelling dynamic of avalanches both in engineering both in research [22,23]

The main parameters governing the flow in the VS model are the sliding and turbulent friction μ and ξ. They split the total basal friction in two terms which resemble a dry Coulomb resistance and a Chezy-like friction. This decision was taken to accurately model the avalanche both in the acceleration and run-out zone.[49]

$$S_f = \mu N + \frac{\rho g u^2}{\xi} \tag{3.1}$$

$$with\ N = \rho g \cos\theta \tag{3.2}$$

RAMMS is a 3D model and therefore the results have been considered taking a section along the line passing in the middle of the chute.

The friction inputs varied in the range $0.2 \leq \mu \leq 0.4$ and $850 \leq \xi \leq 1750$ as suggested by the studies of Bartelt and Gruber performed in the Alpine area [28].

Data from the simulations showed that the sliding friction μ accounts much more than the turbulent friction ξ regarding the height of the deposit and position of the center of mass.

As in the case of the MPM model, the height of the deposit is overestimated in every scenario by RAMMS model.

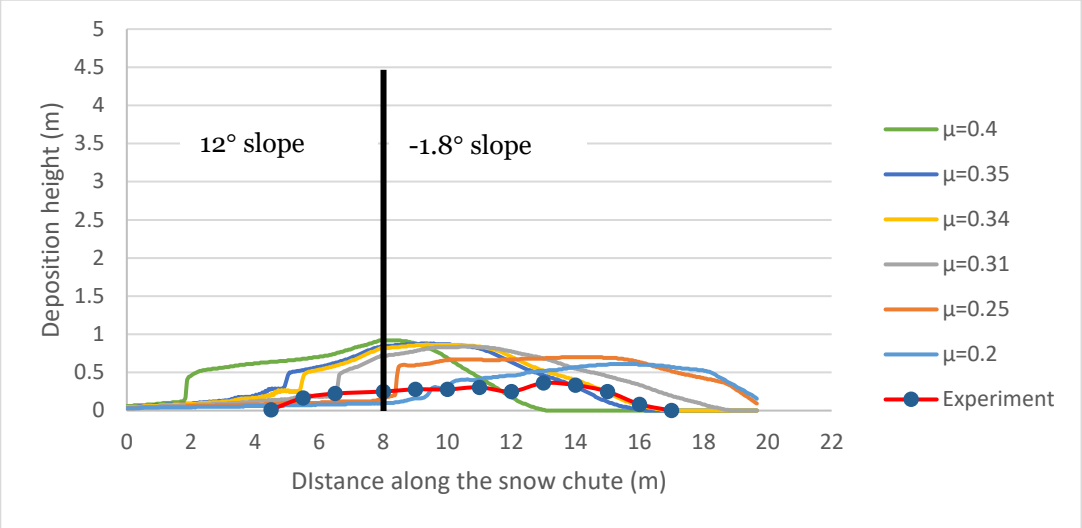

Figure 3.27 Sensitivity of the model to the parameter μ keeping constant $\xi = 1250$

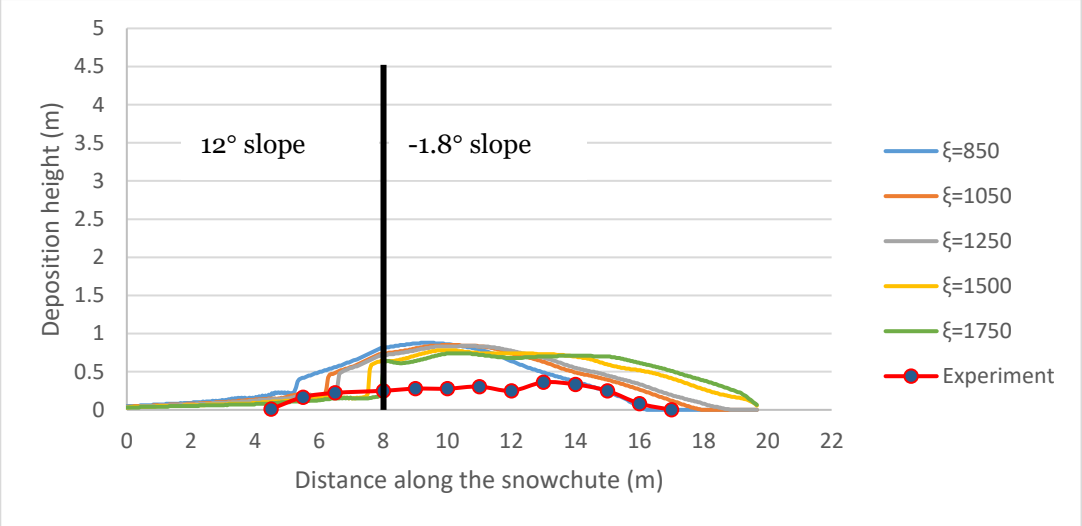

Figure 3.28 Sensitivity of the model to the parameter ξ keeping constant μ =0.3

The experience gained with the RAMMS model suggested that the main parameter which has a larger effect on both run-out distance and avalanche velocity is the avalanche volume released. This thesis has been confirmed later by the study of Buhler et Al. [48]

3.3 Large scale

In this section the findings of the previous chapter will be extended to study the propagation and impact of a real event in Val di Zocca, Masino. In history, the two mountain huts Allievi and Bonacossa, have been damaged three times; we found therefore interesting deepening the understanding of the phenomenon.

Unluckily almost no data were recorded during these events because of the winter inaccessibility of the area and the scarce interest of the Italian snow agency (AINEVA).

The problem will be analysed using a scenario-based approach to consider the variability of the release mechanism and the flowing parameters. RAMMS will be used as the reference model for the propagation and will be compared with MPM 2-D. This decision is supported by the experience gained with that model in these last twenty years in the Alpine area. Furthermore, the impact of the previous flow against a deviating wall in the proximity of the huts will be studied.

3.3.1 Val di Zocca framework

Allievi and Bonacossa are two mountain huts located in Val Masino, a lateral valley of Valtellina in the province of Sondrio. More precisely they are in the middle of the glacial amphitheatre of Val di Zocca at 2395m.

This area represents the northern boundary between Lombardy region and the Swiss Confederation.

The landscape is alpine and the slopes below Punta Rasica host a little glacier called Rasica ovest (~11.5 ha)

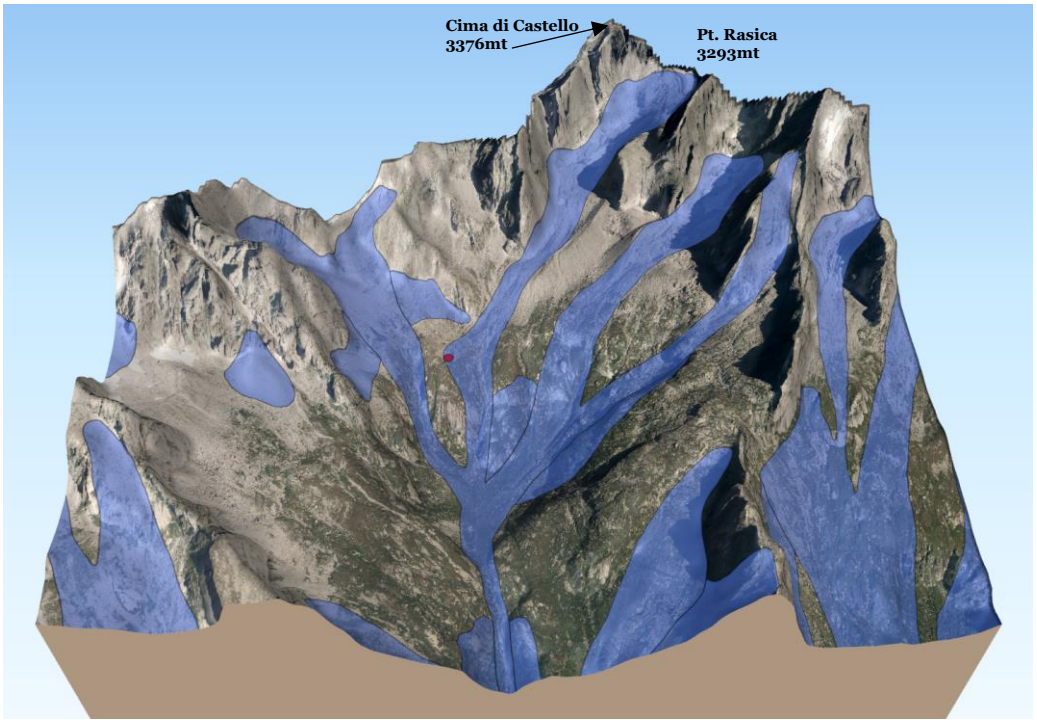

Figure 3.29 Val di Zocca 3D model, in blue the historical data of snow avalanches (Geoportale Regione Lombardia). The red pin highlihts the position of Allievi and Bonacossa huts

The buildings throughout history underwent many changes that are worth mentioning.

In 1897 the first shelter was built (Capanna Zocca) but a year later it was destroyed due to causes unknown. It was rebuilt in 1905 and dedicated to the Italian alpinist Francesco Allievi; this building in 1916 got hit by a snow avalanche and had to be reconstructed again. During the First and Second World War has been used as a military outpost because of its strategical location and closeness to the Swiss border.

In 1988 the alpinism was becoming popular and the section CAI of Milan decided to proceed with a call for applications to build, in the proximity, a new hut dedicated to the Bonacossa Brothers.[50]

The actual version, shown in Figure 3.33, dates to 2000 when the hut was damaged for the third time by an avalanche and needed some extra-maintenance works.

Figure 3.31 Version of the building in 1916

Figure 3.30 Internal damage of Bonacossa hut after the 2000 snow avalanche event

Figure 3.32 External damage (December 2000)

Figure 3.33 Current version of Allievi and Bonacossa hut

3.3.2 Propagation analysis

The RAMMS model has been initialized with a digital terrain model of 5x5m resolution (ed. 2015), the snow density was fixed at 300 Kg/m^3 and the standard flow parameters ranged from a return period T of 30 to 300 years [28].

Release flow height was assumed to be lower than 1m as suggested in several studies of dense snow avalanches ([2], [29], [48]).

The simulations have been calculated considering a set of possible release scenarios as reported in

Table 3.6.

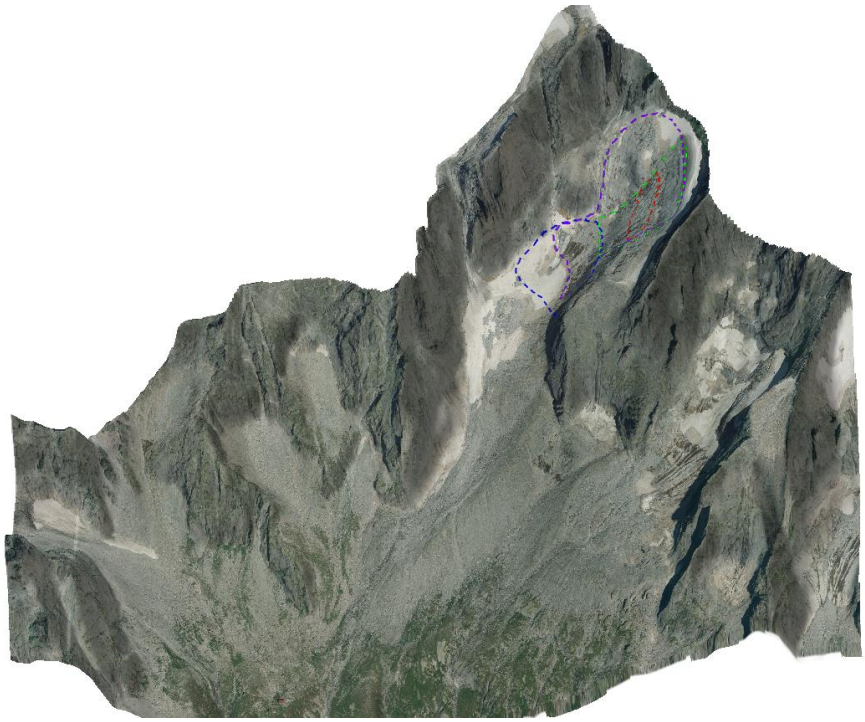

Scenario	Area	Slab height (m)	Release volume (m^3)
A	RED	0.5	8416
B	RED	1	16832
C	GREEN	0.5	35263
D	GREEN	1	70526
E	BLU	0.5	33665
F	BLU	1	67331
G	PURPLE	0.5	72033
H	PURPLE	1	144067

Table 3.6 RAMMS scenarios considering different release volumes

As already mentioned in chapter 3.2.3, the main parameter governing the flow propagation is the release volume. During the initial stage the volumes have been chosen considering the slopes with maximum inclination (SCENARIOS from A to D) but the results showed that those areas were too small, and the flow did not reach the huts even in the worst case of T=300

years.

In the second stage the release areas were enlarged, and both the scenarios G and H partially or severely damaged the lodges (μ and ξ for T=300 years) The choice of the most likelihood release area is therefore a critical step of the modelling process; usually this task is left to mountain expert who base their decision on similar events because a reliable release model has not yet been developed [51]

Flowing parameters have been assumed to be fixed with a return period of T=300 years in order to consider the worst possible scenario (Figure 3.34). They are automatically computed evaluating the curvature from the digital model of the terrain and identifying the type of slope (open, channelled, gully or flat).

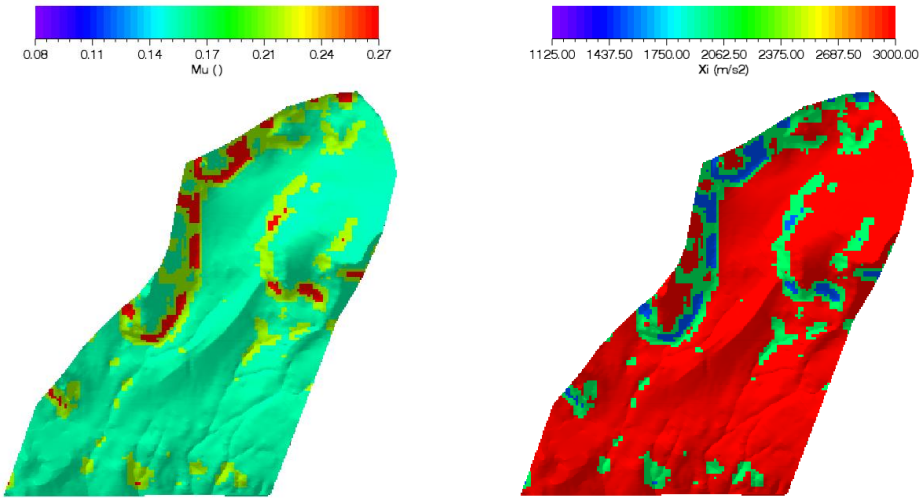

Figure 3.34 Frictional μ and ξ parameters for T=300 years

This assumption, however, does not influence a lot the outcome because the simulations with parameters T=30 and T=100 years have almost the same propagation with a mismatch of just few cm of flow height and maximum 2-3 m/s of velocity in the proximity of the huts.

Very difficult has been the evaluation of the runout distance because of the gully and the steep change of slope just below the two huts. The flow, therefore, cannot deposit and continues its path towards the valley.

The simulations showed that the flow rapidly accelerates in the first open slope, reaching velocities up to 45 m/s.

At 20s after the release, the avalanche feels the presence of the counter S-E slope and begins to direct into the wide channel.

A big portion of the volume, at 40s overcomes the natural barrier and spread down the open slope at the right of the channel that leads to the mountain lodges. The rest of the flow undergoes a steep right turn that dissipates a lot the velocity and channelized in a gully. Approximately at 70s, the rather small channel cannot drain all the flow and a small portion of it exceeds the edges and flows down the slope just above the two huts. This last stream completely flows over Allievi building and partially covers Bonacossa one.

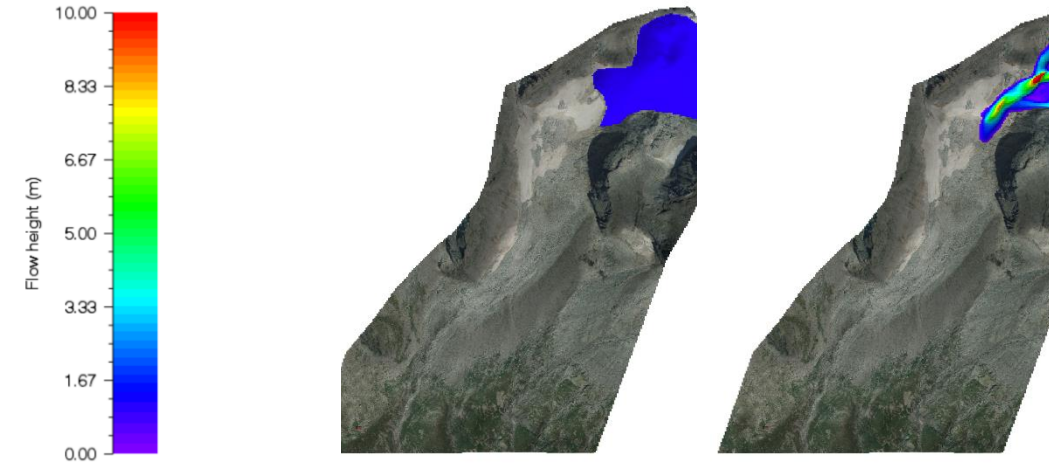

t=0 s t=10s

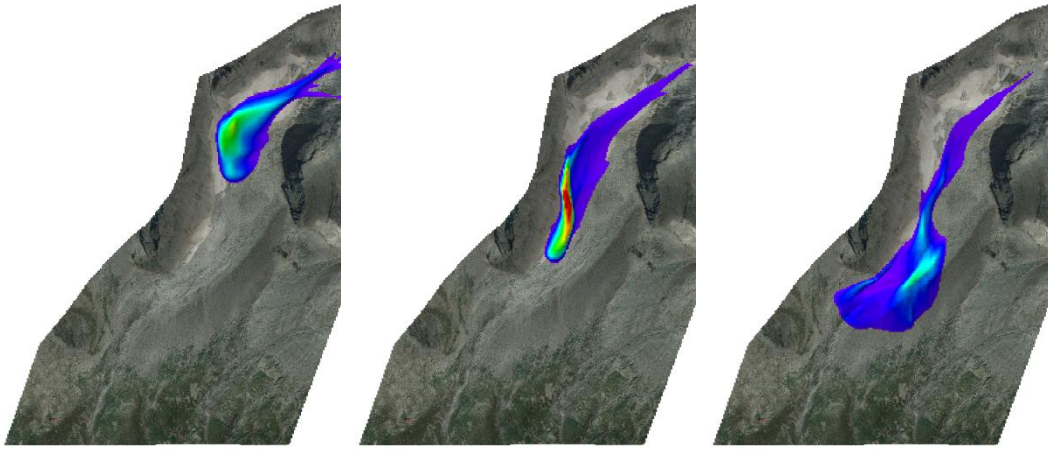

t=20 s t=30s t=40s

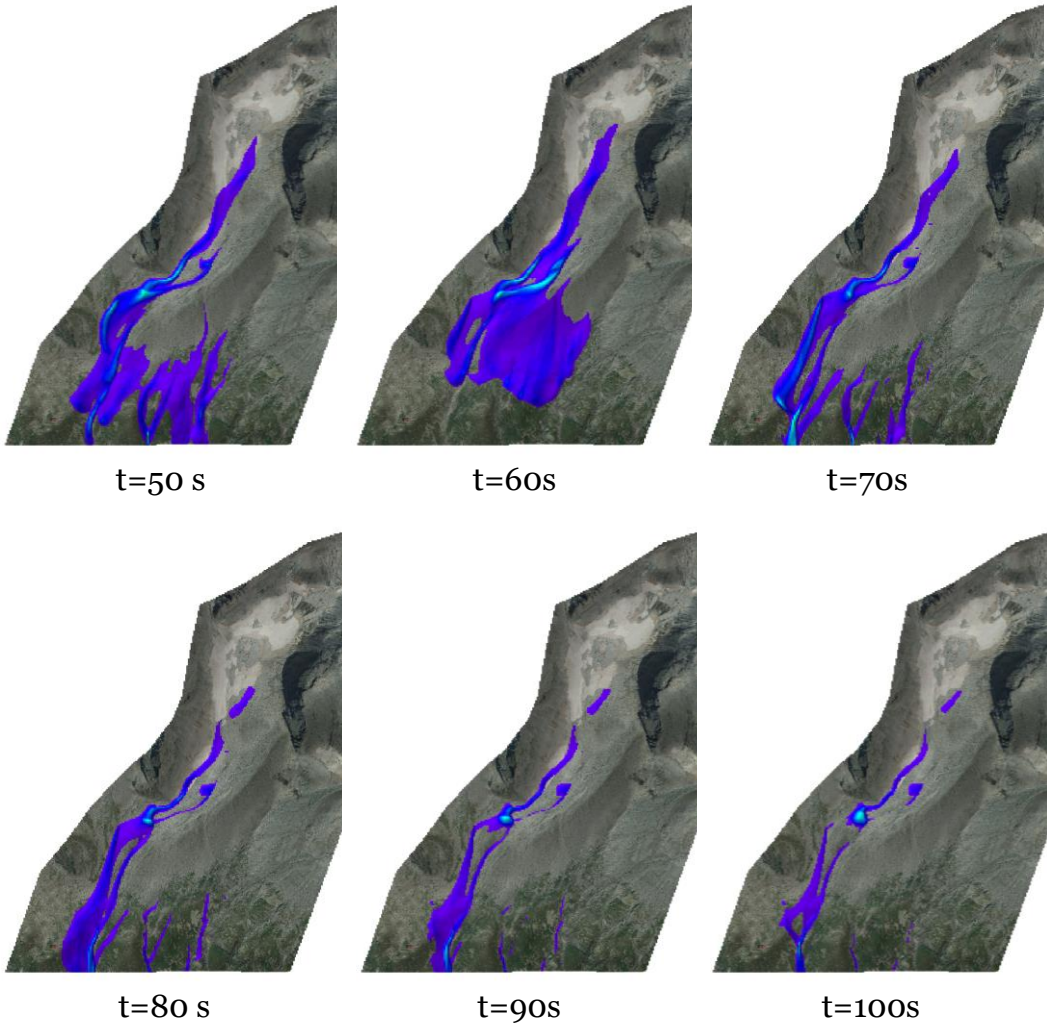

Figure 3.35 Screenshots of the scenario H at different instants of time

Previous simulations showed the propagation in space, but the results needed to be extracted along a profile otherwise could not be compared with the 2D MPM model. The profile chosen followed the gradient of the maximum velocity in the first part of the slope and then matched the trajectory towards the huts (
Figure 3.36)

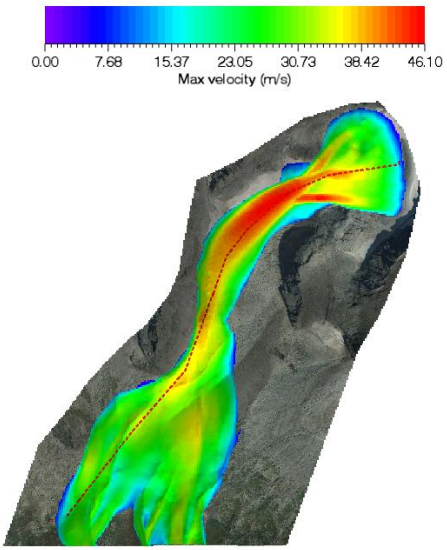

Figure 3.36 Cross section profile used as topographic input for the MPM simulation

Considering the problem 2D plane strains turned out to be a heavy assumption but was the only choice available. Unluckily the computational cost and the instabilities of Anura code did not allow to model such a large-scale problem 3D.

Although the propagation differs considerably from one method to the other because of the strong influence of the geometry and the different constitutive behaviour, the MPM maximum velocities matched quite well the RAMMS results.

The material point method has been calibrated considering firstly the friction angle which corresponded to the same propagation time, from the release to the impact, evaluated with RAMMS. Secondly, the interparticle angle ranged from 10 to 20° in order to investigate the differences and to select the simulation which best fit the RAMMS findings.

In the following table are reported the numerical and mechanical parameters employed in MPM simulations:

Parameter	Symbol	Value
Density (Kg/m^3)	ρ	300
Porosity (-)	n’	0

Effective Poisson ratio (-)	ν'	0.3
Effective Young modulus (kPa)	E'	200
Effective Cohesion (kPa)	c'	0
Friction angle (°)	Φ'	10-20 (12)
Dilatancy angle (°)	Ψ'	0
Number of particles per element		3
Numerical damping	δ	0.05
Bed friction angle (°)	θ	5-25 (20)
Bed contact cohesion (KPa)	c	0
Mesh size		Unstructured triangular 1 m

Table 3.7 Numerical and mechanical parameters of MPM real scale propagation

The best fitting simulation to the RAMMS results has been that one with an interparticle angle of 12° and a contact friction of 20°. The front of the avalanche, with this last setup, reached Allievi hut in 69s compared to 72s of the other model. The results were very sensitive to small variations of interparticle angle and, for instance, with just 1° increase the flow could not reach the lodges.

In Figure 3.37 are reported the MPM results extracted manually each 50 m together with the RAMMS ones.

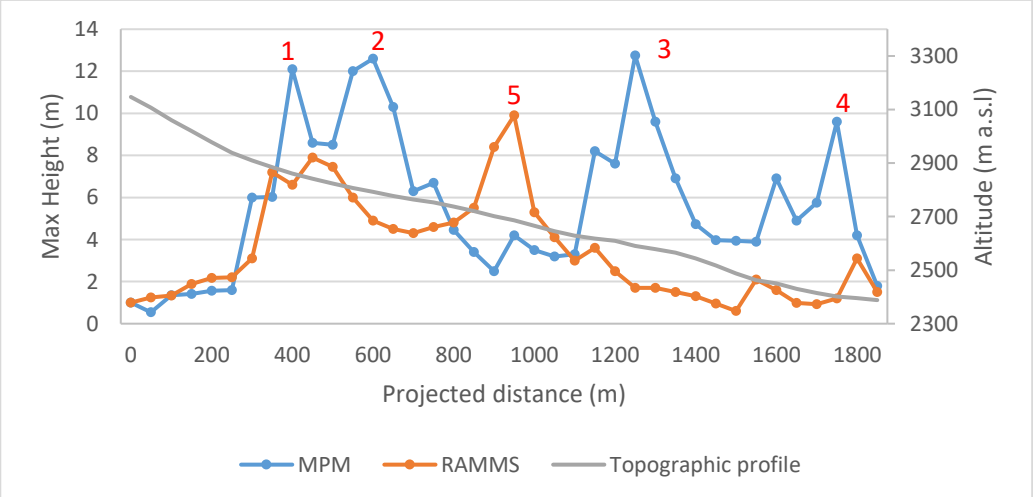

Figure 3.37 Maximum flow height registered along the section profile over the whole simulation time

MPM shows four main peaks of flow height (400,600,1300 and 1750m); the first two are related to the sharp change of slope of the valley present at approximately 300m of distance. Here the flow suddenly brakes, and the front is overtaken by the rear faster flow. The avalanche changes therefore its shape and becomes thicker. The behaviour is confirmed by the velocity pattern of Figure 3.38 that highlights an evident decrease of speed from 400 to 650m.
Third and fourth peaks follow the same reasoning and are effects of the change of slope at 1200 and 1700 m.

The evident mismatch of the height magnitude is mainly due to the 2D impossibility of lateral spread and by the differences in the constitutive laws. RAMMS model shows another glaring peak at 900m (number 5 in Figure 3.38)

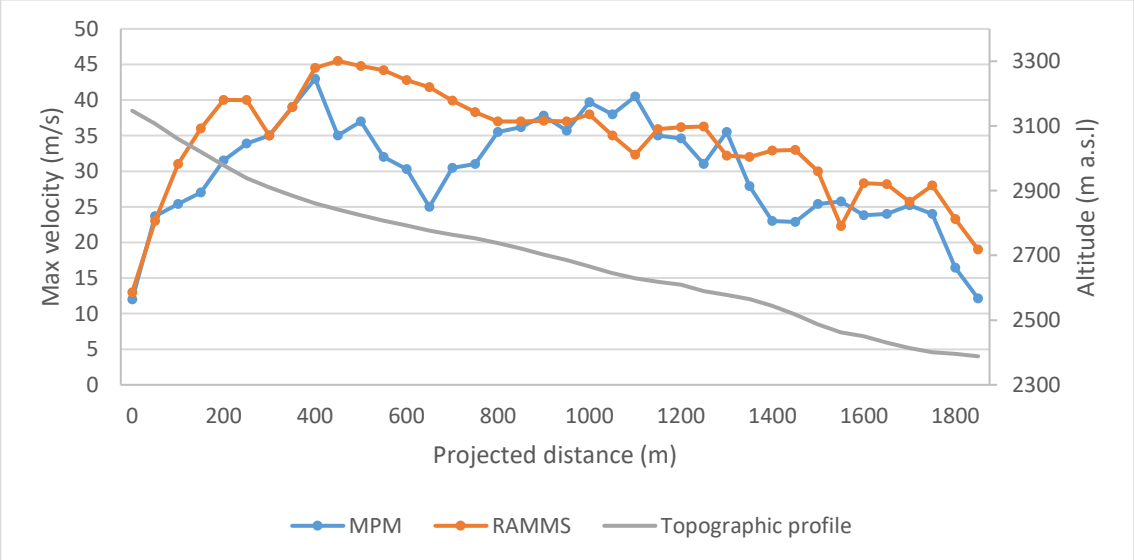

Figure 3.38 Maximum flow velocity registered along the section profile over the whole simulation time

3.3.3 Impact analysis

This subchapter investigates the impact of the snow avalanche against a barrier placed 5 m ahead of Allievi hut. Among the possible mitigation measures, after a quick cost-benefit analysis it was chosen the option to directly protect the building through a wall. The remoteness of the area leads to high working cost that cannot be justified by such a low exposure. Actually, during the winter season, the lodges are closed and usually no people visit those mountain slopes. Furthermore, as found in the propagation analysis, the huts are not on the direct track of the flow but are hit by a secondary flow that climbs over the edge of the channel. These considerations suggest therefore a solution which is relatively simple and cheap to be implemented.

Hexagonal woven mesh gabion boxes are employed for slope stability applications, but their versatility fits well also for such a marginal impact. In order to design this protecting wall, the evaluation of impact actions is of fundamental importance.

In this treating the results of the propagation with RAMMS model (Scenario H) will be used as boundary condition to study the impact with the MPM approach. The following description is intended to represent only the dynamic of the dense core, which is the predominant factor if compared to the fluidised and powder parts. The analysis does not consider any entertainment effects of boulders or tree trunks within the flow.

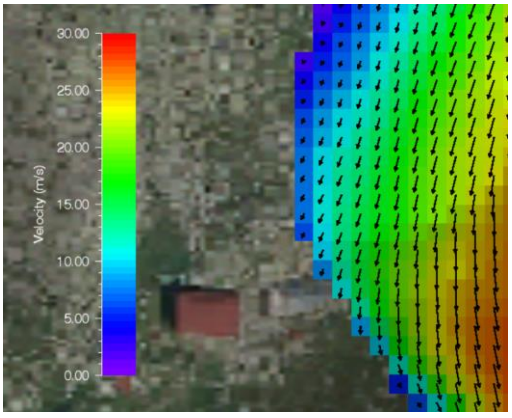

Figure 3.39 Flow velocity at t=74s

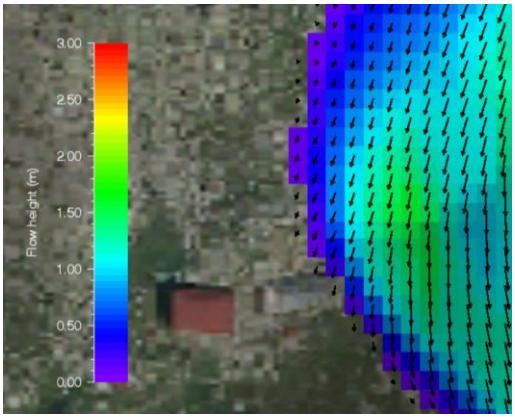

Figure 3.40 Flow height at t=74s

Impact velocity of the flow, has been chosen on the safe side, fixed at 15 m/s (Figure 3.39).

Here below are presented the numerical and mechanical parameters used to model the snow and wall materials.

The gabions were modelled with the simplest law of the type linear elastic. Numerical parameters have been set considering the findings on granular flow impact of Ceccato et Al,2018 [43] .

Parameter	Symbol	Snow	Wall
Material model		MOHR-COULOMB	LINEAR-ELASTIC
Density (Kg/m^3)	ρ	300	2013
Porosity (-)	n'	0.4	0.3
Effective Poisson ratio (-)	v'	0.3	0.3
Effective Young modulus (kPa)	E'	10-10000	1-1000
Effective Cohesion (kPa)	c'	0	-
Friction angle (°)	Φ'	20	-
Dilatancy angle (°)	Ψ'	0	-
Number of particles per element		3	3
Numerical damping	δ	0.05	0.05
Bed friction angle (°)	θ	5	5
Bed contact cohesion (KPa)	c	0	0
Mesh size		Unstructured triangular 15-60 cm	Unstructured triangular 15-60 cm

Table 3.8 Material parameters employed in the impact simulation

Mechanical parameters of the woven mesh gabion boxes have been deducted from the price list.[52]

Knowing that a 200x100x100 cm module weights 3100 Kg and assuming a porosity of 0.4, the density has been calculated as follows:

$$V_s = \frac{V}{1+n} = \frac{2}{1.3} = 1.54\ m^3 \tag{3.3}$$

$$\rho = \frac{m}{V_s} = 2013 Kg/m^3 \tag{3.4}$$

Results of the simulations showed that the phenomenon is highly influenced by the dynamic of such a low-density fluid. The low inclination of the front (~8°) is the reason of low impact values compared to the national guidelines for snow load. Impact geometry has already been found by Calvetti et Al. [53] being the leading factor in the different deformation and energy dissipation processes.

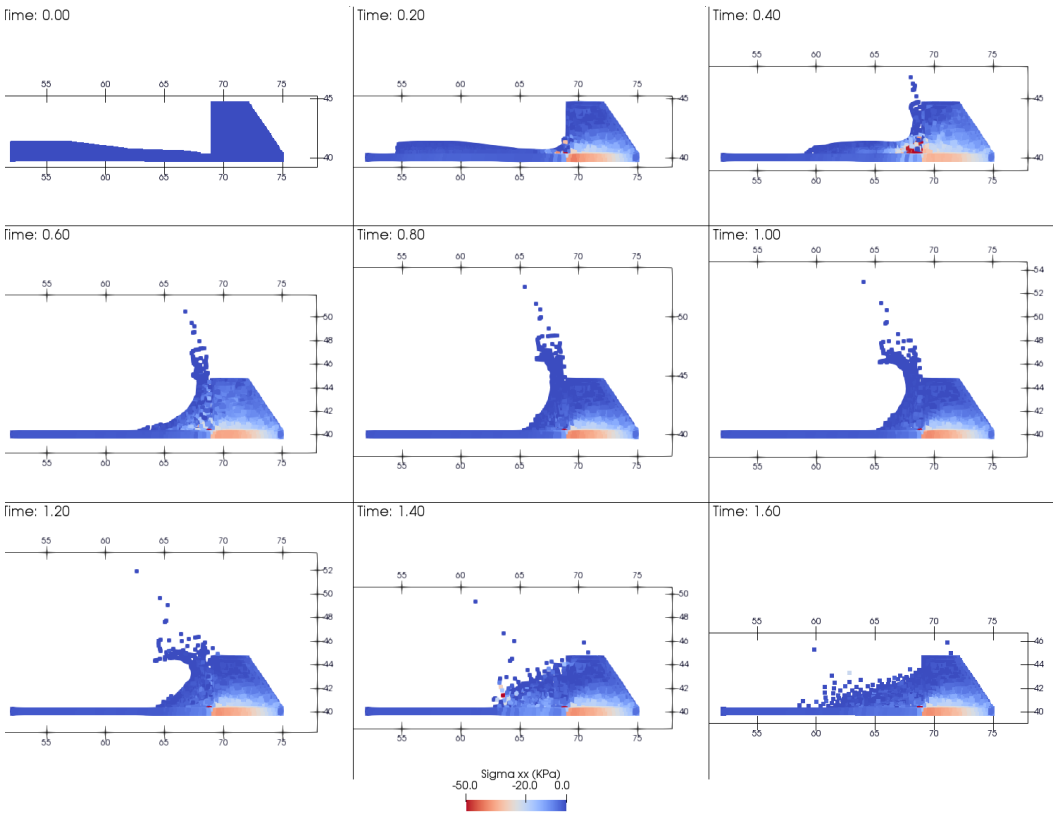

Figure 3.41 Stress evolution in time considering the flowing shape and velocity evaluated in the propagation analysis

In Figure 3.41 must be pointed out that the high stresses at the basement of the wall are due to the assumption of a wall fixed to the ground.

If the findings are compared with the granular flow impact performed by Ceccato et Al. [43], the high fluctuations of impact forces on the wall are very evident.

Figure 3.42 Effect of snow Young Modulus on the impact force highlights it, and this trend of unphysical oscillations is confirmed by many works [42], [44],[54].

The actual method uses piecewise-linear basis functions to map data from the MP to the background mesh and vice versa. The discontinuities in the gradients of such functions leads to these inaccuracies. A solution of the problem is under development: Steffen and Tielen [54] have already demonstrated that the use of higher order B-spline basis function guarantees the continuity of the gradients and smooths the solution.

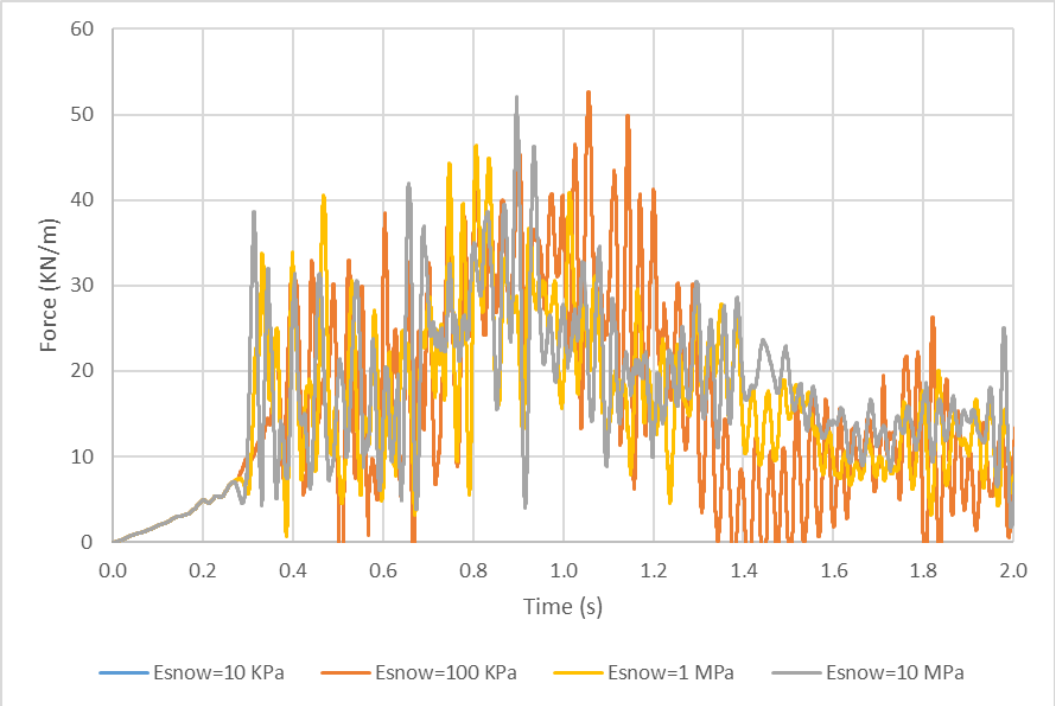

Figure 3.42 Effect of snow Young Modulus on the impact force considering a front inclination of 8°

MPM simulations showed that the snow Young modulus does not significantly affect the results for values higher than 100KPa. Maximum peaks of impact forces are in the range of 45-55 KN/m

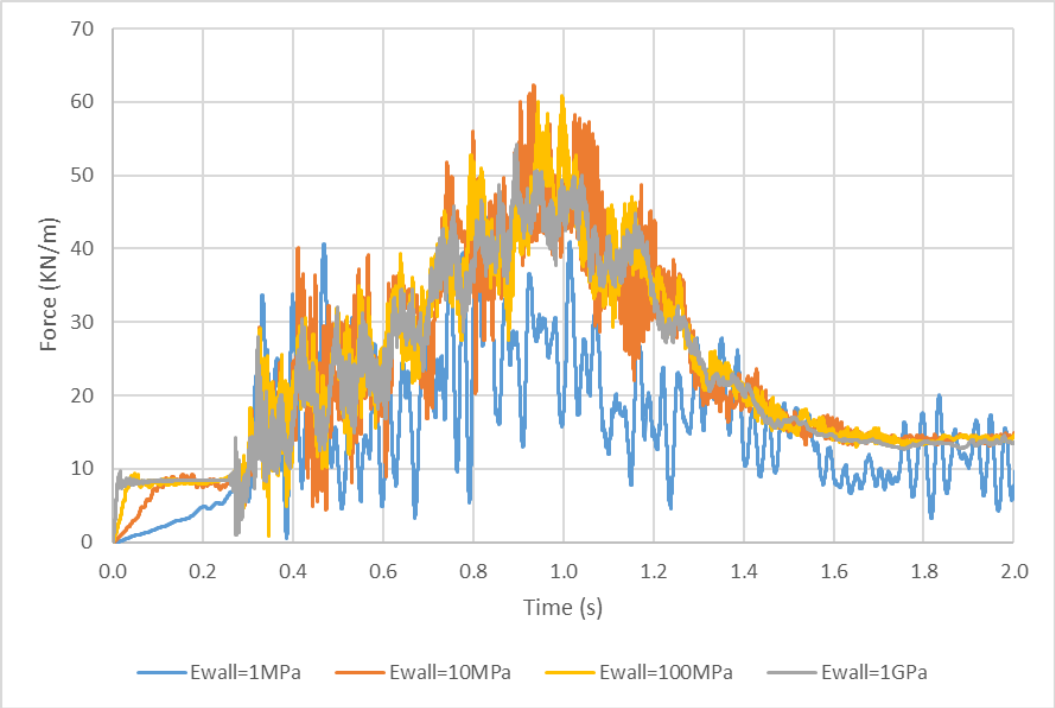

Figure 3.43 Impact force for different wall stiffnesses considering a front inclination of 8°

Figure 3.43 Impact force for different wall stiffnesses shows a sensitivity analysis of the wall stiffness keeping fixed the snow Young modulus at 1MPa.

Blue curve has a significant different trend compared to the others because the stiffness of the snow is the same as the one of the wall. Hence, it derives an amplification of the dynamic behaviour of the impact.

Mesh-dependency of the results is a common drawback of such dynamic problems; a moderate effect of larger forces for increasing sizes of the elements was observed (Initial and final part of Figure 3.44).

Force-time curves for different impact velocities shows that the higher the velocity, the earlier the impact occurs and the higher the maximum force is.

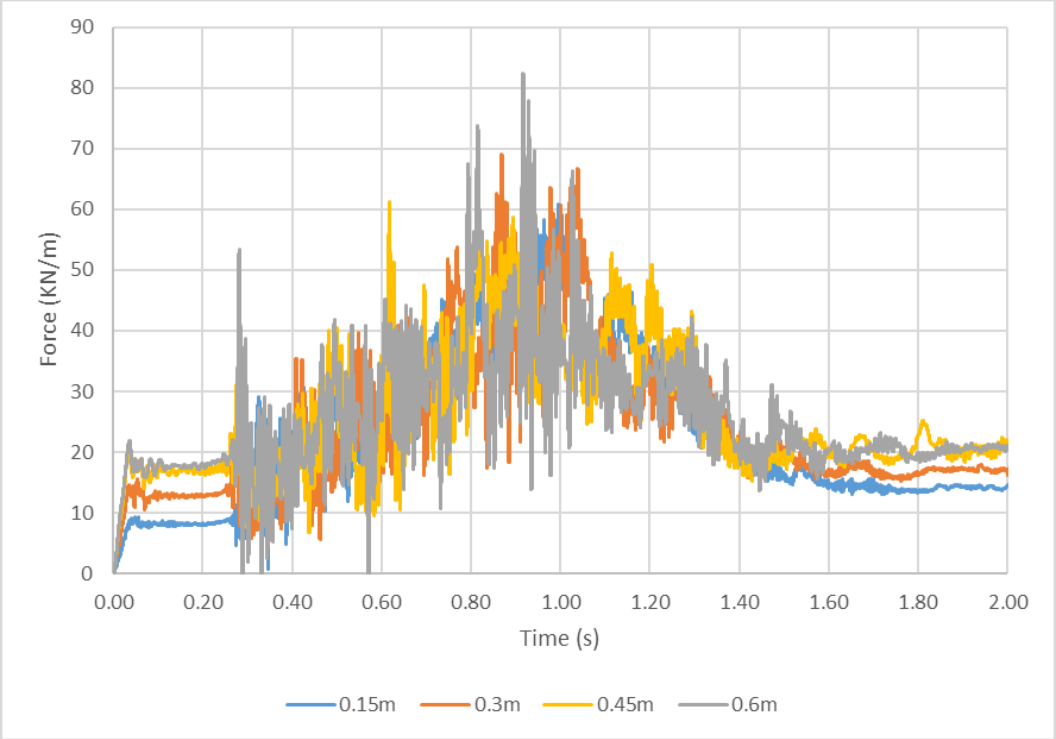

Figure 3.44 Effect of mesh size on the impact force evolution over time considering a front inclination of 8°

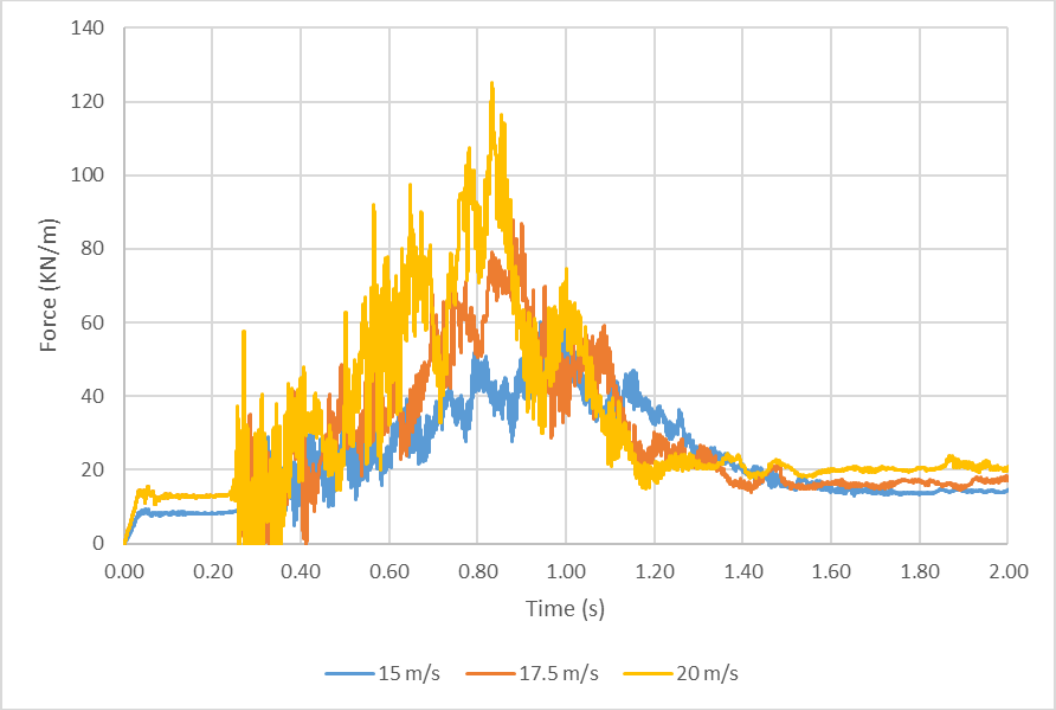

Figure 3.45 Impact force for different flow velocities considering a front inclination of 8°

From an approximate analysis, on the basis of the damage suffered by the building during the event of 2000 (Figure 3.32), the values of the impact forces match fairly well the expected damage.
The following table shows the damage potential for different avalanche pressures registered in past events [2].

Avalanche pressure (KPa)	Damage potential
1	Windows are pressed in and smashed
5	Doors are pushed in
30	Wooden constructions and brick buildings are destroyed
100	Spruce forest is thrown over a large area
1000	Reinforced concrete structures are damaged or destroyed

Table 3.9 Damage potential of avalanches in relation to the impact pressure

The structure was made of cemented stones with few lateral connecting elements that stiffened the walls and therefore the equivalent pressure producing such a damage might be in the range of 30-100 KPa. From the picture of the damaged building, it seems that the avalanche flowed over the roof which could not withstand the frictional forces and the pressure on the outer wall.
The meteorological information during the event suggested that no powder pressure was generated (Appendix) and all the damage is to be ascribed to the dense flowing core.

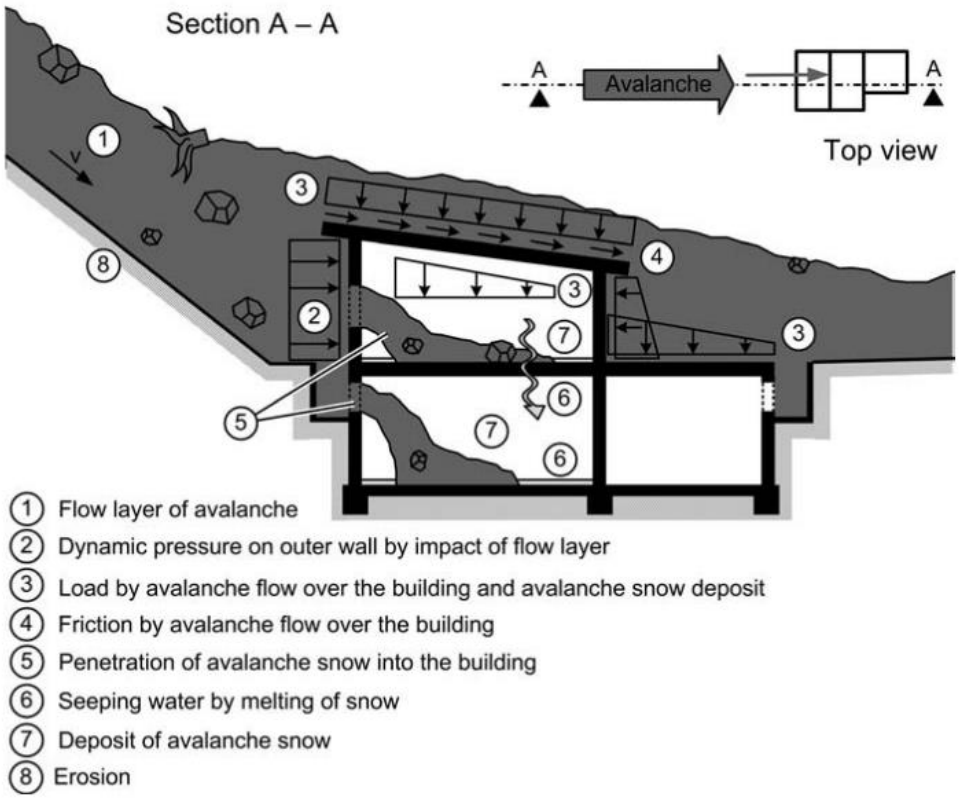

Figure 3.46 Action on a structure when an avalanche flows over the building [2] *(© Suda)*

A detailed analysis of the impact on the specific building was out of the scope of the thesis and therefore the investigation stopped at the level of computing the actions on the wall.
Nevertheless, knowing the in-depth effects on the actions caused by a flowing avalanche remains an interesting topic that must be investigated in the following studies.
Furthermore, the many rock boulders present in the valley might be dragged by the flow and impact the structures producing point-shaped action forces.

Although significant progress in the understanding of the interaction between snow avalanches and structures has been achieved in the last 15 years [55], an Italian regulation concerning avalanche hazard mapping still does not exist.

There are some guidelines proposed by the collaboration of University of Pavia with AINEVA (Italian association for Snow and Avalanches) [22], but they date back to 2004 and do not include important recent findings. The impact pressure of avalanches on big plate elements is expressed as the sum of a static and a dynamic contribution:

$$p_{dn} = p_{static} + p_{dynamic} = \rho \cdot g \cdot H + k\,(\rho \cdot v^2 \cdot \sin^2 \varphi) \qquad (3.5)$$

Where ρ is the average density of the snow, g the gravity acceleration, H the height of the flowing snowpack, v the velocity, φ the deflection angle and k a dimensionless coefficient assumed 1 for dense avalanches and 0.5 for powder ones [22].

Swiss guidelines suggest a value for the drag coefficient $k = 2$ and propose $\rho = 300Kg/m\text{^}3$ as a safe side assumption.
The impact creates also a vertical and tangential pressure that are often the main causes of damages to buildings.[2]

$$p_{dt} = \mu\, p_{dn} \qquad (3.6)$$

With $\mu = 0.3 - 0.4$ [25]
When flow velocity is higher than 10 m/s, the static contribution of (3.5) is negligible compared to the dynamic one and can be neglected.
The stress distribution proposed by both the regulations is made of two contributions: a uniform pressure p_{dn}in the snow depth upstream the obstacle and, above, is assumed to linearly decrease up to a stagnation height $h_{stau}$where the stresses nullify. The expression of h_{stau} is given by:

$$h_{stau} = v^2/2g\lambda \qquad (3.7)$$

The empirical dissipation coefficient λ accounts for the splashing of the flow and depends on the snow type: $\lambda = 1.5$ for dry, fluidised flows and $2 \leq \lambda \leq 3$ for dense flows.[25]

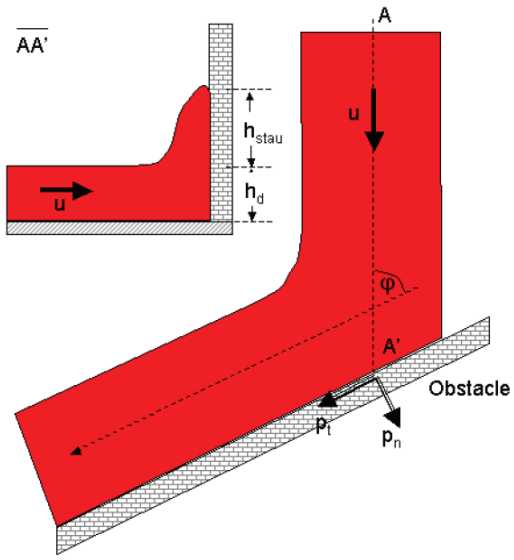

Figure 3.47 Schematic load on a large obstacle [11]

Equation (3.5) derives from hydraulics and consider snow as an incompressible fluid that hits a large obstacle. This oversimplification of the problem does not consider the time dependency of the phenomenon and has been proved underestimating from 2 (moist avalanches) to 6 times (dry) the values in the first moments of the impact.

Experiments by Bachmann [11] showed that, for $0.5 < Fr < 3$, the peak pressure was approximately 3 times higher than the pressure corresponding to an undisturbed flow. This value has been taken as a reference threshold in the Swiss guidelines for assessing the peak of the impact in dynamic applications [25]

Detailed investigations about short peaks and fluctuations of impact forces are difficult to carry out because of the interaction of the flow with the dynamic behaviour of the structure.

Another approach followed by some authors in these last years has been the study of the shock dynamics. [11]

When the flow suddenly hits the obstacle a pressure wave creates and travels upstream with a celerity C_{ps} which slows down the oncoming flow.

Applying the principle of linear impulse to the element of *Figure 3.48*:

$$-\rho C_p \Delta t A u_x = \int_{t0}^{ti} R dt \tag{3.8}$$

And being R the resultant force

$$R = [\, pA - (p + \Delta p)A \,] \tag{3.9}$$

These two equations lead to the following

$$\Delta p = \rho C_p u_x \tag{3.10}$$

The impact pressure is therefore linearly dependent to the velocity of the flow and to the celerity of the pressure wave C_p.

This last value depends on the bulk modulus of the fluid and on the density; a suggested magnitude for snow avalanches of that density is $C_p \sim 30/40 \frac{m}{s}$ [11].

The previous model over-confines the flow also in the vertical direction while in the real case the avalanche can spread out and reduce the excess of pressure. Furthermore, the pressure profile within the flowing layer has never been recorded in experiments and it might be that the wave propagation is not fully elastic. This transition from elastic to plastic should lead to a reduction of maximum peak pressure and an increase of the duration of the impact.[11]

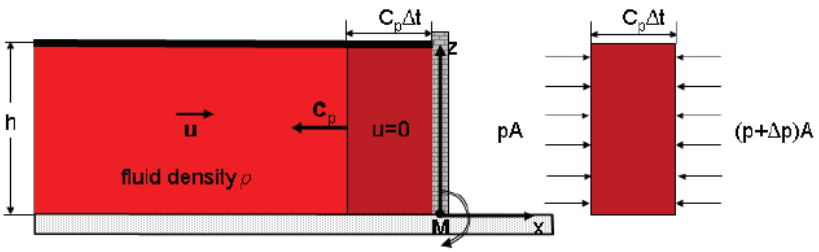

Figure 3.48 Shockwave sketch in the case of a lateral and vertical confined setting [11]

The linear impulse model has been compared with the results of MPM impact for a flow with a velocity $v = 15\ m/s$, density $\rho = 300 Kg/m^3$ and a perpendicular front.

Figure 3.49 MPM impact simulation of the flow with perpendicular front

Result of the simulation showed that the maximum force evaluated through MPM approach is within the range of values deducted with the empirical formulas. The most reliable among the two is the Swiss guideline because it has been directly extrapolated from experiments in site tests [56] and, as shown in Table 3.10, the two values are very similar.

Parameter	Swiss guidelines $p_{peak} = 3\,\rho u_x^2$	MPM	Linear impulse model $p_{peak} = \rho C_p u_x$
Peak pressure (KPa)	202.5	204	135

Table 3.10 Maximum impact forces with different models

Theoretically the linear impulse model has been developed under the assumption of confined flows and this should lead to an overestimation of pressures. In practice, the result from the elastic model is even lower than the others and the reason might be that the inaccuracy in the estimation of the wave celerity C_p hides the effect of confinement. The C_p values proposed in literature rely on numerical simulations and no direct measurements have ever been carried out. Looking at the numerical results with MPM, a celerity $40 < C_p < 45\frac{m}{s}$ can be deducted from the analysis of the shockwave generated after the impact.

Figure 3.51 and Figure 3.51 evidence the evolution in time both points velocities both normal stresses.

The shockwave in the first hundredths of a second involves the whole depth of the snow layer and it has a sharp discontinuity. As time goes on, the oncoming particles climb over the points attached to the wall and this process allows to dissipate the energy of the reflected wave. The magnitude of the stresses, in fact, more than halved in just 3 meters travel (Figure 3.51 at t=0.13s).

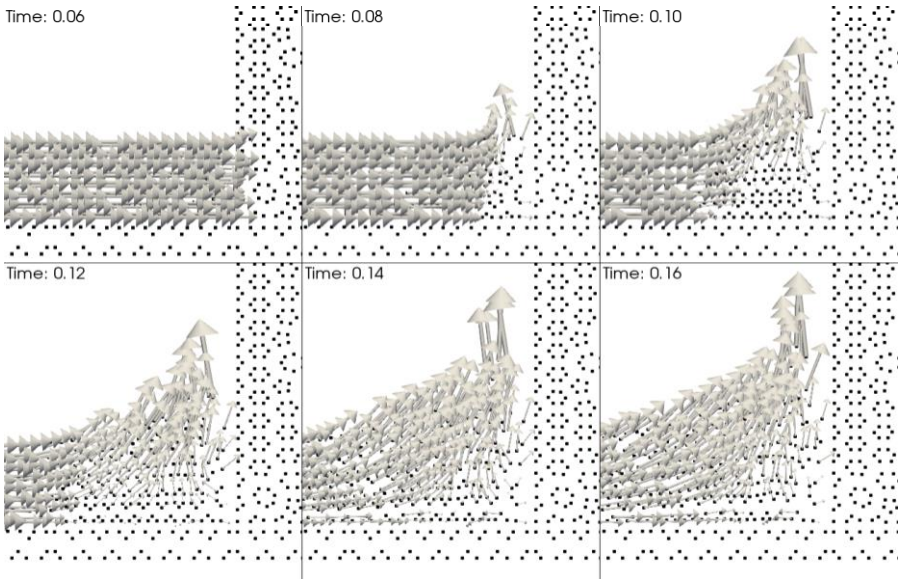

Figure 3.50 Magnitude and direction of the MP velocities during the impact

The previous figure well depicts the particle at rest and the initial phase of the splashing. This behaviour is less pronounced in the case of a front with 8° inclination because the particles first compact in the proximity of the wall and then start climbing.

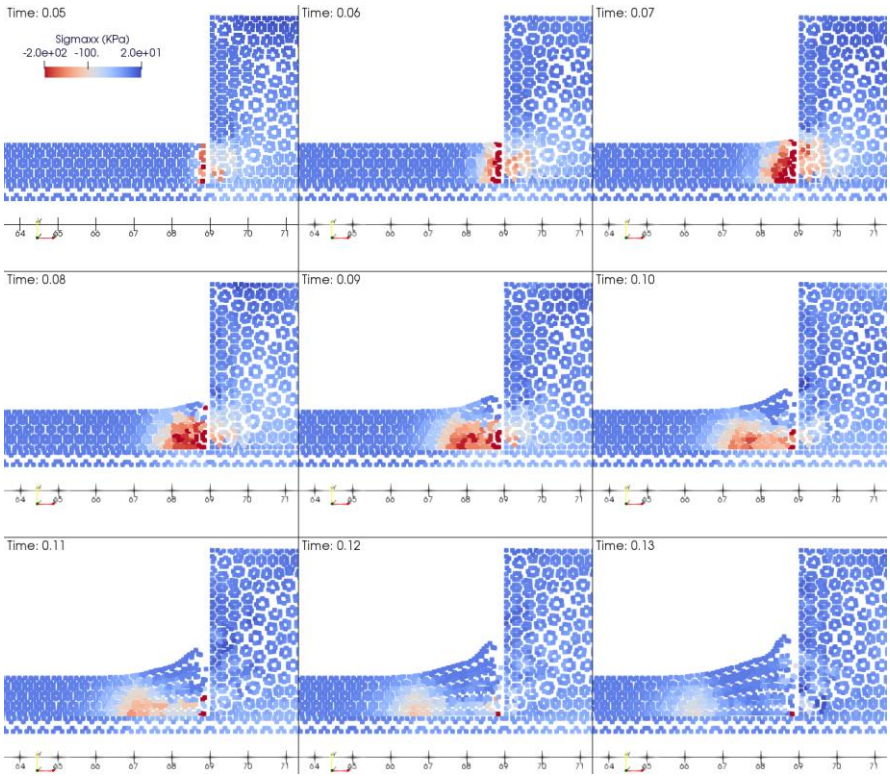

Figure 3.51 Screenshots at different instants of time showing the evolution of the shockwave

MPM simulation allows also to capture the dynamic behaviour of the impact.

In order to compare the pressure distribution obtained through the numerical approach with that used in common design practice, the front of the flow was set perpendicular.

The results in Figure 3.52 highlighted that the pressure can be considered, at the instant of peak impact, almost constant within the first 1-1.5 meters and then sharply drops to 0 in the rest of the structure.

Some parts of the structure undergo tensile stresses due to the relaxation of the material (t=0.10s at 1.5 m height).

The most conservative approach, to compare the MPM results with the other methods, has been considering the envelope of the maximum values of normal compressive stresses in time.

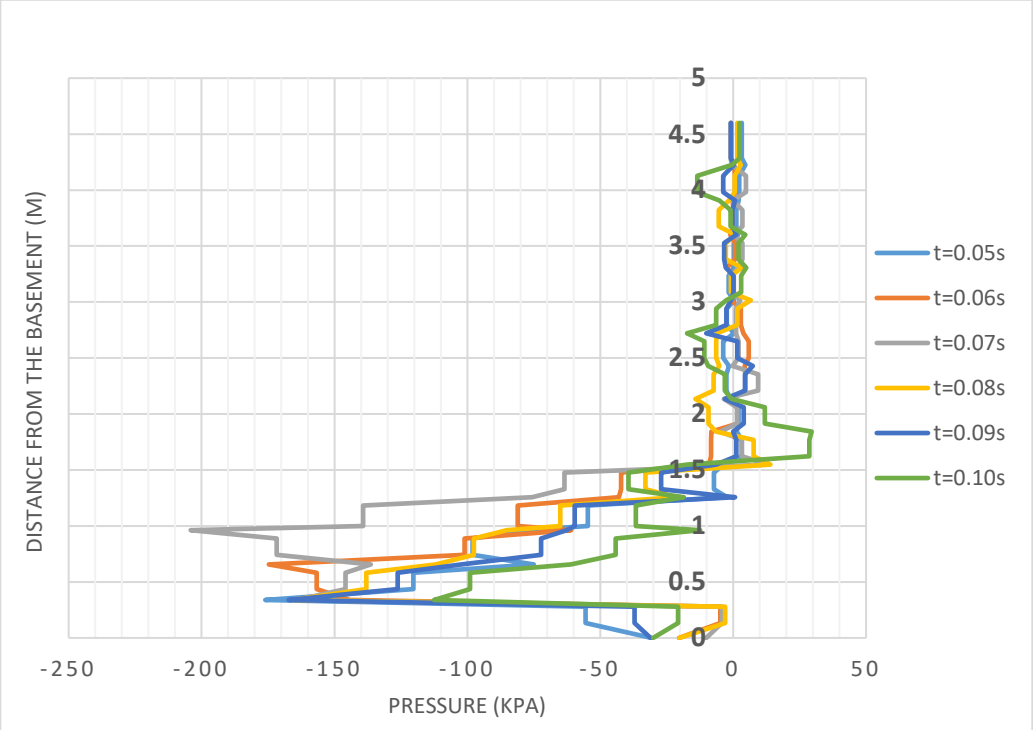

Figure 3.52 Pressure distribution along the height of the wall at different instants of time (perpendicular front)

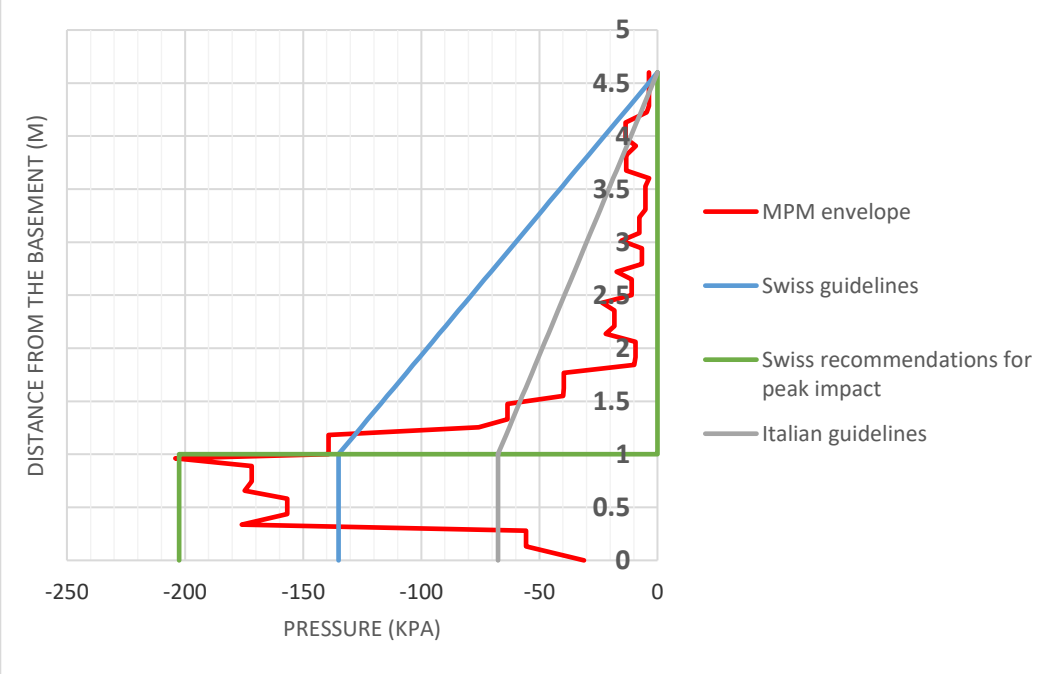

Figure 3.53 Comparison of the MPM results with the Swiss and Italian provisions

In Figure 3.53, the different distribution of stresses is shown; there is a perfect agreement of peak pressure among the numerical model and the Swiss guidelines. On the contrary the distribution of the pressures above the flow depth is lower than the national guidelines. A possible explanation might be that in MPM the influence of the saltation layer and the powder cloud is neglected while the guidelines are calibrated from experiments in which those processes could be present.

Looking at the actions on the wall caused by the impact (Table 3.11), the Swiss guidelines are the most conservative ones. Italian guidelines, on the contrary, underestimate the resultant force compared to MPM simulation. In actual fact, the envelope is not a real distribution of pressure and the values last just few hundredths of second, therefore the overall effect is not so relevant.

Parameter	Swiss recommendations $p_{peak} = 3\ \rho u_x^2$	Swiss guidelines $p = 2\ \rho u_x^2$	Italian guidelines $p = \rho u_x^2$	MPM
Peak pressure (KPa)	202.5	135	67.5	204
Resultant force (KN/m)	202.5	378.0	189.0	222.5
Resultant Moment (KN m/m)	101.3	599.2	299.6	270.1

Table 3.11 Actions on the structure with different impact models

CHAPTER 4
CONCLUSIONS

The analysis of propagation and impact of a dense snow avalanche was tackled. Following a numerical approach, the current possibilities and limitations of the Material point method have been investigated.
This study provides the available results from literature review on snow avalanches and explores the capabilities of MPM in modelling impacts.
It gives the research community a set of parameters that best fit the considered experiments and some findings about the sensitivity of the method to mesh size and number of discretization points.
These results confirmed the literature indications and proved a slight dependence of the number of Material Points with the shape of the deposit.
Mohr-Coulomb, Bingham and Newtonian constitutive models have been employed to model the behaviour of a dense snow avalanche.
The overall performance of the model was satisfactory for the propagation in small scale experiments both for solid and fluid constitutive laws.
However, for medium and large-scale problems, MPM Anura code still needs some improvements on the stability of the solution in modelling fluid constitutive models.
Real scale 3D problem is currently too demanding for Anura regarding the computational cost. For this reason, the real problem was tackled with 2 methods: Anura2D and 3D commercial model RAMMS.
Once both models have been calibrated on the position and height of the

deposit at the medium scale, they have been employed for the real scale analysis.
The results are similar in terms of runout and velocity profile along the slope. On the contrary, the 2D model has local discrepancies in flow height due to the lateral release restraint.
Subsequently, the velocity and height of the flow obtained from RAMMS at the hut location have been used as initial condition for studying the impact with a deformable obstacle which protects the buildings. The obtained results with MPM 2D seem to be compatible in terms of impact force with the damage experienced by the structure during past events.
The analysis captured the dynamic behaviour of the impact and showed that the national guidelines provide safe indications about final actions on the wall. Swiss recommendations are more stringent than the Italian ones, which should be validated for different conditions of snow and structures in additional studies.

Bibliography

[1] M. Stoffel, “Numerical Modelling of Snow using Finite Elements,” ETH Zurich, 2005.

[2] F. Rudolf-miklau and A. I. Mears, *The Technical Avalanche Protection Handbook*. 2011.

[3] S. Cresseri, “Constitutive modelling of dry granular snow at low strain rates,” Politecnico di Milano, 2005.

[4] J. P. Navarre, A. Taillefer, E. Flavigny, J. Desrues, and T. Gauthier, “Mécanique de la neige . Essais en laboratoire sur la resistance de la neige,” no. September 1986, pp. 129–138, 1987.

[5] J. D. Dent and T. E. Lang, “A biviscous modified Bingham model of snow avalanche motion.,” *Ann. Glaciol.*, vol. 4, pp. 42–46, 1983.

[6] E. Bovet, B. Chiaia, and L. Preziosi, “A new model for snow avalanche dynamics based on Bingham fluids,” *Prepr. Submitt. to J. Mech. Phys. Solid August*, vol. 7, pp. 1–22, 2008.

[7] E. Bovet, B. Chiaia, and L. Preziosi, “Non-Newtonian fluids for the avalanche dynamics behavior,” pp. 1–9.

[8] K. Oda, S. Moriguchi, I. Kamiishi, A. Yashima, K. Sawada, and A. Sato, “Simulation of a snow avalanche model test using computational fluid dynamics,” *Ann. Glaciol.*, vol. 52, no. 58, pp. 57–64, 2011.

[9] A. C. Hansen and R. L. Brown, “A new constitutive theory for snow based on a micromechanical approach,” *Avalanche Form. Mov. Eff. Proc. Davos Symp.*, no. 162, pp. 87–104, 1987.

[10] J. Gaume, T. Gast, J. Teran, A. van Herwijnen, and C. Jiang, “Dynamic anticrack propagation in snow,” *Nat. Commun.*, vol. 9, no. 1, 2018.

[11] T. Johannesson, P. Gauer, D. Issler, and K. Lied, “The design of avalanche protection dams. Recent practical & theoretical developments,” 2009.

[12] D. McClung and P. Schaerer, *The Avalanche handbook*, Third. Mountaineers Books, 2006.

[13] C. V. Valero, N. Wever, M. Christen, and P. Bartelt, “Modeling the influence of snow cover temperature and water content on wet-snow avalanche runout,” *Nat. Hazards Earth Syst. Sci.*, vol. 18, no. 3, pp. 869–887, 2018.

[14] J. Gaume, “Towards better forecast of slab avalanches,” *EPFL*, 2018. [Online]. Available: https://actu.epfl.ch/news/towards-better-forecasts-of-slab-avalanches/.

[15] “Avanza la slavina a Ludrigno,” 2014. [Online]. Available: https://www.valserianananews.it/2014/02/09/avanza-la-slavina-a-ludrigno-ad-ardesio-emergenza-anche-a-piazzolo/avanza-la-valanga-a-ludrigno-9-febbraio-2014-valseriana-news/.

[16] S. De Toni and P. Scotton, “Two-dimensional mathematical and numerical model for the dynamics of granular avalanches,” *Cold Reg. Sci. Technol.*, vol. 43, no. 1–2, pp. 36–48, 2005.

[17] M. Kern, P. Bartelt, B. Sovilla, and O. Buser, “Measured shear rates in large dry and wet snow avalanches,” *J. Glaciol.*, vol. 55, no. 190, pp. 327–338, 2009.

[18] M.-A. Baillifard, “Interaction Between Snow Avalanches and Catching Dams,” ETH Zürich, 2007.

[19] B. Sovilla, M. Kybruz, M. Schaer, and S. Margreth, “Avalanche pressure at the Vallé de la Sionne test site:comparison of maximum measured loads with design loads,” in *International Snow Science Workshop*, 2018.

[20] B. Sovilla and P. Bartelt, “Observations and modelling of snow avalanche entrainment,” *Nat. Hazards Earth Syst. Sci.*, vol. 2, no. 3–4, pp. 169–179, 2002.

[21] P. Gauer and K. Kristensen, “Four decades of observations from NGI’s full-scale avalanche test site Ryggfonn-Summary of experimental results,” *Cold Reg. Sci. Technol.*, vol. 125, pp. 162–176, 2016.

[22] M. Barbolini, L. Natale, M. Cordola, and G. Tecilla, “Linee guida metodologiche per la perimetrazione delle aree esposte al pericolo di valanghe,” 2002.

[23] A. Sinickas and B. Jamieson, “Comparing methods for estimating β points for use in statistical snow avalanche runout models,” *Cold Reg. Sci. Technol.*, vol. 104–105, pp. 23–32, 2014.

[24] C. Ancey, “Snow Avalanches,” 1999.

[25] E. Bovet, “Mechanics of Snow Avalanches,” Politecnico di Torino, 2012.

[26] H. Lagotala, “Étude de l’avalanche des Pèlerins (Chamonix) 10-11 avril 1924,” *Le Globe. Rev. genevoise géographie*, vol. 66, no. 1, pp. 37–85, 2015.

[27] U. Gruber and H. Haefner, “Avalanche hazard mapping with satellite data and a digital elevation model,” *Appl. Geogr.*, vol. 15, no. 2, pp. 99–113, 1995.

[28] U. Gruber and P. Bartelt, “Snow avalanche hazard modelling of large areas using shallow water numerical methods and GIS,” *Environ. Model. Softw.*, vol. 22, no. 10, pp. 1472–1481, 2007.

[29] M. Christen, J. Kowalski, and P. Bartelt, “RAMMS: Numerical simulation of dense snow avalanches in three-dimensional terrain,” *Cold Reg. Sci. Technol.*, vol. 63, no. 1–2, pp. 1–14, 2010.

[30] P. Bartelt, O. Buser, and K. Platzer, “Fluctuation-dissipation relations for granular snow avalanches,” *J. Glaciol.*, vol. 52, no. 179, pp. 631–643, 2006.

[31] S. Cresseri, “A framework for the constitutive modelling of dry granular snow at low strain rates.”

[32] K. Hutter, T. Koch, C. Plüss, and S. B. B. Savage, “The dynamics of avalanches of granular materials from initiation to runout. Part II. Experiments,” *Acta Mech.*, vol. 109, no. 1, pp. 127–165, 1995.

[33] K. Hutter, Y. Wang, and S. P. Pudasaini, “The Savage-Hutter avalanche model: How far can it be pushed?,” *Philos. Trans. R. Soc. A Math. Phys. Eng. Sci.*, vol. 363, no. 1832, pp. 1507–1528, 2005.

[34] E. Thibert *et al.*, “The full-scale avalanche test-site at Lautaret Pass (French Alps),” *Cold Reg. Sci. Technol.*, vol. 115, pp. 30–41, 2015.

[35] F. Ceccato, “Study of large deformation geomechanical problems with the Material Point Method,” 2015.

[36] H. Sulsky, D., Chen, Z., Schreyer, *A particle method for history dependent materials*. 1994.

[37] D. Sulsky, S.-J. Zhou, and H. L. Schreyer, “Application of a particle-in-cell method to solid mechanics,” *Comput. Phys. Commun.*, vol. 87, no. 1–2, pp. 236–252, May 1995.

[38] Anura3D, “Anura3D MPM software v.2018,” no. January, 2018.

[39] F. Ceccato, “Material Point Method : concetti base e applicazioni,” 2018.

[40] F. Calvetti, G. Crosta, and M. Tatarella, “Numerical simulation of dry granular flows: from the reproduction of small-scale experiments to the prediction of rock avalanches,” *Rivista Itaiana di Geotechnico*, vol. 34. pp. 21–38, 2000.

[41] Ceccato et Al., “Anura3D MPM software: tutorial manual,” 2019.

[42] F. Ceccato, “Run-up of granular avalanches on protective barriers : a numerical study with the Material Point Method,” *15th IACMAG*, no. October, 2017.

[43] F. Ceccato, I. Redaelli, C. di Prisco, and P. Simonini, “Impact forces of granular flows on rigid structures: Comparison between discontinuous (DEM) and continuous (MPM) numerical approaches,” *Comput. Geotech.*, vol. 103, no. December, pp. 201–217, 2018.

[44] F. Ceccato, “Study of flow landslide impact forces on protection structures with the Material Point Method,” *Landslides Eng. Slopes. Exp. Theory Pract.*, no. June, pp. 615–620, 2016.

[45] W. Steinkogler, B. Sovilla, and M. Lehning, “Influence of snow cover properties on avalanche dynamics,” *Cold Reg. Sci. Technol.*, vol. 97, pp. 121–131, 2014.

[46] A. Upadhyay, A. Kumar, and A. Chaudhary, “Velocity measurements of wet snow avalanche on the Dhundi snow chute,” *Ann. Glaciol.*, vol. 51, no. 54, pp. 139–145, 2010.

[47] R. K. Aggarwal and A. Kumar, “Application of CFD code for simulation of an inclined snow chute flow,” *Int. J. Eng. Res. Appl.*, vol. 3, no. 2, p. 10, 2013.

[48] R. Buhler, C. Argue, B. Jamieson, and A. Jones, “Sensitivity analysis of the RAMMS avalanche dynamics model in a Canadian transitional snow climate.” .

[49] P. Bartelt, B. Salm, and U. Gruber, “Calculating dense-snow avalanche runout using a Voellmy-fluid model with active/passive longitudinal straining,” *J. Glaciol.*, vol. 45, no. 150, pp. 242–254, 1999.

[50] M. Dei Cas, “Storia del rifugio Allievi Bonacossa,” 2003. [Online]. Available: www.paesidivaltellina.it/val_masino/valledizocca.htm#galleria%0D. [Accessed: 28-May-2019].

[51] Y. Bühler, M. Christen, P. Bartelt, W. Gerber, and B. Mcardell, “Rapid Mass Movements System RAMMS Where do we come from ? WSL / SLF in the ETH Domaine.”

[52] INER.Te.Co, “Gabbioni armati portanti.” [Online]. Available: http://www.inerteco.com/wp-content/uploads/2014/06/gabbioni-portanti-armati.pdf. [Accessed: 20-May-2019].

[53] F. Calvetti, C. di Prisco, I. Redaelli, A. Sganzerla, and E. Vairaktaris, “Mechanical interpretation of dry granular masses impacting on rigid obstacles,” *Acta Geotech.*, vol. 9, 2019.

[54] E. J. Fern and A. Rohe, *The Material Point Method for Geotechnical Engineering*, no. January. 2019.

[55] B. Chiaia, V. De Biagi, B. Frigo, L. Pitet, V. Segor, and P. Dynaval, *Manuale per lo studio dell ’ interazione del flusso valanghivo con un ostacolo*. .

[56] P. A. Schaerer and A. A. Salway, “Seismic and impact-pressure monitoring of flowing avalanches.,” *J. Glaciol.*, vol. 26, no. 94, pp. 179–187, 1980.

[57] E. J. Fern, A. Rohe, K. Soga, and E. Alonso, *The Material Point Method for Geotechnical Engineering : a Practical Guide*. 2019.

APPENDIX

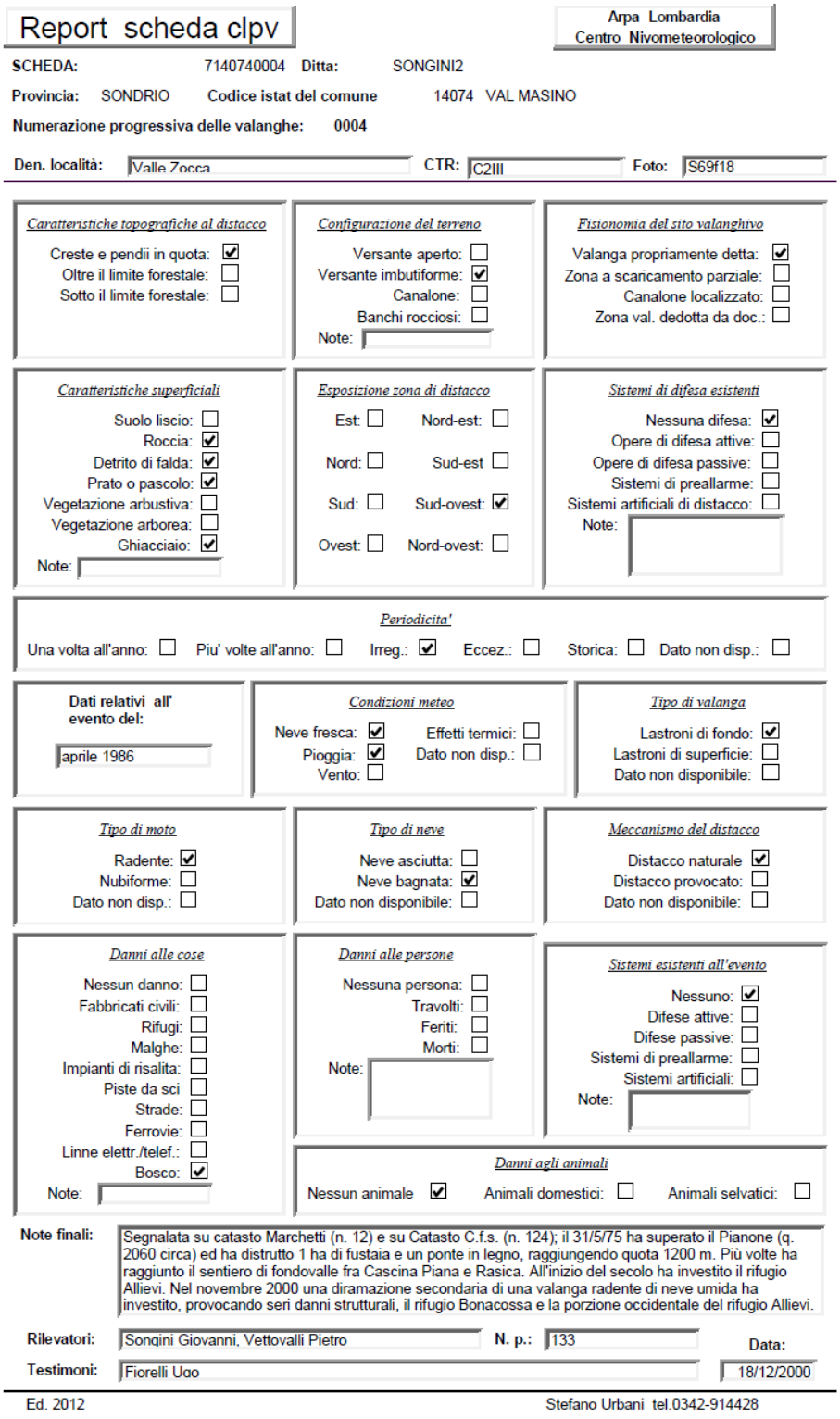

Report scheda clpv

Arpa Lombardia
Centro Nivometeorologico

SCHEDA: 7140740004 Ditta: SONGINI2

Provincia: SONDRIO Codice istat del comune 14074 VAL MASINO

Numerazione progressiva delle valanghe: 0004

Den. località: Valle Zocca CTR: C2III Foto: S69f18

Caratteristiche topografiche al distacco
- Creste e pendii in quota: ☑
- Oltre il limite forestale: ☐
- Sotto il limite forestale: ☐

Configurazione del terreno
- Versante aperto: ☐
- Versante imbutiforme: ☑
- Canalone: ☐
- Banchi rocciosi: ☐

Note:

Fisionomia del sito valanghivo
- Valanga propriamente detta: ☑
- Zona a scaricamento parziale: ☐
- Canalone localizzato: ☐
- Zona val. dedotta da doc.: ☐

Caratteristiche superficiali
- Suolo liscio: ☐
- Roccia: ☑
- Detrito di falda: ☑
- Prato o pascolo: ☑
- Vegetazione arbustiva: ☐
- Vegetazione arborea: ☐
- Ghiacciaio: ☑

Note:

Esposizione zona di distacco
- Est: ☐ Nord-est: ☐
- Nord: ☐ Sud-est ☐
- Sud: ☐ Sud-ovest: ☑
- Ovest: ☐ Nord-ovest: ☐

Sistemi di difesa esistenti
- Nessuna difesa: ☑
- Opere di difesa attive: ☐
- Opere di difesa passive: ☐
- Sistemi di preallarme: ☐
- Sistemi artificiali di distacco: ☐

Note:

Periodicita'

Una volta all'anno: ☐ Piu' volte all'anno: ☐ Irreg.: ☑ Eccez.: ☐ Storica: ☐ Dato non disp.: ☐

Dati relativi all' evento del: aprile 1986

Condizioni meteo
- Neve fresca: ☑ Effetti termici: ☐
- Pioggia: ☑ Dato non disp.: ☐
- Vento: ☐

Tipo di valanga
- Lastroni di fondo: ☑
- Lastroni di superficie: ☐
- Dato non disponibile: ☐

Tipo di moto
- Radente: ☑
- Nubiforme: ☐
- Dato non disp.: ☐

Tipo di neve
- Neve asciutta: ☐
- Neve bagnata: ☑
- Dato non disponibile: ☐

Meccanismo del distacco
- Distacco naturale ☑
- Distacco provocato: ☐
- Dato non disponibile: ☐

Danni alle cose
- Nessun danno: ☐
- Fabbricati civili: ☐
- Rifugi: ☐
- Malghe: ☐
- Impianti di risalita: ☐
- Piste da sci ☐
- Strade: ☐
- Ferrovie: ☐
- Linne elettr./telef.: ☐
- Bosco: ☑

Note:

Danni alle persone
- Nessuna persona: ☐
- Travolti: ☐
- Feriti: ☐
- Morti: ☐

Note:

Sistemi esistenti all'evento
- Nessuno: ☑
- Difese attive: ☐
- Difese passive: ☐
- Sistemi di preallarme: ☐
- Sistemi artificiali: ☐

Note:

Danni agli animali

Nessun animale ☑ Animali domestici: ☐ Animali selvatici: ☐

Note finali: Segnalata su catasto Marchetti (n. 12) e su Catasto C.f.s. (n. 124); il 31/5/75 ha superato il Pianone (q. 2060 circa) ed ha distrutto 1 ha di fustaia e un ponte in legno, raggiungendo quota 1200 m. Più volte ha raggiunto il sentiero di fondovalle fra Cascina Piana e Rasica. All'inizio del secolo ha investito il rifugio Allievi. Nel novembre 2000 una diramazione secondaria di una valanga radente di neve umida ha investito, provocando seri danni strutturali, il rifugio Bonacossa e la porzione occidentale del rifugio Allievi.

Rilevatori: Songini Giovanni, Vettovalli Pietro N. p.: 133 Data:

Testimoni: Fiorelli Ugo 18/12/2000

Ed. 2012 Stefano Urbani tel.0342-914428